Transient Response of a Large Two-Stroke Marine Diesel Engine Coupled to a Selective Catalytic Reduction Exhaust Aftertreatment System

A thesis submitted to

NATIONAL TECHNICAL UNIVERSITY OF ATHENS

for the Degree of
Doctor of Philosophy

Michael I. Foteinos

Thesis Supervisor:
Nikolaos P. Kyrtatos

November 2019

Dedicated to my parents

Non sunt multiplicanda entia sine necessitate

Occam's razor

THIS PAGE INTENTIONALLY LEFT BLANK

Acknowledgments

Michael I. Foteinos

Athens, November 2019

THIS PAGE INTENTIONALLY LEFT BLANK

Abstract

Large two-stroke marine diesel engines are used as the prime mover in the majority of ocean going commercial vessels. With a view of reducing the environmental footprint of the marine sector, the International Maritime Organization has enacted regulations which set strict limits on the emitted NO_x emissions from marine engines, also known as IMO Tier III. Selective Catalytic Reduction (SCR) is an exhaust aftertreatment technology which allows compliance with the new emission standards. Due to the need of high exhaust gas temperatures for proper SCR operation, in marine two-stroke applications the SCR system is placed upstream of the turbine, i.e. between the engine and the turbocharger. This disrupts the coupling between the engine and the turbocharger introducing challenges on the transient operation of the engine. Due to the large thermal inertia of the SCR system, the turbocharger responds to an engine load change with a significant time delay, which in low load engine operation might lead to thermal instability of the system. Researchers underlined the system's susceptibility to thermal instability and proposed complicated solutions to ensure the system's robust operation, such as Variable Turbine Geometry.

This thesis investigates the transient response of a large two-stroke marine diesel engine, without turbocharging variability, coupled to a SCR exhaust aftertreatment system. The objective of the thesis is to investigate the effect of the high pressure SCR system on the transient response of the engine with focus on low load operation. Due to the high cost involved in large engine testing the investigation was carried out via modelling and simulation. Zero dimensional models were developed for the propulsion engine and the SCR system. The engine was modelled in the NTUA in-house engine process simulation code and validated against available steady-state measurements from the engine's shop trials. Moreover, a SCR model was developed to take into account the temperature dynamics of the SCR system and was integrated with the engine model. The SCR model was validated against available measured data from a full scale engine-SCR testbed. In transient loading conditions, the load that the engine has to overcome,

i.e. the propeller load, is not known a priori, but is dependent on the complex interactions between the engine, propeller and the ship's hull. In order to obtain an accurate prediction of the engine load during load transients, models for the propeller and the ship's hull were also developed and integrated with the engine and SCR models. The coupled model of the propulsion system was validated under transient loading conditions using available on-board measured data from a commercial vessel.

Simulations of the propulsion system under transient loading were carried out under both calm and heavy weather conditions. Results showed that the transient response of the engine is indeed affected by the presence of the SCR system and the effect is more pronounced at the lower engine load region. However, thermal instability of the system can be averted and the system is able to operate even during very low load operation.

Contents

THIS PAGE INTENTIONALLY LEFT BLANK

List of Figures

THIS PAGE INTENTIONALLY LEFT BLANK

List of Tables

THIS PAGE INTENTIONALLY LEFT BLANK

Nomenclature

Acronyms

A/B   Auxiliary blower

ABS   Ammonium Bisulphate

CBV   Cylinder Bypass Valve

DOC   Diesel Oxidation Catalyst

DPF   Diesel Particulate Filter

DWT   Deadweight

ECA   Emission Controlled Area

EGR   Exhaust Gas Recirculation

IMO   International Maritime Organization

MCR   Maximum Continuous Rating

MVEM   Mean Value Engine Model

NO_x Nitrogen Oxides

RAO   Response Amplitude Operator

RBV   Reactor Bypass Valve

RSV   Reactor Sealing Valve

RTV   Reactor Throttle Valve

SCR   Selective Catalytic Reduction

SO$_x$ Suplhur Oxides

T/C Turbocharger

Symbols

A Area

A_1 Amplitude of surge motion

A_3 Amplitude of heave motion

A_5 Amplitude of pitch motion

A_{reg} Regular wave amplitude

B Ship breadth

b Factor for thrust and torque reduction due to propeller proximity to the free surface

c Specific heat capacity at constant pressure

C_P Prismatic Coefficient

C_Q Propeller torque coefficient (4-quadrant nomenclature)

C_T Propeller thrust coefficient (4-quadrant nomenclature)

D Diameter

E Energy

e PID Controller error

F_{fk} Froude Krylov forces

h Convective heat transfer coefficient

h_{heave} Propeller movement due to heave motions

h_{pitch} Propeller movement due to pitch motions

H_s Significant wave height

h_v Vertical distance between the propeller shaft centre and the free surface

I Polar moment of inertia

I_{ent} Water entrained polar moment of inertia

J Advance coefficient

k Wave number

K_Q Propeller torque coefficient (1-quadrant nomenclature)

K_T Propeller thrust coefficient (1-quadrant nomenclature)

L Ship length

m Mass

$\dot{m}$ Mass flow rate

M_{tip} Compressor impeller tip Mach number

N Rotational Speed

Nu Non-Dimensional Nusselt Number

p Pressure

P_{br} Engine Brake Power

Pr Non-Dimensional Prandtl Number

Q Torque

$\dot{Q}$ Heat flow

R Gas constant

r Radius

R_{θ} Thermal Resistance

R_{AW} Added resistance in irregular waves

R_{reg} Added resistance in regular waves

R_T Calm water resistance

Re Non-Dimensional Reynolds Number

S Spectral density

T Temperature

t Time

t_D Thrust deduction factor

t_{ins} Insulation thickness

T_{peak} Peak period

T_P Propeller Thrust

T_s Ship draught

U Blade tip velocity

V Volume

$\dot{V}$ Volumetric flow rate

V_a Mean effective wake velocity

V_r Relative advance velocity

V_s Ship speed

w Mean effective wake fraction

X Wave encounter angle

x_p Longitudinal coordinate of the propeller with reference to the centre of gravity of the ship

Y Controller Output

z_P Immersion depth of the propeller shaft

Greek Symbols

β Advance angle

γ Heat Capacity Ratio

$\Delta\theta_{IGD}$ Ignition delay

$\Delta\theta_{IND}$ Injection delay

ϵ Emissivity

θ_0 Crank angle at start of combustion

θ_{SOI} Crank angle at start of static injection

ζ Wave elevation

η_0 Propeller open water efficiency

η_{is} Compressor isentropic efficiency

κ Index for ship motions

λ Wave Length

ξ_1 Surge motion

ξ_3 Heave motion

ξ_5 Pitch motion

π Pressure ratio

ρ Density

σ Stefan-Boltzman constant

Φ Non-dimensional flow coefficient

ϕ Wave phase

ϕ_1 Phase lag of surge motion

ϕ_3 Phase lag of heave motion

ϕ_5 Phase lag of pitch motion

Ψ Non-dimensional isentropic head coefficient

ω Wave circular frequency

ω_{eng} Engine rotational speed

ω_e Wave encounter frequency

Subscript

act Blower activation

add Added

amb Ambient

C Compressor

$c \rightarrow w$ Catalyst to wall

cat Catalyst

$cell$ Catalyst cell

$comp$ Compression

$deact$ Blower deactivation

eng Engine

env Environment

exh Exhaust gas

exh Exhaust

fw Fresh water

$g \rightarrow c$ Gas to catalyst

$g \rightarrow w$ Gas to wall

max Maximum

p Propeller

$reac$ Reactor

$scav$ Scavenge

24

sw Sea water

T/C Turbocharger

$urea$ Urea

vap Vaporizer

$wall$ Wall

THIS PAGE INTENTIONALLY LEFT BLANK

Preface

In this chapter, the objective, contributions and structure of this thesis are presented. A list of the publications that emerged from the research work carried out in this thesis is also included.

Thesis Objective

This thesis focuses on the effect of the high pressure SCR exhaust aftertreatment system on the transient response of a large two-stroke marine diesel engine. High pressure SCR systems on marine diesel engines is a relatively new technology. The placement of the SCR system on the high-pressure side of the turbocharger turbine, i.e. between the engine and the turbocharger, introduces challenges on the transient operation of marine diesel engines. Due to the large thermal inertia of the SCR system, the turbocharger responds to an engine load change with a significant time delay. This delayed response could eventually result to a thermal instability of the engine-turbocharger system. This inherent susceptibility of the system to thermal instability was underlined by researchers (1). Codan et al (2), proposed that this should be treated with the implementation of variable turbine geometry (VTG), which is an expensive and complicated solution.

In the automotive industry SCR performance is investigated using a large number of available testbeds. On the other hand, in the case of large engines, few testbeds exist due to the low number of engine manufacturers and the high cost required for building such a testbed. Moreover, the high operating cost of a large engine testbed significantly limits the number of tests that can be carried out. Another alternative, would be to conduct engine tests on sailing vessels that have a SCR system installed. However, operating ships with SCR systems are still limited and this would further require agreement with vessel owners. Hence, having a fast and accurate simulation model that can be used for the investigation of engine performance during load transients would be both useful and cost-effective.

The objective of this thesis is to investigate the performance and response of a large two-stroke diesel engine coupled to a high pressure SCR system, during transient loading via simulation. The impact of the thermal inertia of the SCR reactor on the engine-turbocharger system is investigated under calm and heavy weather conditions, with focus on low load engine operation.

Thesis Contributions

A significant number of research works has been carried out on the transient performance of large two-stroke marine diesel engines. On the other hand, research on the transient response of such an engine coupled to a high pressure SCR exhaust aftertreatment system is limited. The contribution of this thesis lies on the modelling and simulation of a large two-stroke diesel engine coupled to a high pressure SCR exhaust aftertreatment system under transient loading conditions.

A zero-dimensional engine model was developed using the NTUA in-house engine simulation code MOTHER and validated against available data from the engine shop trials. To take into account the SCR temperature dynamics, a zero-dimensional model for the SCR system was also developed and integrated with the engine model. The SCR model was validated against available measured data obtained from a full scale engine-SCR testbed. In the context of simulating the entire marine propulsion powerplant, propeller and ship-hull models were also developed and integrated with the engine model. The coupled model of the propulsion plant was validated under transient loading conditions, using on-board measured data from a commercial vessel. It was then applied to investigate the transient performance of a Tier III engine under low load operation, as well as during heavy weather conditions.

Results showed that even though the transient operation of the engine is affected by the presence of the high pressure SCR system, thermal instabilities can be avoided. Simulations showed that the engine is able to operate even at very low load with the SCR system engaged, if the system is properly heated. The research performed within this thesis yielded the following scientific publications:

1. M.I. Foteinos, S. Konstantinidis, N.P. Kyrtatos, and K. Busk, "Simulation of the transient thermal response of a high pressure selective catalytic reduction aftertreatment system for a Tier III two-stroke marine diesel engine", ASME J. Eng. for Gas Turbines and Power, vol. 141, no. 7, 2019

2. M.I. Foteinos, G. Christofilis and N.P. Kyrtatos, "Response of a direct-drive large marine two-stroke engine coupled to SCR exhaust aftertreatment system when operating in waves", Proceedings of the iMeche, Part M: Journal of Engineering for the Maritime Environment, accepted for publication (12/2019)

3. M.I. Foteinos, A. Papazoglou, N.P. Kyrtatos, A. Stamatelos, O. Zogou, and A. M. Stamatellou, "A three-zone scavenging model for large two-stroke uniflow marine engines using results from CFD scavenging simulations", Energies, vol 12, no. 9, 2019.

4. M.I. Foteinos, G. Christofilis, and N.P. Kyrtatos, "Transient operation of a large two-stroke marine diesel engine equipped with a high-pressure SCR aftertreatment system in heavy weather conditions" 29th CIMAC Congress, Vancouver, Canada June 10th to June 14th, 2019.

5. M. I. Foteinos and N.P. Kyrtatos, "Transient Simulation of a Large Two-Stroke Marine Diesel Powerplant Operation with a High Pressure SCR Aftertreatment System", 27th Aachen Colloquium Automobile and Engine Technology, October 2018

Publications Currently Under Review:

1. M.I. Foteinos, G. Christofilis and N.P. Kyrtatos, "Large two-stroke marine diesel engine operation with a high-pressure SCR system in heavy weather conditions", Journal of Ship Research
Submission Date: 23/05/2019

2. M.I. Foteinos and N.P. Kyrtatos, "Transient response of a large two-stroke marine diesel engine coupled to a high pressure Selective Catalytic Reduction exhaust aftertreatment system", ASME J. Eng. for Gas Turbines and Power
Submission Date: 30/08/2019

Thesis Outline

The thesis is divided in the following Chapters:

Chapter 1, Introduction: This chapter includes a description of current emission regulations and NO_x abatement technologies with focus on the high pressure marine SCR exhaust aftertreatment system. It also outlines important and current research on marine diesel engine and SCR simulation.

Chapter 2, Marine Diesel Engine Model: In this chapter, the modelling of the marine diesel engine, extrapolation of the compressor performance maps and modelling of the auxiliary blower are presented.

Chapter 3, SCR System Model: This chapter includes a detailed presentation of the developed SCR model, followed by model validation using available experimental data from a full-scale engine-SCR testbed

Chapter 4, Propeller and Ship Hull Model: In this chapter the propeller and ship hull models used in this work are described.

Chapter 5 Coupled Model Validation: This chapter includes the validation of the coupled model of the marine propulsion powerplant. Validation is performed by comparing model predictions against available measured data obtained from an operating commercial vessel.

Chapter 6 Model Application and Results: In this chapter the coupled model is used to investigate the performance of the system under transient loading conditions.

Chapter 7 Conclusions and Future Work: This is the closing Chapter of the thesis, where the main results of the thesis are summarized and suggestions for future work are made.

Contribution of Diploma Theses

In the framework of this work, a number of diploma theses were carried out by undergraduate students of the School of Naval Architecture and Marine Engineering of NTUA, under the supervision of Prof. Nikolaos Kyrtatos and co-supervision of the author. The contribution of each thesis in the current work is outlined below.

- "Simulation of the transient operation of a large two-stroke marine diesel engine coupled to a high-pressure SCR exhaust aftertreatment system in heavy weather conditions". In this thesis, the propeller and ship hull models were extended for simulation in waves.

- "Development of SCR thermal model and performance of transient simulations with an engine simulation code". The author participated in the development and validation of the SCR model.

- "Update of the mixing coefficients of a scavenging model for large uniflow scavenged marine diesel engines". In this thesis the three-zone scavenging model employed in the current work was updated using results from CFD scavenging simulations.

Chapter 1

Introduction

Over the past few years, emissions of internal combustion engines have been on the spotlight due to their detrimental environmental effect. The International Convection of Prevention of Pollution from Ships (MARPOL) imposes strict limits on marine pollutants with focus on Nitrogen Oxides (NO_x) and Sulphur Oxides (SO_x). As far as NO_x emissions are concerned, the International Maritime Organization (IMO) has enacted stepwise restrictions (Tier I, II, III), so far culminating to the Tier III regulation (3). The Tier III standard applies to vessels with a keel laying date on or after January 1st 2016, when sailing inside NO_x Emission Controlled Areas (NECAs). For large two-stroke marine diesel engines with a rated speed below 130 RPM, Tier III imposes a limit of 3.4 g/kWh, which corresponds to a 75% reduction compared to the previous Tier II regulation. As of yet, NECAS include the North American coast, parts of Canada and the Caribbean Sea. As of January 1st 2021, the North Sea and Baltic Sea will also be designated as NECAS (4). IMO also sets restrictions on the emitted sulphur oxides (SO_x), which apply to all vessels regardless of keel laying date (3). Similar to NO_x, stricter limits are defined when sailing inside SO_x emission controlled ares (SECAs). Sulphur oxide emissions from marine diesel engines are solely dependent on the sulphuric content of the marine fuel used. SO_x abatement may be achieved either by switching to better quality fuel oil, or by the use of SO_x scrubbers which remove SO_x from exhaust gases.. On the other hand, NO_x emissions are mostly dependent on the peak in-cylinder temperature during the combustion process. The majority of produced NO_x in internal combustion engines is the so called thermal NO_x. The rate of NO_x formation increases significantly at high combustion temperatures (above 1800 K). At such high temperatures, the tripple bond of N_2 breaks allowing the formation of nitrogen oxides, NO and NO_2. These reactions can be described by the Zeldovich mechanism (5).

1.1   NOx Abatement Technologies in Marine Diesel Engines

The emission limits imposed by the Tier III standard, cannot be achieved by in-engine modifications such as combustion improvement (6; 7) or Miller timing (8). Water injection technologies seemed to be a promising solution, but they were associated with significant increase in SFOC and soot emissions as discussed in (9) and (10). Two established technologies for NO_x abatement, long used in heavy duty truck engines are the Exhaust Gas Recirculation (EGR) and the Selective Catalytic Reduction (SCR). EGR is a technology which aims to reduce the amount of produced NO_x during the combustion process by lowering the peak combustion temperature. This is achieved by recirculating a portion of exhaust gas back to the scavenge receiver. In this way, the O_2 content in the cylinder is decreased and the heat capacity of the mixture entering the engine increases. As a result, peak combustion temperatures drop, leading to reduced thermal NO_x formation. On the other hand, SCR is an aftertreatment technology which removes the NO_x that were formed during combustion in a reactor, which is placed either upstream or downstream the turbocharger turbine. In the SCR reactor, the NO_x are reduced catalytically to nitrogen and water by adding ammonia as a reducing agent. The catalyst is placed inside the reactor and consists of blocks with a large number of channels, providing a large surface area.

1.2   High-Pressure SCR System: Working principle and operational challenges

An essential parameter for robust SCR operation is the exhaust gas temperature at the SCR inlet. A lower temperature limit is imposed due to the presence of sulphur in most marine fuels and the subsequent presence of sulphuric acid in exhaust gases. At low exhaust gas temperatures, the sulphuric acid reacts with ammonia producing ammonium bisulphate (ABS), a sticky substance which accumulates in the SCR elements and eventually clogs the reactor. The bulk condensation temperatures of ABS at high and low exhaust pressures is shown in Figure 1-1. The ABS formation reaction can be suppressed if exhaust gas temperature at the reactor inlet remains above 320 ^oC (11; 1). A higher exhaust gas temperature limit of 500 ^oC is imposed by the oxidation of ammonia and catalyst material strength.

In four stroke engine applications, the exhaust gas temperature downstream the turbine is adequately high for SCR operation. On the other hand, in two stroke engine applications, due to the high thermal efficiency of these engines and the mixing of exhaust gas with air during
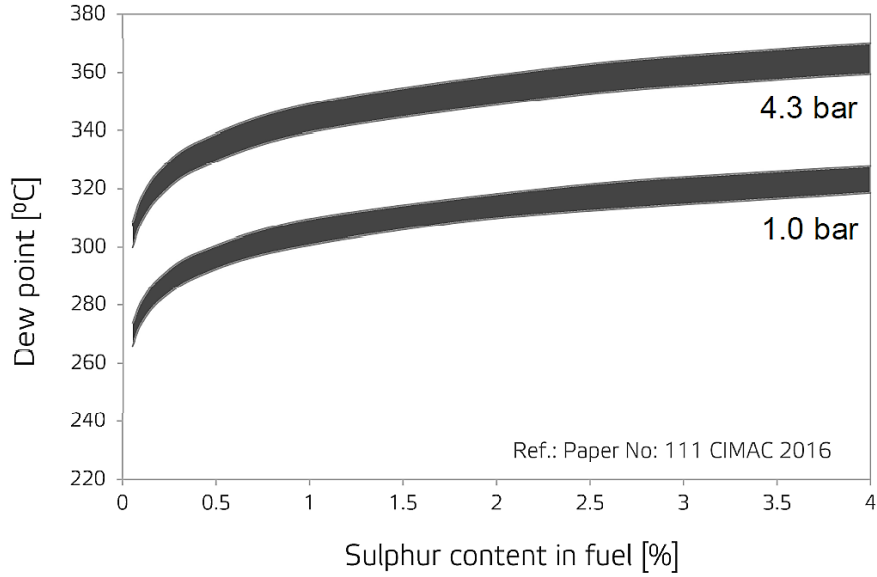
Figure 1-1: Bulk condensation temperatures of ABS at high and low exhaust pressure (12)

scavenging, exhaust gas temperature after the turbine lies between 230 and 260 ^{o}C. For this reason, in two stroke engine applications, the SCR reactor is placed upstream the turbine (high pressure SCR concept), in order to obtain exhaust gas temperatures sufficient for SCR operation. An overview of the examined High Pressure SCR system, as proposed by the engine manufacturer MAN Energy Solutions (11) is presented in Figure 1-2, where the various flow regulating valves are shown. When NO_x abatement is required, the exhaust gas is led through the SCR system via the Reactor Sealing Valve (RSV) and the Reactor Throttle Valve (RTV), while the Reactor Bypass Valve (RBV) is closed. An aqueous solution of urea (40% urea) is injected in the vaporizer, where due to the high temperatures in the exhaust gas, urea decomposes to ammonia by heat in the presence of water as shown below:

$$(NH_2)_2 \longrightarrow NH_3 + HCNO \tag{1.1}$$

$$HCNO + H_2O \longrightarrow NH_3 + CO_2 \tag{1.2}$$
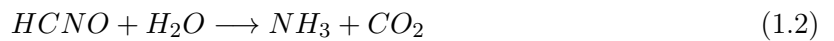
The injected urea undergoes two chemical processes in order to produce the ammonia needed for the SCR reactions. The first process, described in Eq. (1.1), is the decomposition of urea to ammonia and isocyanic acid. The second process, described in Eq. 1.2, is the hydrolysis of the isocyanic acid to ammonia and carbon dioxide. The first reaction is endothermic (ΔH=185.5 kJ/mole), while the second is exothermic (ΔH=-95.9 kJ/mole). Hence, the total process of urea decomposition can be considered as endothermic (ΔH=89.6 kJ/mole) (13). Then, the exhaust

gas is guided through the reactor where NO_x contained in exhaust gas is reduced catalytically by NH_3 to N_2 and H_2O. The three main SCR reactions are shown below, all of which are exothermic.

$$4NO + 4NH_3 + O_2 \longrightarrow 4N_2 + 6H_2O \qquad (1.3)$$

$$6NO_2 + 8NH_3 \longrightarrow 7N_2 + 12H_2O \qquad (1.4)$$

$$NO + NO_2 + 2NH_3 \longrightarrow 2N_2 + 3H_2O \qquad (1.5)$$
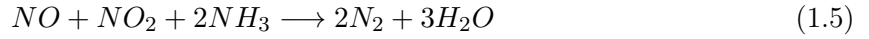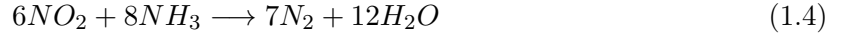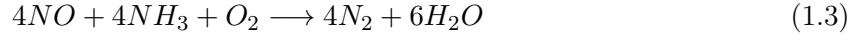
When SCR operation is not required, the SCR system is isolated by valves RSV and RTV and exhaust gas is led directly to the turbine through valve RBV. Even though the reactor is placed upstream the turbocharger turbine, at low engine loads the exhaust gas temperature would still not be sufficient for SCR operation. The Cylinder Bypass Valve (CBV) is engaged during low load operation to increase exhaust gas temperature and avoid formation of ABS on the SCR catalyst. When CBV is open, a fraction of compressed air from the scavenge receiver is led directly to the turbine, bypassing engine cylinders. In this way, the amount of combustion air decreases and combustion becomes richer, without reducing scavenge pressure, which leads to increased exhaust gas temperature.
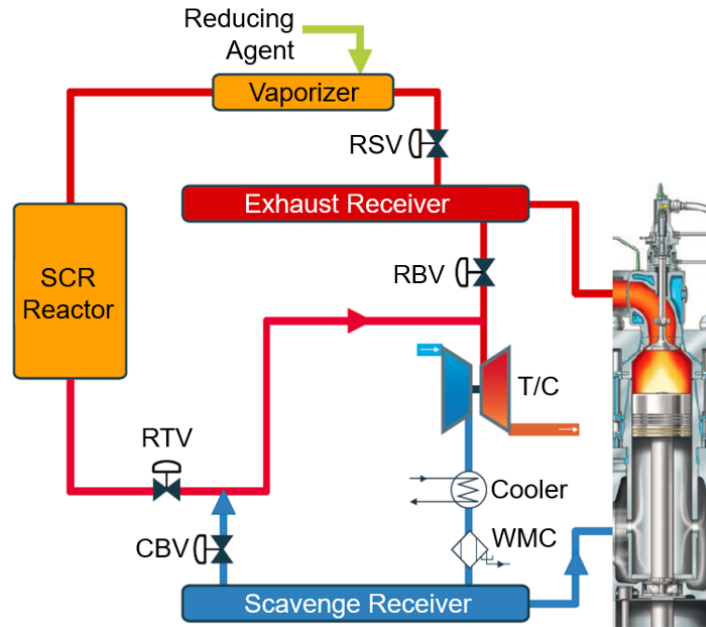
Figure 1-2: Overview of the examined high pressure SCR system (11)

The placement of the reactor upstream the turbine, helps maintain high exhaust gas temperature at the SCR inlet, but the large thermal inertia of the SCR system disrupts the coupling between the engine and the turbocharger. The thermal inertia of the reactor, causes a delayed

response of the turbocharger to an engine load change since exhaust gases are either heated or cooled by the reactor. As a result, the transient response of the engine, especially at low load operation, may be heavily affected.

Moreover, an instability of the system, known as thermodynamic oscillations might emerge during low load operation (11; 1; 2). An example of thermodynamic oscillations during low load operation of a large two-stroke marine diesel engine is shown in Figure 1-3. Measured timeseries of engine load, turbocharger speed and exhaust gas temperature at the inlet and outlet of the SCR system are presented. A sudden load spike around 600 s is the triggering factor of oscillations. While the exhaust gas temperature at the SCR inlet increases rapidly the increase in SCR outlet temperature is much slower due to the heat transferred from the exhaust gas to the reactor, i.e. the exhaust gases are cooled from the reactor. The heating of the reactor requires a significant amount of time due to its large thermal inertia. When the reactor is heated (hence exhaust gas is no longer cooled by the reactor), high temperature exhaust gases reach the turbine, increasing turbine power and consequently the airflow in the engine. As it can be seen in Figure 1-3, while the turbine accelerates the engine load (hence the fuel flow) drops. As a result, the fuel to air ratio is decreased and the energy content of the exhaust gases drops. These lower enthalpy exhaust gases do not reach the turbine instantly, but with a time delay,
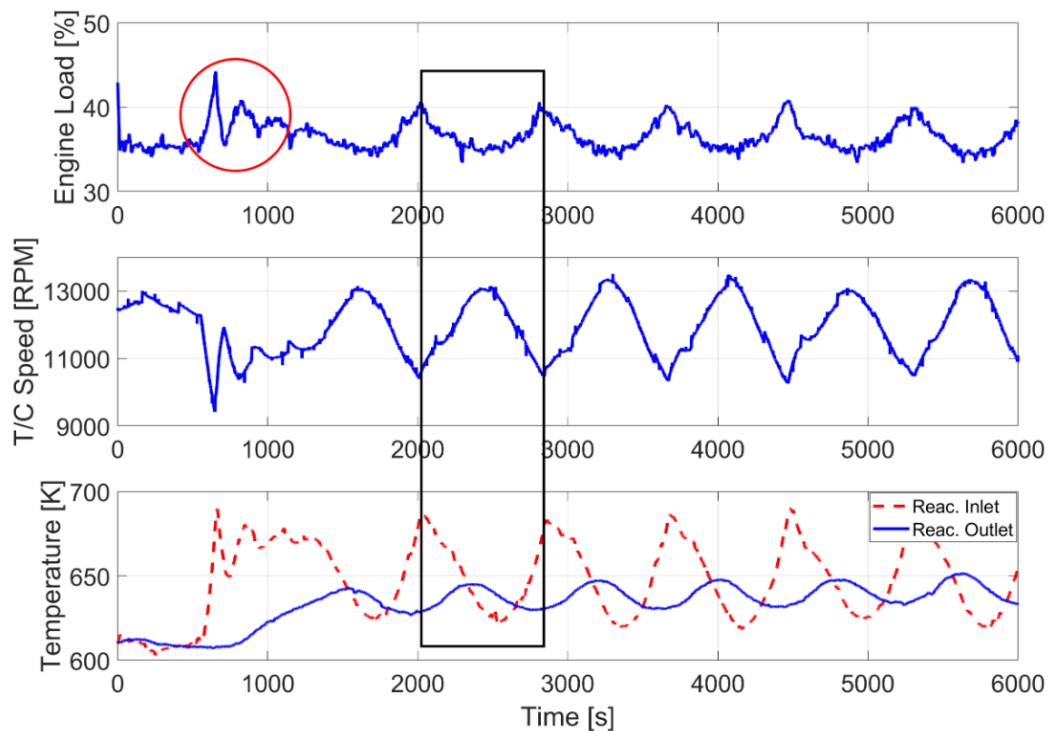
Figure 1-3: Thermal Oscillations on a large two-stroke engine with a High Pressure SCR (Testbed measurements) (14)

as in this case heat is transferred from the warmer reactor to the exhaust gases, i.e. exhaust gases are heated by the reactor. When the lower enthalpy exhaust gases reach the turbine, turbine power decreases, engine load (hence fuel flow) increases, leading to higher exhaust gas temperature. The periodic heating and cooling of exhaust gases by the reactor, is the reason behind SCR thermal oscillations. The phase difference between the exhaust gas temperature at the inlet and the outlet of the SCR system, is rendered in a phase difference between engine load and turbocharger speed. Engine load crests correspond to turbocharger speed troughs and vice versa.

1.3   Related Research

1.3.1   Internal Combustion Engine Modelling

Internal combustion engine modelling has been an important research topic and a large amount of research has been carried out concerning the development of zero dimensional (0-D), mean value engine models (MVEMs) and CFD engine models. Dynamic engine performance is primarily investigated using zero dimensional or mean value engine models due to the lower computational resources they require compared to CFD models. In this work, the transient engine performance is investigated using a zero-dimensional engine process simulation model, but research works which employed MVEMs are also presented in this section for reasons of completeness.

Zero dimensional models are more accurate and computationally demanding than MVEMs. A very detailed zero dimensional model capable of capturing engine dynamics is presented by Kyrtatos et al in (15). The model was used to investigate the behavior of a large two-stroke marine diesel engine during various load changes as well as during crash stop manoeuvre. The model was further used in the work of Livanos et al (16) where it was used to simulate the operation of a large two-stroke diesel engine during a fire in the scavenge receiver. The main finding of this work was that if the sludge burning rate is too high, compressor surge may occur. Moreover, simulations showed that fire in the scavenge receiver may lead to loss of engine controllability since the fuel cut-off may not be enough to stop the engine. The same detailed model was used in (17) for control and optimization purposes. The model was validated using performance measurements conducted on-board a 4600 TEU containership. Based on simulation results, a simpler transfer-function type model was developed and then utilized to design an improved engine speed controller. The developed speed controller was then integrated in the

model and predictions showed improved transient performance of the powerplant. In (18) the NO_x reduction potential of EGR technology on a large two-stroke diesel engine is investigated using a multi-zone combustion model. The authors concluded that the fuel penalty due to EGR is lower in the case of two-stroke slow speed engines compared to high speed DI engines, due to the higher amount of time available for combustion and the lower fuel to air ratios in these engines. Zero dimensional models have also been used for the prediction of marine diesel engine performance under fault conditions as in (19).

On the other hand, mean value engine models are simpler, require less amount of input data while predicting engine behaviour with sufficient accuracy. In (20), a complete two-stroke engine model which is able to capture the transient behavior of the engine is presented. The significance of the turbocharger dynamics for the transient response of the engine was investigated in (21) and (22). In (23) the performance of a large containership propulsion engine at slow-steaming conditions was investigated using a MVEM.

In recent works, MVEMs are combined with zero-dimensional models in order to combine the advantages of both modelling techniques. In (24) the closed cycle of engine cylinders are modelled using a 0-D approach, while the open cycle is modelled using a mean value approach. In (25) a MVEM is extended with a 0-D combustion model, to investigate the effect of turbocharger cut-out and auxiliary blowers deactivation during transient engine operation. The same model is used in (26) to map different engine parameters and use the results to develop functional extensions to a two-stroke diesel MVEM. Finally, in (27), a 0-D cylinder model is integrated with a MVEM based on asynchronous calculations to achieve real-time engine simulations.

1.3.2   SCR Modelling

A very good overview of SCR technology for mobile diesel applications can be found in (28). A large number of publications deal with SCR modeling in medium and heavy duty four stroke applications. In these engines the reactor size is small compared to marine applications, and hence the impact of the reactor's thermal inertia on the transient thermal response of the SCR is not of high importance. As a result, most publications focus on chemical modeling and the prediction of NO, NO_2 and NH_3 concentrations at SCR outlet rather than the SCR transient thermal response. Such models can be found in (29; 30; 31). A control-oriented model investigating the temperature dynamics of SCR, DOC (Diesel Oxidation Catalyst) and DPF (Diesel Particulate Filter) in a medium duty engine is presented in (32). The thermal inertia of a DOC

for a medium-duty engine during is investigated in (33).

Publications on SCR models for large two-stoke diesel engines are much fewer. The basic principles, challenges and control issues of the marine high pressure SCR sytem are outlined in (1). In this work, experimental results from the operation of a large two-stroke marine diesel engine equipped with a SCR system are presented in both steady state and transient loading conditions. Moreover, the thermal instabillity of the system is demonstrated using results from numerical simulations without however, presenting the models employed in the simulation. The effect of the reactor thermal inertia and the thermodynamic instability of high pressure marine SCR systems are further discussed in (2). In this work, the emergence of thermal oscillations even during constant load operation, and the effect of reactor size were investigated through simulation. The authors used a thermal model, considering ceramic and metal thermal mass, which is however not presented. In this work it is suggested that the engine can be safely operated only with additional variability in the turbocharger system. A simple SCR heating model can be found in (34). In this work, the exhaust gas temperature at the SCR outlet was modelled as a relationship between the position of valve RTV, the massflow of exhaust gas through the reactor and the exhaust gas temperature at the SCR inlet. The control of SCR systems has also attracted the interest of quite a few researchers. An overview of the state of the art in SCR control can be found in (35). As far as control in marine SCR systems is concerned, model based urea control strategies for a marine SCR system are investigated in (36). In this study, an optimal control strategy is developed in order to compromise the NO_x conversion rate with NH_3 slip. The urea dosing rate is calculated based on a chemical kinetics SCR model, enabling the controller to respond to transient conditions in advance. Finally, the NO_x conversion performance of a vanadium based SCR catalyst at marine engine like conditions (exhaust pressures up to 5 bar) was investigated experimentally in (37). Results showed that the NO_x conversion rate was independent of pressure, indicating that the SCR kinetics are not affected by the increased pressure up to 5 bar.

1.3.3   Marine Propulsion System Modelling

In this work, the performance of the entire propulsion system is investigated through simulation. Most of the research that was carried out in this field focused on Tier II engines i.e. engines without an EGR or an SCR unit. In (15) the potential problems of very large engines during transient operation are discussed. Models for the propeller hydrodynamics, hull resistance and

ship steering were integrated into one model, to simulate the dynamics of the entire marine powerplant. The combined model was used to investigate the transient behavior of highly rated marine diesel engines during load changes and crash stop manoeuvre. In (38) a mathematical model was developed in the Matlab-Simulink environment, with the aim to investigate the dynamic performance of a marine powerplant. Ship resistance was obtained using model test data and propeller characteristics were calculated using published open water characteristics of controllable pitch propellers. The model was validated against measurements obtained from a cruise ferry during steady state and transient operation. The model was extended to consider the ship manoeuvrability in the horizontal plane in (39) and validated using sea trials data. Livanos et al (40) investigated the performance of a medium speed marine propulsion engine during non-normative operating conditions, such as crash stop, full astern and full ahead manoeuvres. The engine model consisted of a set of thermodynamic performance maps, implemented in the Matlab/Simulink environment. Mean value engine models are also used in publications that examine the behaviour of the entire propulsion system. In (41) a mean value engine model was used in conjunction with a controllable pitch propeller model and a ship hull model to investigate the performance of a tanker during ice operation. Simulations were used in order to adjust the control modes of the engine for ice operation. In the work of Llamas et al (42), a control-oriented mean value engine model of a large two-stroke engine with an Exhaust Gas Recirculation (EGR) system is presented. A detailed model for the cylinder pressure is presented and validated with cylinder pressure measurements. Also, a parameterization procedure that deals with the low number of measurement data available is proposed. The model was validated using ship-board measured data under steady state and transient loading conditions including EGR start and stop scenarios.

Operation in waves has also been a subject of high interest for many researchers. Most works, focus on the effect of waves on the propeller performance. The open water characteristics of a propeller in regular waves are reported in (43). In the work of Nakamura et al (44), the open water characteristics of a propeller in regular and irregular waves are studied and it is showed that the average propeller characteristics in waves are identical with the ones in calm water conditions. Sluijs in (45) performed experiments with a ship model of 0.825 block coefficient in regular and irregular waves. Results showed that mean thrust and torque increase of the propeller, vary with the squared wave amplitude. Wake flow measurements in waves can be found in the works of Aalbers et al. (46) and Nakamura et al. (47) where wake measurements

were carried out at the propeller position without a propeller. In both these works it was shown that the average wake coefficient in regular waves varies as a function of wavelength. Politis used an unsteady BEM time stepping algorithm to predict the unsteady performance of a propeller in heaving and pitching motions (48; 49). It was shown that the combined heaving and pitching motion of a propeller, increases the mean developed force and absorbed power. Thus, the propeller seems more loaded when operating in a wavy environment. The effect of waves on the propeller inflow velocity is discussed by Tasaki (50) and Ueno (51). Ueno et al proposed a relation for the prediction of propeller inflow velocity in the presence of regular waves in (51). The authors used ordinary thrust and torque identification methods which are originally for calm water conditions, to analyse the unsteady inflow velocity in waves. The effect of wake variations due to waves on propeller cavitation was investigated in (52). It was found that the presence of waves does not significantly affect cavitation, despite large changes in the wake field.

On the other hand, publications that investigate the effect of waves on engine operation are much fewer. The effect of different regular waves on the performance of a conventional Tier II engine under steady engine load, was investigated by Yum et all in (53). The engine was modelled using zero dimensional models and the propeller open water characteristics were obtained using the open-source software Openprop. In the work of Taskar et al (54), a method for modelling wake in waves was presented, which allows the studying of the propulsion system in waves of different wavelength, height and direction. In the work of Kyrtatos et al (55), a method for predicting propeller torque demand of large ships in heavy weather using systematic tank test results is presented and validated. The method is based on the measurement of the instantaneous vertical acceleration of the stern of the ship as well as the instantaneous shaft torque. Torque prediction can be used to reduce the effect of extreme load changes, such as those present in heavy weather conditions. Moreover, the response of low-pressure dual fuel engines under wave load conditions is presented in (56). The performance of these engines in waves is of high interest, since they operate on the Otto cycle and as a result they are prone to knocking and misfiring. These inherent Otto cycle problems could accentuate in the case of unsteady working conditions, as in the case of waves. In this work, the engine operated at constant engine speed while coupled to a water brake. The rough weather conditions were simulated by a torque fluctuation of the water brake by 9% at a period of 20 seconds. It is reported, that the engine managed to operate without any misfire or knocking. Finally, the simulation of a hybrid marine propulsion system in waves can be found in (57). Simulation

results showed that having an energy storage device enables to utilize the shaft generator as an active aid to propulsion with allowable influence on the generator load.

1.4   Experimental data used

Different sets of experimental data were utilized to tune and validate the models. The engine model was developed using steady state measurements obtained from the engine's shop trials. Shop trials are carried out at the engine maker's site, which is usually a shipyard and the engine is loaded using a water brake. The SCR system was validated using measurements from a full scale engine and SCR test-bed. The coupled model of the marine powerplant was validated using two different sets of measurements under dynamic conditions. The first set was obtained during the ship's sea trials and the second was obtained during vessel operation shortly after she was commissioned.

THIS PAGE INTENTIONALLY LEFT BLANK

Chapter 2

Marine Diesel Engine Model

In this chapter the development and validation of the propulsion engine model are described. Moreover, the procedure followed for the extrapolation of the compressor compressor maps as well as the modelling of the auxiliary blowers are presented. The chapter closes with a description of the basic control elements incorporated in the engine model.

2.1 Engine Model setup and validation

The propulsion engine was modelled using the NTUA in-house engine process simulation software MOtor THERmodynamics (MOTHER). MOTHER is a detailed zero-dimensional thermodynamic process simulation code, based on the control volume principle. The code has been successfully employed on predicting the transient and steady state performance of marine diesel engines (17; 58; 16; 59). A detailed description of the code methodology can be found in (15). The engine presently under consideration is a MAN Energy Solutions 6S50ME-C8.2 two stroke electronically controlled, uniflow scavenged marine diesel engine. The main particulars of the engine are shown in Table 2.1.

Table 2.1: Particulars of marine diesel engine

Engine Type	MAN B&W 6S50ME-C8.2	
Bore	500	mm
Stroke	2000	mm
No. of Cylinders	6	-
P_{MCR}	7620	kw
N_{MCR}	115.3	RPM
Firing Order	1-5-3-4-2-6	-
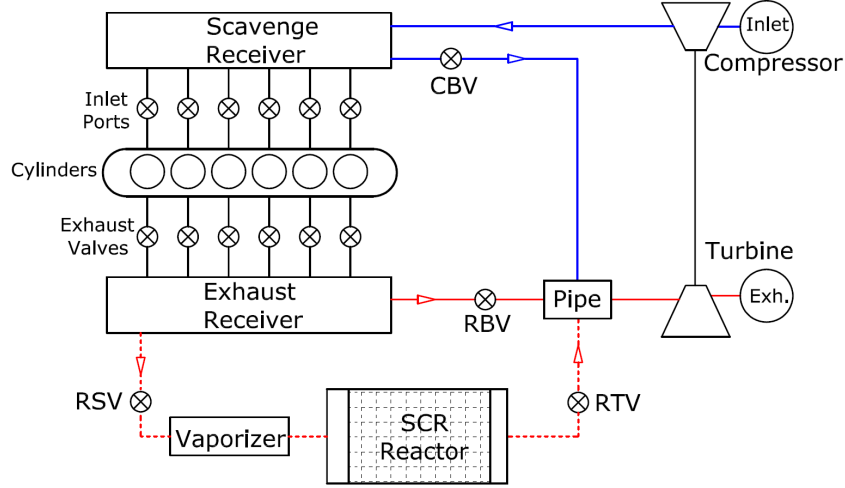
Figure 2-1: Diagram of the engine model

Figure 2-1 gives an overview of the model, showing the various control volumes and flow regulating valves. The engine model was validated in steady state conditions using available measurements from the engine Shop Trials. Shop trials are carried out at the engine maker's site, which is usually a shipyard and the engine is loaded using a water brake. Measurements were available at four engine loads, namely 25%, 50%, 75% and 100%. The parameters that were chosen to examine are listed below.

(i) Engine brake power(P_{br})

(ii) Turbocharger speed ($N_{T/C}$)

(iii) Compression pressure (p_{comp})

(iv) Maximum combustion pressure (p_{max})

(v) Scavenge receiver temperature (T_{scav})

(vi) Scavenge receiver pressure (p_{scav})

(vii) Exhaust receiver temperature (T_{exh})

(viii) Exhaust receiver pressure (p_{exh})

In Figure 2-2 model predictions are presented against measurements in Tier III operating mode. The model predicts brake engine power with less than 1% deviation over the examined load range. Model results for the rest of the parameters are also very close to measured values. Exhaust gas temperature was the hardest parameter to predict, nevertheless, deviation between predictions and measured values remained within acceptable limits. After submodel calibration, deviation between measurements and model predictions is less than 2.5% for all the parameters, over the examined load range. In-cylinder pressure prediction for the four engine loads is

presented in Figure 2-3 where simulated pressure traces are compared to measured ones. It is shown, that the engine model can predict the pressure evolution in the cylinders during compression, combustion and expansion phases with satisfactory accuracy.
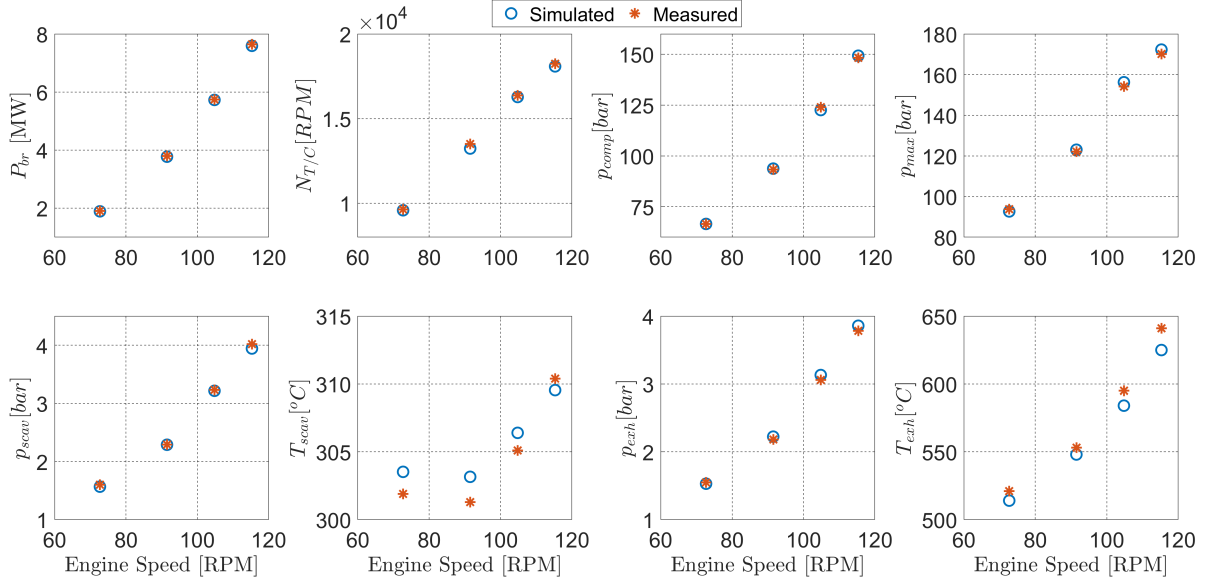
Figure 2-2: Model predictions against Shop Test measurements for various engine parameters at Tier III mode
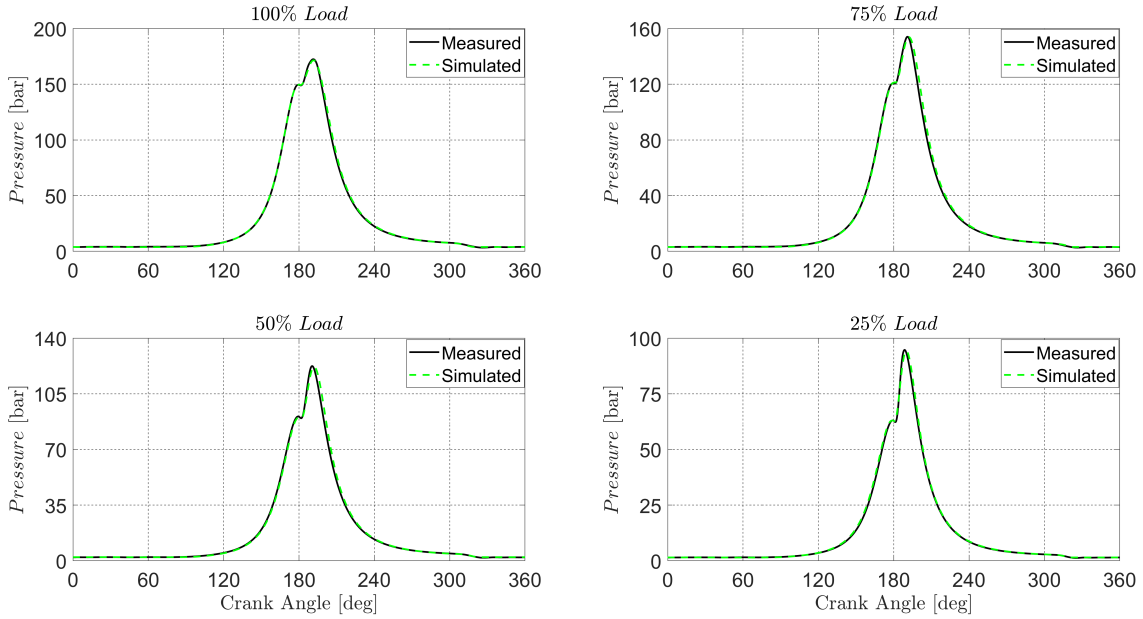
Figure 2-3: Measured cylinder pressure traces (solid lines) compared to simulated (dashed lines) for different engine load at Tier III operating mode

Engine combustion was modelled using the Woschni-Anisits combustion model (60), a phenomenological model used for direct injection diesel engines simulation. The model is based on the single S-curve equation and calculates the S-curve constants based on a reference point,

where the values of these constants are known. The single S-curve equation is given by:

$$\frac{m_{fb}}{m_{tot}} = 1 - e^{-\alpha(\frac{\theta - \theta_0}{\Delta\theta})^{m+1}} \tag{2.1}$$

The cranshaft angle at the start of combustion θ_0 is given by:

$$\theta_0 = \theta_{SOI} + \Delta\theta_{IND} + \Delta\theta_{IGD} \tag{2.2}$$

where θ_{SOI} is the crank angle at start of static injection, $\Delta\theta_{IND}$ is the injection delay(between delivery start of injection pump and start of injection) and $\Delta\theta_{IGD}$ is the ignition delay.

The gas to wall heat transfer coefficient was estimated using the relation proposed by Woschni (61). Woschni's equation is a widely used correlation for steady, turbulent heat transfer in the engine cylinders. The instantaneous spatial average heat transfer coefficient of cylinder gas is given by:

$$h = 0.00326 \cdot B^{-0.2} \cdot p^{0.8} \cdot T^{-0.55} \cdot w^{0.8} \tag{2.3}$$

where B is cylinder bore, p is cylinder gas pressure, T is cylinder gas temperature and w is average cylinder gas velocity.

Friction losses were calculated using the relation proposed by Mc Auly et al (62), which assumes that the total losses vary linearly with the peak pressure and with the piston speed. The friction mean effective pressure is determined using the following relation:

$$fmep = k_1 + k_2 \cdot p_{max} + k_3 \cdot \bar{v}_p \tag{2.4}$$

where p_{max} is the cylinder maximum combustion pressure, $\bar{v}_p$ is mean piston speed and k_1, k_2, k_3 are constants.

Engine scavenging was simulated using a detailed three zone scavenging model (63). In this model, the engine cylinders are divided in three zones namely, the pure air zone, mixing zone, and pure exhaust gas zone. The entrainment of air and exhaust gas in the mixing zone is specified by time varying mixing coefficients.

2.2   Auxiliary Blower Modelling

In marine two stroke engines, auxiliary blowers (A/Bs) are fitted to the engine in order to assist the compressor and deliver adequate amount of air in the engine, during part load or low load operation. The blowers are placed between the scavenge air cooler and the scavenge receiver and are driven by an electric motor operating at constant rotational speed. In Tier II engines, auxiliary blowers automatically start operating when the scavenge pressure drops below a predefined value (at about 30% engine load) and continue operating until the scavenge pressure exceeds a value corresponding to about 40% engine load. In engines coupled to a SCR system, auxiliary blowers are further used to supply the turbine with sufficient enthalpy and prevent thermal instability of the engine-turbocharger system (11). Different modelling methods of auxiliary blowers may be found in (20; 23; 42). In this work, the compressor-blower system was modelled as two in series compressors. A sketch of the modelling configuration is shown in Figure 2-4. When p_{scav} is higher than the blower activation pressure, virtual valve
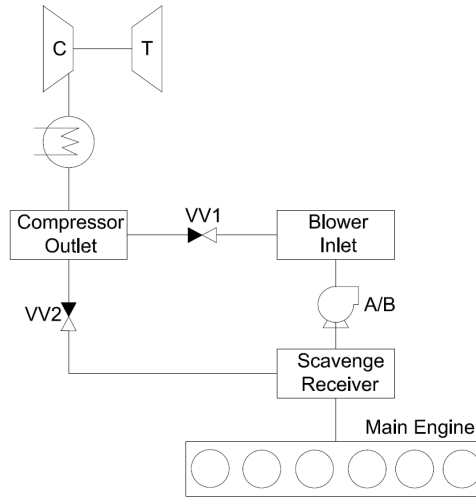
Figure 2-4: Sketch showing the blower modelling configuration

No.1 (VV1) is closed and virtual valve No.2 (VV2) is open, isolating the auxiliary blower from the air path. When p_{scav} is lower than the blower activation pressure, VV1 opens and VV2 closes guiding the air exiting the compressor through the A/B. There was little information about the performance of the auxiliary blower. Two operating points of volumetric flow and static pressure increase at the nominal blower operating speed were provided. The blower static pressure increase can be expressed as a quadratic function of the volumetric flow rate as in Eq. (2.5). Using this relation, the single iso-speed curve of the auxiliary blower can be constructed.

No other curves are needed since the blower operates at constant rotational speed.

$$\Delta p_{bl} = c_{bl,1} + c_{bl,2} \cdot \dot{V} + c_{bl,3} \cdot \dot{V}^2 \tag{2.5}$$

2.3   Compressor Map Extrapolation

Compressor maps provided by compressor makers typically cover the compressor operating area from 30% to 100% load. In order to be able to simulate engine operation at lower loads the compressor map should be extrapolated at lower compressor speed regions. The extrapolation was based on the non-dimensional flow coefficient Φ and isentropic head coefficient Ψ.

$$\Phi = \frac{\dot{V}_C}{A_C \cdot U_C} \tag{2.6}$$

$$\Psi = \frac{\pi_C^{\frac{\gamma-1}{\gamma}} - 1}{(\gamma - 1) \cdot M_{tip}^2} \tag{2.7}$$

Where $\dot{V}_C$ is the air volumetric flow rate entering the compressor, A_C is the compressor inlet area, U_C is the compressor blade tip velocity, π_C is the compressor pressure ratio and M_{tip} is the compressor impeller tip Mach number defined as:

$$M_{tip} = \frac{U_C}{\sqrt{\gamma R \cdot T_{amb}}} = \frac{\pi N_{T/C} D_C}{60\sqrt{\gamma R \cdot T_{amb}}} \tag{2.8}$$

where γ is the heat capacity ratio, R is the gas constant and D_C is the compressor impeller diameter. The non-dimensional flow coefficient Φ can be expressed as a function of Ψ and M_{tip} using the relation proposed by (64) :

$$\Phi = \frac{k_1 + k_2 M_{tip} + k_3\Psi + k_4 M_{tip}\Psi}{k_5 + k_6 M_{tip} - \Psi} \tag{2.9}$$

As far as the compressor isentropic efficiency is concerned, it can be expressed as a second order polynomial of Φ and a first order polynomial of M_{tip} as Eq. (2.10) shows.

$$\eta_{is,C} = u_1 + u_2\Phi + u_3 M_{tip} + u_4\Phi^2 + u_5\Phi M_{tip} \tag{2.10}$$

The $k_1 - k_6$ and $u_1 - u_5$ coefficients were calculated using the Matlab Curve Fitting Toolbox (65). The exact procedure followed for the extrapolation of the compressor map is outlined in

(23). The original and extrapolated compressor performance map is shown in Figure 2-5.
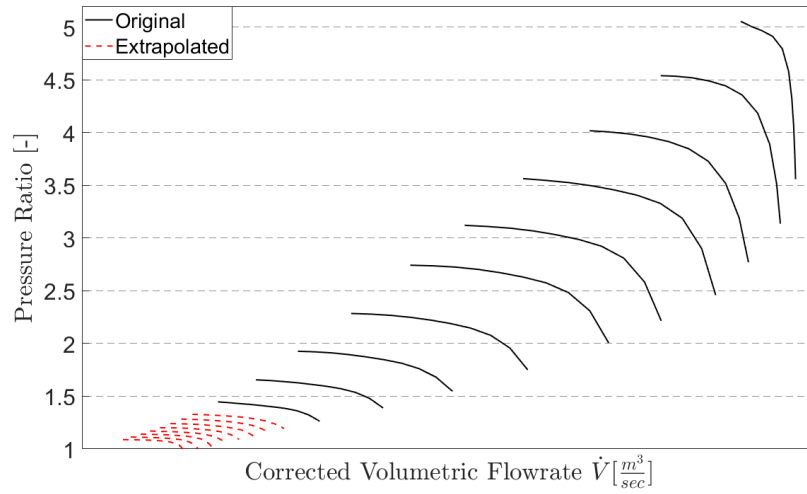
Figure 2-5: Original and extrapolated compressor performance map

2.4   Validation of the extrapolation method

No experimental data at the lower speed region of the compressor map were available. In order to evaluate the accuracy of the extrapolation method, it was used to predict the three lower existing iso-speed curves of the compressor map. Extrapolation results are compared with the original curves in Figures 2-6 and 2-7. The original curves are shown with solid lines while the ones calculated using the extrapolation method are shown with dashed lines. The prediction of iso-speed lines is very good and prediction of isentropic efficiency is also decent. Hence, the lower regions of the compressor map can be predicted with satisfactory accuracy using this extrapolation methodology.
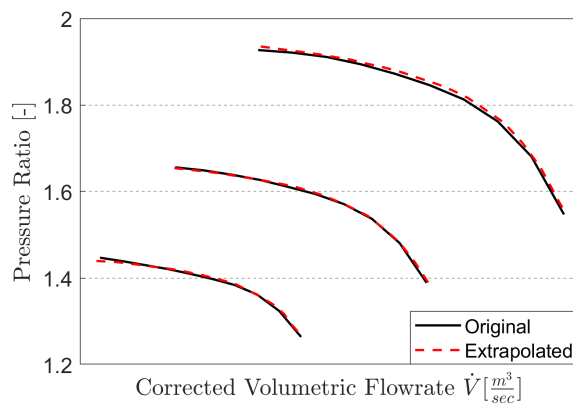
Figure 2-6: Original and extrapolated compressor iso-speed curves
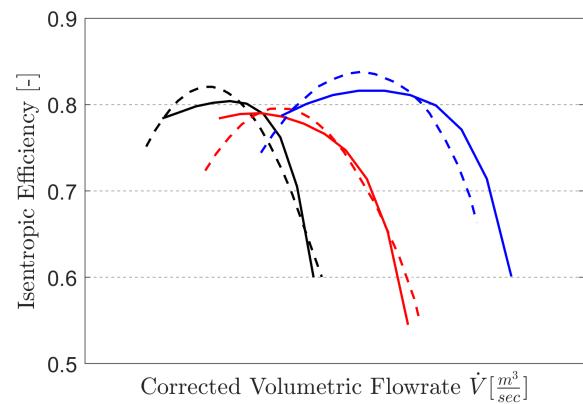
Figure 2-7: Original (solid lines) and extrapolated (dashed lines) compressor isentropic efficiency curves

2.5   Shaft Dynamics

The instantaneous crankshaft rotational speed is determined using the following differential equation:

$$\frac{d\omega_{eng}}{dt} = \frac{Q_{br} - Q_p}{I_{eng} + I_p + I_{ent}} \tag{2.11}$$

Where Q_{br} is the brake engine torque, Q_p is the propeller torque, I_{eng} is the engine and crankshaft inertia, I_p is the propeller dry inertia and I_{ent} is the water entrained propeller inertia. The propeller dry inertia is calculated using the methodology described in (66) and I_{ent} is calculated using the regression model described by Parsons for the Wageningen B-Series propellers in (67).

2.6   Control Elements

Engine control schemes constitute of two different Proportional-Integral-Derivative (PID) type controllers. The output of the PID controller in the time domain is given by the following equation:

$$Y = K_p e(t) + \frac{K_i}{T_i} \int_0^t e(t)dt + K_d T_d \frac{de(t)}{dt} \tag{2.12}$$

Where K_p , K_i and K_d are the proportional, integral and derivative gains respectively and $e(t)$ is the error value. The first controller is a speed governor, i.e. it regulates the engine rotational speed having the fuel index as the control input. The second controller, regulates the position of the Cylinder Bypass Valve (CBV) of the SCR system, ensuring that exhaust gas temperature at the reactor inlet will remain above 300 ^oC and the ABS formation reaction will be suppressed. When valve CBV is open, a fraction of compressed air from the scavenge receiver bypasses the engine cylinders and is directed to the turbine inlet. In this way, combustion becomes richer and exhaust gas temperature increases. In the speed governor control scheme, K_d equals to zero (PI controller) and the error is defined as:

$$e_{sg}(t) = N_{ord}(t) - N_{eng}(t) \tag{2.13}$$

while in the case of SCR inlet temperature control:

$$e_{cbv}(t) = T_{set}(t) - T_{reac,in}(t) \tag{2.14}$$

Over-torque and scavenging limiters, as provided by the engine makers, are also incorporated in the speed governor control scheme. Limiters are incorporated in modern electronically controlled marine diesel engines in order to protect them against consequences of off-design operation. A limiter is an upper or lower limit of fuel index position as a function of engine speed (torque limiter) and scavenge pressure (scavenge pressure limiter). Its effect is imposed directly on the control action, i.e. on the fuel index (68).

THIS PAGE INTENTIONALLY LEFT BLANK

Chapter 3

SCR System Model

A zero dimensional model was developed to simulate the temperature dynamics of the SCR system. The present chapter gives a detailed presentation of the developed SCR model, as well as the validation that was carried out using available experimental data. In this model, the SCR system is divided in its three primary components namely: vaporizer, SCR reactor and connecting pipes. Each component may be divided into further control volumes. The inputs to the model are the exhaust gas temperature, pressure and massflow rate at the SCR inlet, the heat capacity of exhaust gases and the mass flow rate of the reducing agent. The output of the model is the exhaust gas temperature at the outlet of the SCR system. In addition, the geometric characteristics of each component are required as input to the model. The model configuration as well as model inputs and outputs are shown in Figure 3-1. The basic model assumptions are listed below:

(i) Flow is assumed to be incompressible.

(ii) Axial heat conduction in the gas can be neglected without the introduction of significant errors as mentioned in (29).

(iii) The flow in the catalyst channels is laminar (69). According to (13) this is true for the full practical range of real-world operating conditions.

(iv) Thermal properties of urea are ignored since the mass of urea injected was less than 0.3% of exhaust gas massflow in all cases. Hence, the composition of exhaust gas-urea mixture can be assumed to be mainly exhaust gas.

(v) All components (vaporizer, pipe and reactor) are insulated.
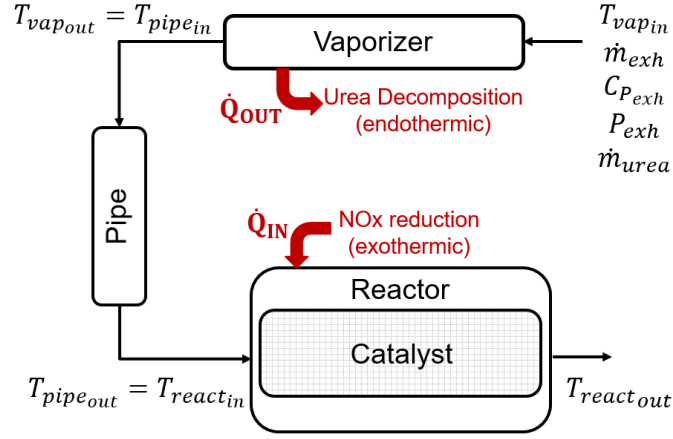
Figure 3-1: Sketch of the SCR model showing the inputs, outputs and different components

3.1   Vaporizer and Pipe Submodel

The exhaust gas and wall temperature at each control volume is calculated using an Euler step method as equations (3.1) and (3.2) show. In each volume j, the temperature at sample instance k+1 is calculated using the temperature and temperature differential calculated at sample instance k.

$$T_{exh,k+1} = T_{exh,k} + \left(\frac{dT}{dt}\right)_{exh,k} \cdot \Delta t \tag{3.1}$$

$$T_{wall,k+1} = T_{wall,k} + \left(\frac{dT}{dt}\right)_{wall,k} \cdot \Delta t \tag{3.2}$$

The temperature gradient of the exhaust gas and the wall, for control volume j is calculated using the conservation of energy at each control volume. The energy flow in the vaporizer is schematically shown Figure 3-2.

Figure 3-2: Energy flow in a control volume of the vaporizer

3.1.1   Gas temperature calculation

The energy dynamics of the exhaust gas at each control volume of the vaporizer can be described by the following equations:

$$\left(\frac{dE}{dt}\right)_{exh} = m_{exh}c_{exh}\left(\frac{dT}{dt}\right)_{exh} \tag{3.3}$$

$$\left(\frac{dE}{dt}\right)_{exh} = \dot{Q}_{in} - \dot{Q}_{g\rightarrow w} - \dot{Q}_{ch,vap} \tag{3.4}$$

The first term of Eq. (3.4) $\dot{Q}_{in}$, accounts for exhaust gas mixing between two adjacent control volumes. It is assumed that exhaust gas mixing for control volume j only takes place with the preceding volume (j-1). The second term $\dot{Q}_{g\rightarrow w}$, accounts for convective and radiative losses from the gas to the wall and the third term $\dot{Q}_{ch,vap}$, accounts for the energy loss due to the endothermic reaction of urea decomposition. Urea decomposition is assumed to take place only in the vaporizer. Hence, modelling of the pipe is done in exactly the same way, except $\dot{Q}_{ch,vap} = 0$. The two heat flows $\dot{Q}_{in}$ and $\dot{Q}_{g\rightarrow w}$ are modelled by the following equations:

$$\dot{Q}_{in} = \dot{m}_{exh}c_{exh}(T_{exh,j-1} - T_{exh,j}) \tag{3.5}$$

$$\dot{Q}_{g\rightarrow w} = h_{exh}A_{gw}(T_{exh,j} - T_{wall,j}) + \sigma\epsilon A_{gw}(T_{exh,j}^4 - T_{wall,j}^4) \tag{3.6}$$

Where $\dot{m}_{exh}$, is the massflow of exhaust gas entering each control volume, h_{exh} is the convective heat transfer coefficient between the wall and exhaust gas and A_{gw} is the inner surface area of the wall in contact with the gas. The mass of exhaust gas in each control volume is calculated using the ideal gas state equation. The temperature gradient $\left(\frac{dE}{dt}\right)_{exh}$ is calculated by dividing the right side of Eq. (3.4) with the term $\dot{m}_{exh}c_{exh}$ yielding the following expression for the exhaust gas temperature dynamics in the vaporizer/pipe.

$$\left(\frac{dT}{dt}\right)_{exh,j} = C_1(T_{exh,j-1} - T_{exh,j}) - C_2(T_{exh,j} - T_{wall,j}) - C_3(T_{exh,j}^4 - T_{wall,j}^4) - dT_{ch,vap} \tag{3.7}$$

The coefficients shown in 3.7 are calculated as in Appendix A.

3.1.2   Wall temperature calculation

The energy content of the wall changes due to the energy exchange between the gas and the wall as well as due to losses to the environment. Hence, the following equations hold:

$$\left(\frac{dE}{dt}\right)_{wall} = m_{wall}c_{wall}\left(\frac{dT}{dt}\right)_{wall} \tag{3.8}$$

$$\left(\frac{dE}{dt}\right)_{wall} = \dot{Q}_{g \to w} - \dot{Q}_{env} \tag{3.9}$$

Where $\dot{Q}_{g \to w}$ is calculated as in Eq. (3.6) and $\dot{Q}_{env}$ is calculated as below:

$$\dot{Q}_{env} = \frac{T_{wall,j} - T_{amb}}{R_{\theta,wall} + R_{\theta,ins} + R_{\theta,env}} \tag{3.10}$$

Where m_{wall} is the wall mass, $R_{\theta,wall}$ and $R_{\theta,ins}$ are thermal resistances of conduction through the wall and insulation respectively and $R_{\theta,env}$ is the thermal resistance for convection to the environment. The first term of Eq. (3.9) accounts for the heat transferred to the wall from the gas due to convection and radiation and the second term accounts for heat losses from wall to ambient. The radiation losses from the insulation to ambient were neglected due to the relatively low temperature of the outer surface of the insulation. The amount of heat transferred through radiation increases as a quadratic function of temperature, hence for low temperatures it can be neglected. However, unless the vaporizer/pipe is insulated, the radiative heat loss from wall to ambient is not negligible and should be taken into account. The wall temperature gradient can be obtained by dividing the right side of Eq. (3.9) with the term $m_{wall}c_{wall}$.

$$\left(\frac{dT}{dt}\right)_{wall,j} = C_4(T_{exh,j} - T_{wall,j}) + C_5(T_{exh,j}^4 - T_{wall,j}^4) - C_6(T_{wall,j} - T_{amb}) \tag{3.11}$$

3.2   Reactor Submodel

The exhaust gas, catalyst block and wall temperature in the SCR reactor is calculated as in Eqs. (3.1) and (3.2). A catalyst component is inserted in order to model the reactor's thermal inertia. The energy flow inside the reactor is schematically shown in Figure 3-3.
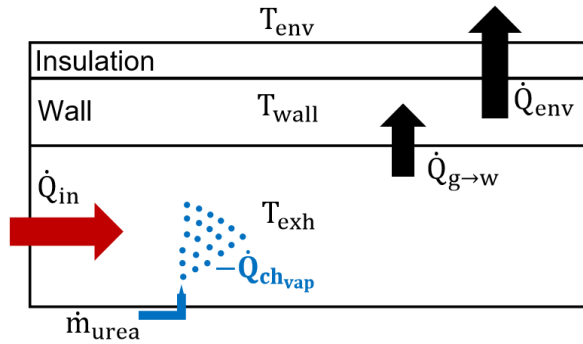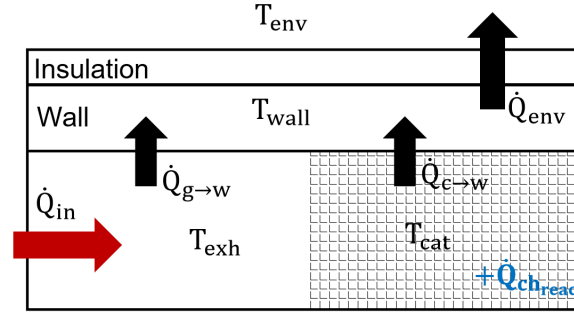
Figure 3-3: Energy flow in a control volume of the reactor

3.2.1 Gas temperature calculation

For the energy dynamics of the exhaust gas inside the SCR reactor the following equations hold:

$$\left(\frac{dE}{dt}\right)_{exh} = m_{exh}c_{exh}\left(\frac{dT}{dt}\right)_{exh} \tag{3.12}$$

$$\left(\frac{dE}{dt}\right)_{exh} = \dot{Q}_{in} - \dot{Q}_{g\to w} - \dot{Q}_{g\to c} + \dot{Q}_{ch,reac} \tag{3.13}$$

The first term of Eq. (3.13) $\dot{Q}_{in}$, accounts for mixing of exhaust gas between two adjacent control volumes and is calculated as in Eq. (3.5). The second term $\dot{Q}_{g\to c}$, represents convective and radiative losses from the gas to the catalyst block. The third term $\dot{Q}_{g\to w}$, represents convective and radiative losses from the gas to the wall and the fourth term $\dot{Q}_{ch,reac}$, accounts for the energy added to the gas due to the exothermic SCR reactions. As it is shown in Figure 3-4, the catalyst does not span throughout the reactor length. Usually there are two or three separate catalyst blocks. Hence, both heat losses to the catalyst and the wall should be taken into account.
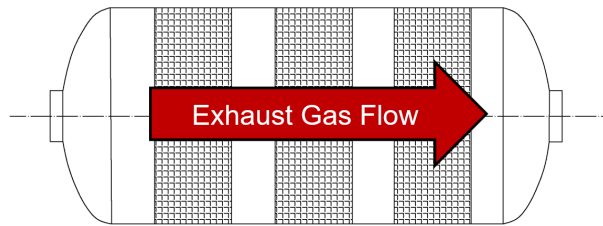
Figure 3-4: Sketch of a marine SCR reactor with its catalyst blocks

The two heat flows $\dot{Q}_{g\to c}$ and $\dot{Q}_{g\to w}$ are modelled by the following equations.

$$\dot{Q}_{g\to c} = h_{cat}A_{cat}(T_{exh,j} - T_{cat,j}) + \sigma\epsilon A_{cat}(T_{exh,j}^4 - T_{cat,j}^4) \tag{3.14}$$

$$\dot{Q}_{g\to w} = h_{exh}A_{gw}(T_{exh,j} - T_{wall,j}) + \sigma\epsilon A_{gw}(T_{exh,j}^4 - T_{wall,j}^4) \tag{3.15}$$

Where h_{cat} is the convective heat transfer coefficient between the catalyst block and the gas, A_{cat} is the total catalyst surface area in contact with the gas and A_{gw} is the total wall surface area in contact with the gas. Similarly with Eq. (3.7), the temperature gradient of the exhaust gas can be calculated as below:

$$\left(\frac{dT}{dt}\right)_{exh,j} = C_7(T_{exh,j-1} - T_{exh,j}) - C_8(T_{exh,j} - T_{cat,j}) - C_9(T_{exh,j} - T_{wall,j})$$
$$- C_{10}(T_{exh,j}^4 - T_{cat,j}^4) - C_{11}(T_{exh,j}^4 - T_{wall,j}^4) + dT_{ch,reac} \tag{3.16}$$

The Nusselt number inside the catalyst cells is calculated using a semi-empirical correlation applicable to laminar flow in square ducts proposed by (13).

$$Nu = 2.976\left(1 + 0.095 \cdot \frac{Re_{cell} \cdot Pr_{cell} \cdot d_h}{L_{cat}}\right)^{0.45} \tag{3.17}$$

3.2.2 Catalyst block temperature calculation

The conservation of energy for each catalyst block control volume can be expressed as:

$$\left(\frac{dE}{dt}\right)_{cat} = m_{cat}c_{cat}\left(\frac{dT}{dt}\right)_{cat} \tag{3.18}$$

$$\left(\frac{dE}{dt}\right)_{cat} = \dot{Q}_{g\to c} - \dot{Q}_{c\to w} \tag{3.19}$$

The first term of Eq. (3.19) $\dot{Q}_{g\to c}$, accounts for the heat flow from the gas to the catalyst block through convection and radiation and is modelled as in (3.14). The second term $\dot{Q}_{c\to w}$, accounts for the heat flow from the catalyst block to the reactor wall through conduction and is modelled as follows:

$$\dot{Q}_{c\to w} = \frac{T_{cat,j} - T_{wall,j}}{R_{\theta,c\to w}} \tag{3.20}$$

Where $R_{\theta,c\to w}$, is the thermal resistance for conductive heat transfer between the catalyst block and the wall. The total catalyst surface area in contact with the gas is calculated using the specific surface area A_{spec} $[m^2/m^3]$ which is a characteristic catalyst value and is provided by the catalyst maker.

$$A_{cat} = A_{spec}V_{cat} \tag{3.21}$$

The temperature dynamics of the catalyst block can be obtained by dividing the right side of Eq. (3.19) with the term $m_{cat}c_{cat}$ yielding the following expression.

$$\left(\frac{dT}{dt}\right)_{cat,j} = C_{12}(T_{exh,j} - T_{cat,j}) + C_{13}(T^4_{exh,j} - T^4_{cat,j}) - C_{14}(T_{cat,j} - T_{wall}) \tag{3.22}$$

3.2.3   Wall temperature calculation

The energy dynamics for the reactor wall can be described by the following equations:

$$\left(\frac{dE}{dt}\right)_{wall} = m_{wall}c_{wall}\left(\frac{dT}{dt}\right)_{wall} \tag{3.23}$$

$$\left(\frac{dE}{dt}\right)_{wall} = \dot{Q}_{g \rightarrow w} + \dot{Q}_{c \rightarrow w} - \dot{Q}_{env} \tag{3.24}$$

Where, the three terms of Eq. (3.24) are modelled as per Eq. (3.15), (3.20), (3.10) respectively. Similarly with Eq. (3.11) the temperature gradient of the wall can be calculated as follows:

$$\left(\frac{dT}{dt}\right)_{wall,j} = C_{15}(T_{exh,j} - T_{wall,j}) + C_{16}(T^4_{exh,j} - T^4_{wall,j}) + C_{17}(T_{cat,j} - T_{wall,j}) - C_{18}(T_{wall,j} - T_{amb}) \tag{3.25}$$

3.3   Chemical Reactions Modelling

The energy lost or added due to chemical phenomena in the vaporizer and the reactor was modelled using correlations derived from available measured data. Steady state datasets under the same engine load, with and without the injection of reducing agent were used in order to quantify the effect of chemical phenomena on the exhaust gas temperature. It was noticed that the effect increased with increasing reducing agent mass flow and engine load. This was modelled with the terms $dT_{ch,vap}$ and $dT_{ch,reac}$ in Eqs. (3.7) and (3.16) respectively.

$$dT_{ch,vap} = 0.034 \cdot Load + 240 \cdot \dot{m}_{urea} \tag{3.26}$$

$$dT_{ch,reac} = 0.07 \cdot Load + 78 \cdot \dot{m}_{urea} \tag{3.27}$$

Where Load is engine load $\in$ (0-100) and urea massflow units are [kg/s]. An aqueous solution of 40% urea was used as a reducing agent. The temperature reduction of the exhaust gas in the vaporizer was found to be around 2-7 ^oC, while the temperature increase in the reactor was around 4-17 ^oC depending on engine load.

3.4   SCR Model Validation

The model was validated by comparing model results to measured data from a full scale engine
and SCR testbed. Data from tests carried out on a MAN B&W 4S50ME test engine at the
Hitachi-Zosen facilities were used for validation. The main characteristics of the SCR and the
engine are shown in Table 3.1. The validation of the model is performed by comparing model

Table 3.1: Engine and SCR testbed characteristics

MAN B&W 4S50ME test engine		
Engine Power	7120	kW
Engine Speed	117	RPM
Stroke	2214	mm
Bore	500	mm
No. of Cylinders	4	-
Vaporizer		
Length	5.68	m
Diameter	0.85	m
Insulation thickness	0.125	mm
Connecting Pipe		
Length	3.4	m
Diameter	0.54	m
Insulation thickness	0.125	mm
SCR Reactor		
Length	5.7	m
Diameter	1.85	m
Insulation thickness	0.15	mm
Catalyst Mass	2080	kg
Catalyst specific area	770	m^2 /m^3
Catalyst Volume	4.02	m^3

predicted temperatures against measurements in three locations of the SCR system: vaporizer
outlet, reactor inlet and reactor outlet. Time series of measured SCR inlet temperature, exhaust
gas massflow, exhaust gas pressure and urea flow were used as input to the model.   The
transient thermal response of the SCR system is presented for three different operating conditions
namely, low load operation where temperature oscillations are present, engine acceleration and
deceleration.

3.4.1   SCR thermal response during low load temperature oscillations

Figure 3-5 shows measured timeseries of engine load and SCR temperatures against model
predictions during low load oscillations. Measurements are shown with blue colour and model
predictions are shown with red colour. Even though load fluctuations are small, fluctuations

of exhaust gas temperature are quite pronounced with an amplitude of 40 ^{o}C. The reactor inlet temperature follows the vaporizer outlet oscillation with the same period. The reactor outlet temperature (turbine inlet temperature) oscillates with the same period but with a phase difference of T/4 equal to about 200 s. This means that the time delay that the reactor imposes to the engine-turbocharger system is around 200 s. Hence, the turbine will react to an increase in engine load with a 200 s delay. The model manages to accurately predict the SCR temperature dynamics in both amplitude and period of oscillations as well as the filtering effect of the reactor (reduction in oscillation amplitude), during low load oscillations.
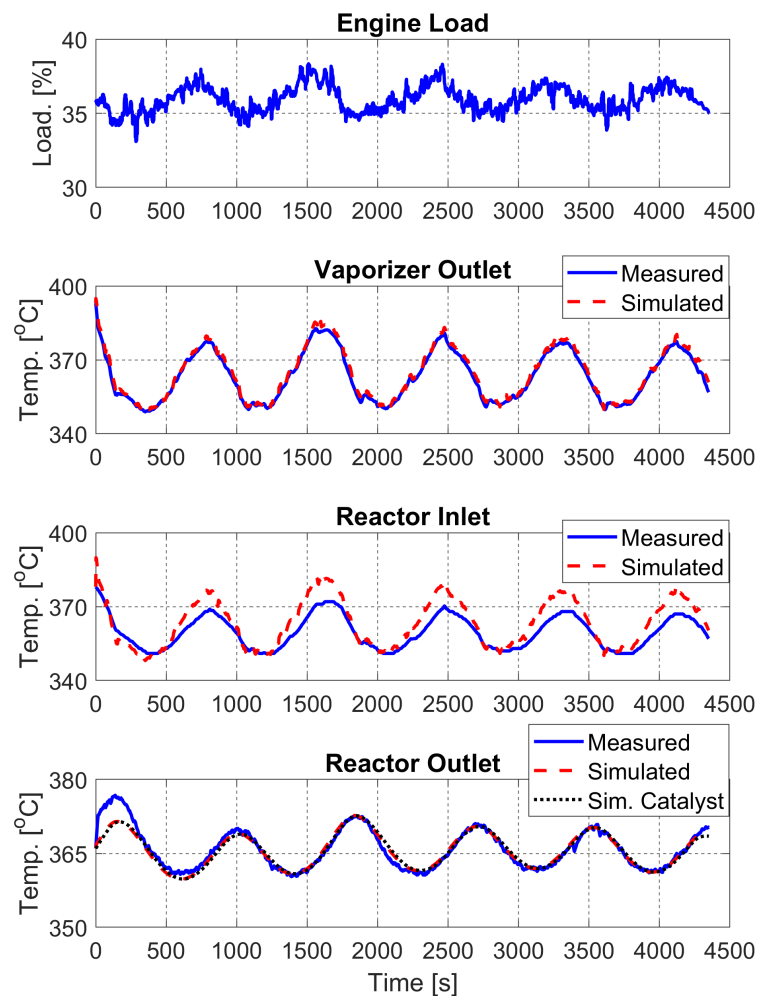
Figure 3-5: Model predicted and measured SCR temperatures during low load oscillations

3.4.2 SCR thermal response during deceleration

The SCR thermal response during a deceleration from 45% to 35% was examined. Measured timeseries of engine load and SCR temperatures are presented in Figure 3-6. At about 300 s there is a load spike (red circle), which is almost immediately rendered into a fluctuation in

exhaust gas temperature. On the other hand, the temperature variation in the reactor outlet temperature is much smoother and lasts longer (red ellipse). Then, the engine operates at steady 45% load until 1800 s, when there is another load spike followed by a sudden deceleration until 35% load. The reactor outlet temperature follows the reactor inlet temperature profile, with a reduced amplitude and a time delay. This time delay can be seen in more detail in Figure 3-7 where the measured and simulated reactor inlet and outlet temperatures of the same dataset are presented. In order get an estimate of the time delay, characteristic events of the temperature variation are compared, such as temperature crests and troughs (see dotted lines at Figure 3-7).
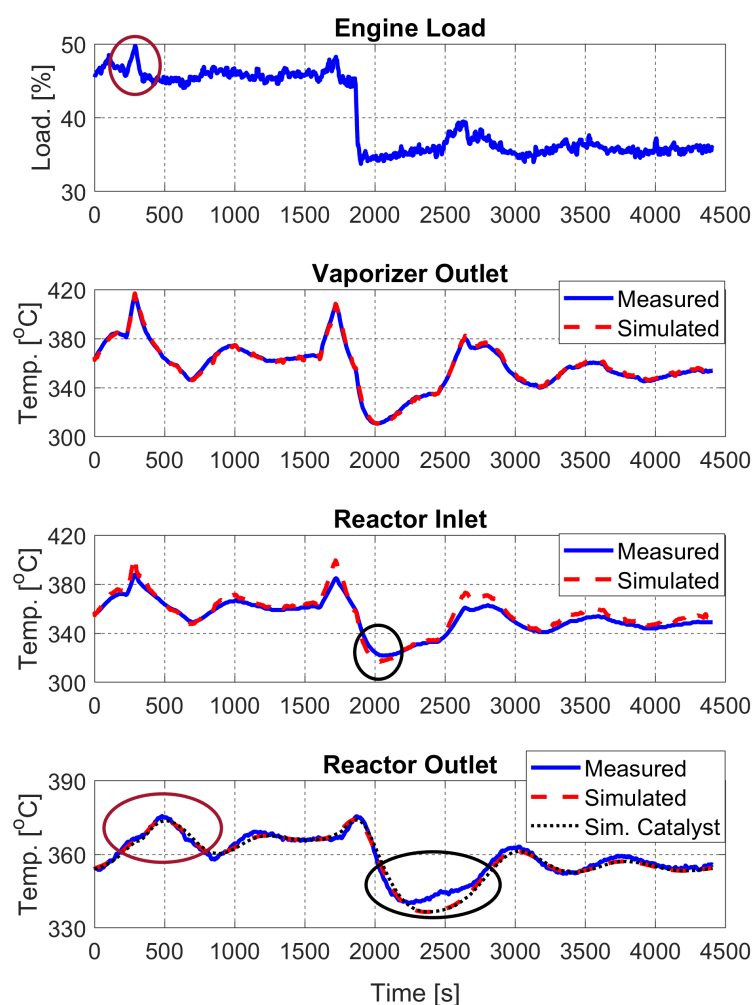
Figure 3-6: Model predicted and measured SCR temperatures during engine deceleration

The time delay due to the presence of the reactor is found to be around 200 s at this engine load. At about 2500 s there is a slight load fluctuation after which, the engine operates at almost steady load. The model accurately simulates the time delay imposed by the reactor. Accurate prediction of the reactor inlet temperature (and hence accurate input to reactor submodel) is

crucial for the accuracy of the reactor outlet temperature. As it can be observed from Figures 3-6 and 3-7, model predicted reactor inlet temperatures show a slightly less smooth behavior than the measured ones. For example, during engine deceleration at about 2000 s, the model underestimates the reactor inlet temperature (black circle). The erroneous input to the reactor leads to further errors in the reactor outlet temperature prediction (black ellipse).
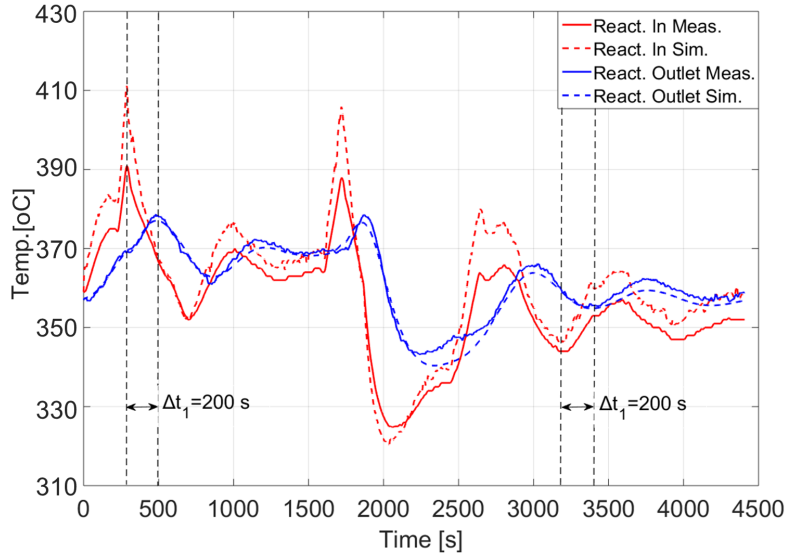
Figure 3-7: Measured reactor inlet and reactor outlet temperature during deceleration

3.4.3   SCR thermal response during acceleration

The thermal response of the SCR system during acceleration is also examined. In this case data for the engine accelerating from 25% to 50% load at about 100 s and then to 75% engine load at about 650 s were used. Model predicted SCR temperatures during acceleration are presented in Figure 3-8. The reactor outlet temperature increases much slower than the reactor inlet temperature due to the enthalpy loss of the exhaust gases in the reactor (the exhaust gases heat the catalyst). The measured and model predicted, reactor inlet and outlet temperatures are shown in a common graph in Figure 3-9. It is observed that the reactor inertial effect in the engine-turbocharger system decreases with increasing engine load. As the engine load increases (hence the exhaust gas mass flow and temperature increase) the reactor is heated faster, due to the higher massflow of the exhaust gases.

This varying thermal inertia or "time constant" can be explained by examining the model equations. The C_7 coefficient in Eq. (3.16) is proportional to the exhaust gas massflow. The "time constant" is inversely proportional to C_7 and hence inversely proportional to massflow.
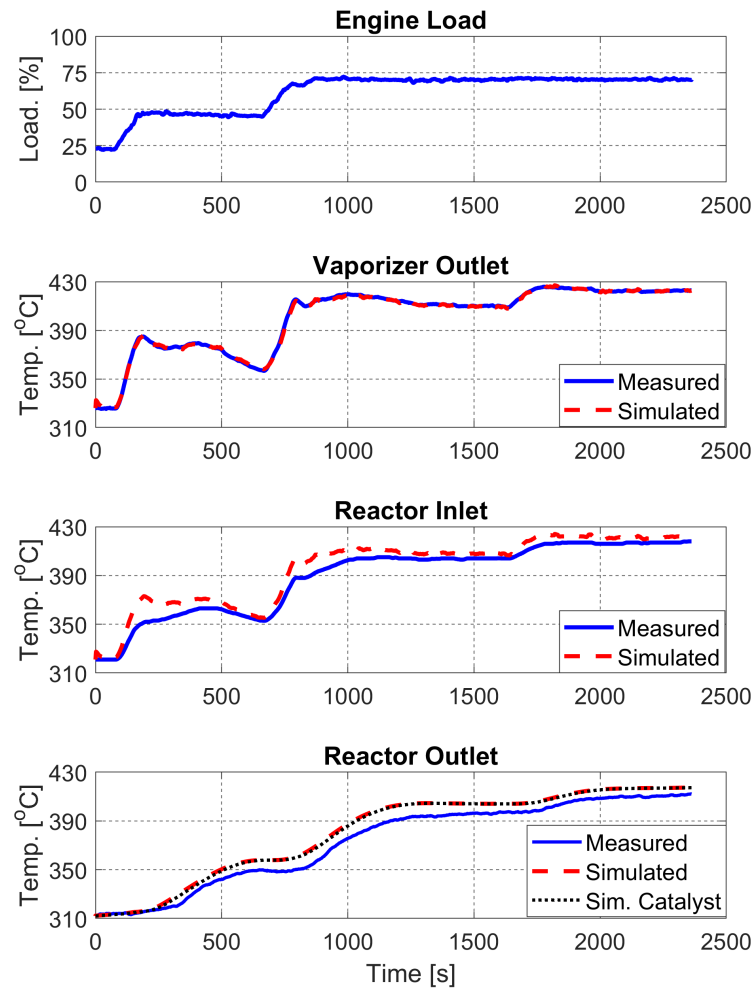
Figure 3-8: Model predicted and measured SCR temperatures during engine acceleration
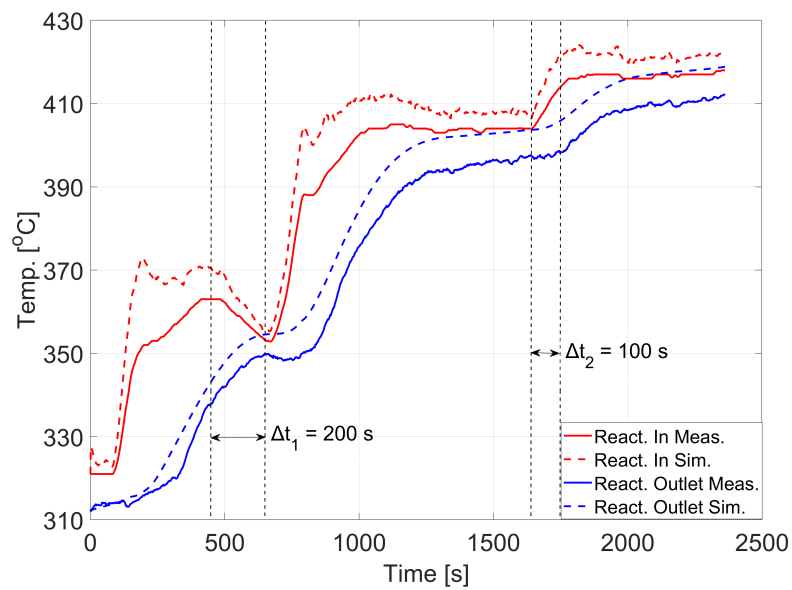
Figure 3-9: Reactor inlet and outlet temperature during acceleration from 25% to 75% load

Hence, a larger exhaust gas massflow through the SCR results in smaller inertial effect of the reactor in the engine-turbocharger system. In low engine loads (40%) the time delay between the engine and the turbocharger due to the presence of the reactor was found to be around 200 s, while in higher loads (75%) it was around 100 s. Hence, in high engine loads the engine-turbocharger system is less affected by the presence of the reactor. This is the reason, why thermal oscillations emerge only during low load operation, where the effect is more significant.

3.5   Effect of different parameters on SCR thermal response

An analysis was carried out in order to assess the effect of different parameters on the thermal response of the SCR system. The variables that were chosen for the analysis were the mass flow rate of exhaust gases, catalyst mass, catalyst volume and insulation thickness of the SCR reactor. The loading scenario that was chosen for the analysis is the low load scenario presented in Section 3.4.1. In order to quantify the effect of each variable on the thermal response of the SCR system two performance indexes were used. The first index, accounts for the effect of each parameter on the time delay (Δt) that the SCR system imposes to the engine-turbocharger system. The second index examines how the variation of each parameter influences the amplitude of temperature oscillations, i.e. the filtering effect of the SCR reactor. An example of how the indexes are determined is shown in Figure 3-10, where model predicted reactor outlet temperature is presented for different values of catalyst mass. A reduction of catalyst mass causes a shift of reactor outlet temperature to the left and an increase in the amplitude of temperature
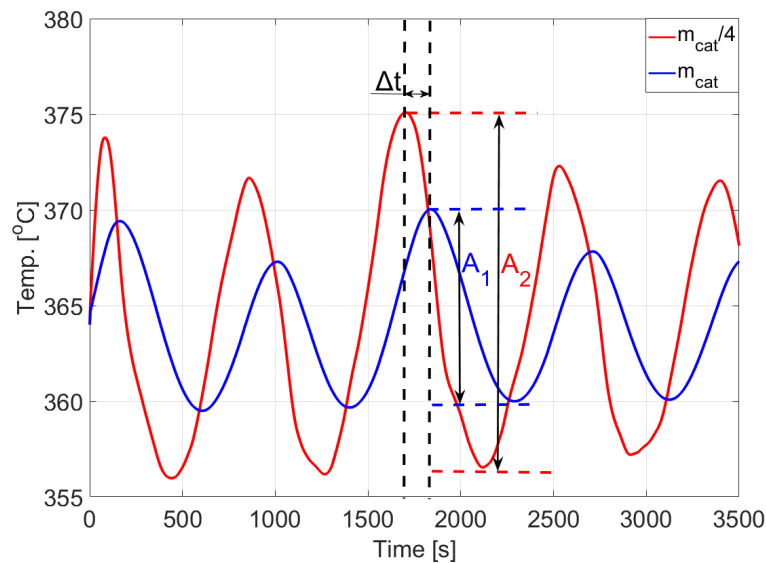
Figure 3-10: Model predicted reactor outlet temperature for different values of catalyst mass

Table 3.2: Range of values for the analysis

	Lower Limit	Initial Value	Upper Limit
$\dot{m}_{exh}[kg/sec]$	1.6	6.5	25.9
$m_{cat}[kg]$	520	2080	8320
$V_{cat}[m^3]$	1.01	4.02	16.08
$t_{ins}[m]$	0.04	0.15	0.6

oscillations (A2>A1). The range of the values for each parameter is shown in Table 3.2. Since the exhaust gas mass flow rate is a time series and hence cannot be characterized by a single number, the mean value of exhaust gas massflow is given in Table 3.2. Results of the analysis are shown in Figure 3-11 where the calculated performance indexes for every investigated parameter are shown. Exhaust gas mass flow and catalyst mass are the parameters of higher influence on the SCR thermal response. An increase of exhaust gas mass flow, causes the SCR system to respond faster and increases the amplitude of temperature oscillations. On the other hand, an increase of catalyst mass makes the SCR respond slower and increases the reactor filtering effect (i.e. decreases the amplitude of temperature oscillations). The catalyst volume has a less significant effect, making the reactor respond faster for values smaller than the initial, and having no significant effect for values greater than the initial. Finally, the insulation thickness has little effect on the SCR thermal response.
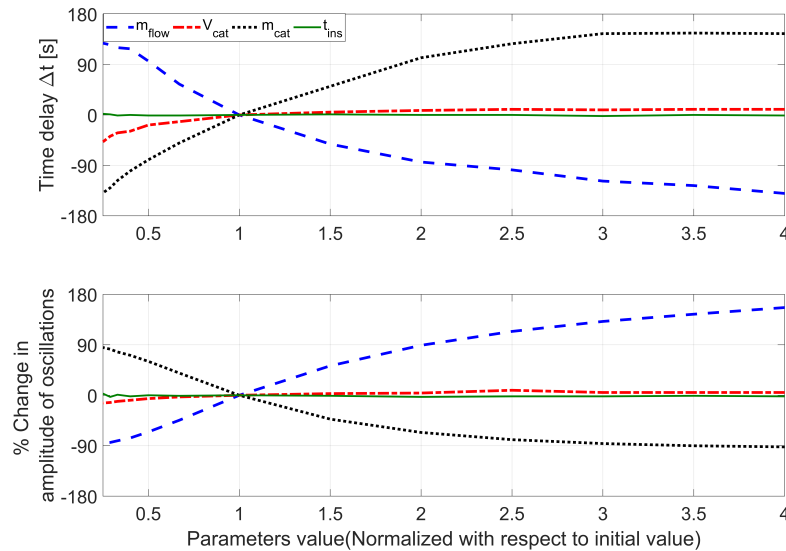
Figure 3-11: Results of performance indexes for various values of the parameters

Chapter 4

Propeller and Ship Hull Model

In the context of this thesis the response of a two-stroke marine propulsion engine with a SCR exhaust aftertreatment system is investigated in transient loading conditions. The load that the engine has to overcome is essentially the torque demanded by the propeller. In transient conditions, i.e. when engine rotational speed or vessel speed varies, the instantateous load of the engine cannot be known a priori, but is dependent on the interraction between the engine, the propeller and the ship's hull. In order to obtain an accurate prediction of propeller produced thrust, demanded torque and vessel speed, propeller and ship hull models were implemented and integrated with the engine and SCR models. In this chapter, the propeller and ship hull models used in this thesis and their extension for simulation in heavy weather conditions are discussed.

4.1 Propeller Model

A propeller model was employed, in order to estimate the additional load that the engine has to overcome during load transients. A four quadrant propeller performance map was used, in order to be able to simulate the performance of the system during start-up and reversing. However, these cases are not investigated in the current work. The ship may be operating in four different conditions, which correspond to the four potential combinations of propeller rotational speed and advance speed. These combinations are also called quadrants of movement and are presented on Table 4.1. In the case of a fixed pitch propeller, the operation in four quadrants is based on the advance angle β at 70% of the propeller radius, defined as:

$$\beta = \arctan \frac{V_a}{0.7\pi N_p D_p} \tag{4.1}$$

Table 4.1: Definition of four quadrants of movement

Quadrant	Advance Speed	Rotational Speed	Advance Angle	Ship Movement
1st	Ahead	Ahead	$0 \leq \beta \leq \frac{\pi}{2}$	Ahead
2nd	Ahead	Astern	$\frac{\pi}{2} \leq \beta \leq \pi$	Crash-back
3rd	Astern	Astern	$\pi \leq \beta \leq \frac{3\pi}{4}$	Backing
4th	Astern	Ahead	$\frac{3\pi}{4} \leq \beta \leq 2\pi$	Crash-ahead

Where N_p is the propeller rotational speed, D_p is the propeller diameter and V_a is the mean effective wake velocity defined as:

$$V_a = V_s(1 - w) \tag{4.2}$$

where w is the effective wake fraction, which was calculated using a relation proposed by Schneekluth for cargo ships with stern bulb (70).

$$w = 0.5C_P\left(\frac{1.6}{1 + \frac{D_P}{T_S}}\right)\left(\frac{16}{10 + \frac{L}{B}}\right) \tag{4.3}$$

The propeller torque and thrust can be calculated as below:

$$Q_p = \frac{1}{2}C_Q\rho_{sw}V_r^2 A_0 D_p \tag{4.4}$$

$$T_p = \frac{1}{2}C_T\rho_{sw}V_r^2 A_0 \tag{4.5}$$

Where C_Q and C_T are the propeller torque and thrust coefficients, ρ_{sw} is the seawater density, A_0 is the propeller disk area and V_r is the relative advance velocity defined as

$$V_r = \sqrt{V_a^2 + (0.7\pi N_p D_p)^2} \tag{4.6}$$

The correlation between the β, C_T, C_Q nomenclature and the traditional J, K_T, K_Q used with open water propeller data is given below (71).

$$J = \frac{V_a}{N_P D_P} = 0.7\pi \tan\left(\frac{\beta}{180/\pi}\right) \tag{4.7}$$

$$K_T = \frac{T_P}{\rho_{sw}N_P^2 D_P^4} = C_T\frac{\pi}{8}(J^2 + (0.7\pi)^2) \tag{4.8}$$

$$K_Q = \frac{Q_P}{\rho_{sw}N_P^2 D_P^5} = C_Q\frac{\pi}{8}(J^2 + (0.7\pi)^2) \tag{4.9}$$

The thrust and torque coefficients from the Wageningen-B screw propeller series were used. Experimentally obtained thrust and torque coefficients for this propeller series as a function of the advance angle β can be found in (72; 73). In this work, C_Q and C_T were modelled as periodic functions of the advance angle β, using a Fourier series representation as shown below:

$$C_Q = -\frac{1}{1000} \sum_{\lambda=1}^{m} (A_{Q\lambda} \cos(\lambda\beta) + B_{Q\lambda} \sin(\lambda\beta)) \tag{4.10}$$

$$C_T = \frac{1}{100} \sum_{\lambda=1}^{m} (A_{T\lambda} \cos(\lambda\beta) + B_{T\lambda} \sin(\lambda\beta)) \tag{4.11}$$

The coefficients for the Fourier series were obtained from (71). The variation of thrust and torque coefficients for a Wageningen B5-65 is shown in Figure 4-1 as a function of the advance angle β. The C_T and C_Q coefficients were calculated from steady state open water test data. However, they were used for thrust and torque calculation in transient simulations in a quasi-steady sense, since the ship speed varies much slower than the propeller's rate of rotation.
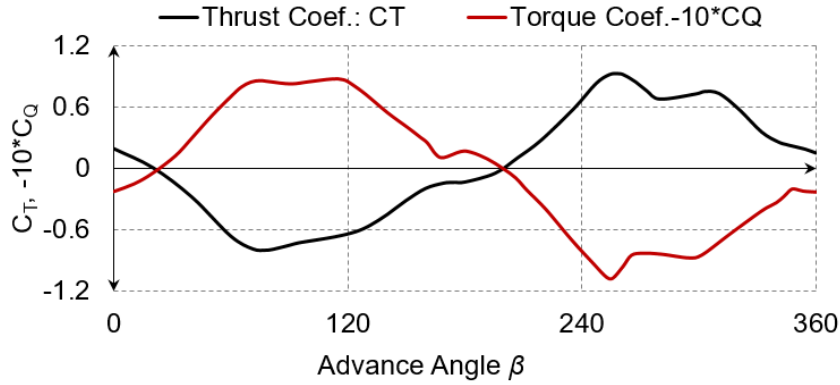
Figure 4-1: Experimentally obtained C_T and C_Q coefficients for the Wageningen B5-65 propeller

4.2 Ship Hull model

A one-dimensional dynamic model was employed for the calculation of vessel longitudinal acceleration and subsequently the vessel speed. The longitudinal acceleration of the ship $\dot{V_s}$ is:

$$\frac{dV_s}{dt} = \frac{T_p - \dfrac{R_T}{1 - t_D}}{m_s + m_{add}} \tag{4.12}$$

Where m_s is the mass of the ship which is equal to its displacement, m_{add} is the added mass for the surge motion, R_T is the calm water resistance, t_D is the thrust deduction factor and

T_p is the propeller thrust. The ship calm water resistance R_T was estimated using the Holtrop statistical method (74; 75). The added mass for the surge motion m_{add} was calculated using the linear equation proposed in (76). The thrust deduction factor was calculated using the relation proposed by Holtrop and Mennen (70).

$$t = 0.001979 \frac{L}{B(1 - C_P)} + 1.0585 \frac{B}{L} - 0.00524 - 0.1418 \frac{D_P^2}{BT_S} \tag{4.13}$$

4.3   Model extension for simulation in waves

The performance of the propulsion system was investigated in heavy weather conditions. For this reason, ship motions were calculated in both regular and irregular waves and the propeller and ship hull models were extended for simulation in waves. When the local wind conditions remain unchanged for a period of time (1/2 to 1 hour according to (70)) then the sea state can be characterized by a certain sea spectrum. In this work, the sea surface elevation is modelled using the JONSWAP wave spectrum which has the following spectral density function (77):

$$S(\omega) = 320 \cdot \frac{H_s^2 \omega^{-5}}{T_{peak}^4} \cdot \exp \frac{-1950 \omega^{-4}}{T_{peak}^4} \cdot \gamma_j^{a_j} \tag{4.14}$$

Where $\gamma_j = 3.3$ and a_j is defined as:

$$a_j = \exp - \left(\frac{\frac{\omega}{\omega_p} - 1}{\sigma \sqrt{2}} \right)^2 \tag{4.15}$$

where

$$\sigma = \begin{cases} 0.07 & , \omega < \omega_p \\ \\ 0.09 & , \omega \geq \omega_p \end{cases} \tag{4.16}$$

Different sea conditions are modelled by varying the sea spectrum parameters; the significant wave height H_s and the peak period T_{peak}. Formula (4.14) gives the wave energy spectrum for a fixed point in the ocean as a function of the wave circular frequency ω. A ship travelling with a non-zero speed of advance in a seaway, is excited in a different frequency than the wave circular frequency, which is called wave encounter frequency ω_e and is defined as:

$$\omega_e = \omega - kV_s \cos(X) \tag{4.17}$$

where X is the wave encounter angle. In order to simulate the performance of a ship sailing in a seaway, it is required to transform the spectrum to the reference of an observer on the moving ship. Transforming the spectrum to the moving frame of reference of the ship does not alter its energy and it follows that the area within the wave frequency range $\delta\omega$ must be exactly reproduced as an equal area within the corresponding encounter frequency range $\delta\ \omega_e$. Hence the following should hold (77):

$$S(\omega_e) = S(\omega)\frac{d\omega}{d\omega_e} = S(\omega)\frac{g}{g - 2\omega V_s cos(X)} \tag{4.18}$$

In head waves, the effect of spectral transformation is to increase the frequencies and reduce their spectral ordinate as shown in Figure 4-2. The two spectra have the same spectral area since the wave energy and the significant wave height remain unchanged by the transformation.
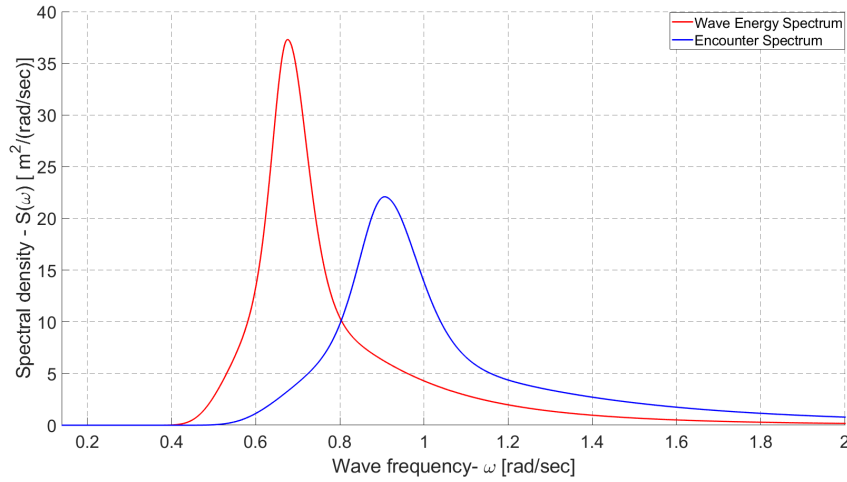
Figure 4-2: Wave energy spectrum and encounter spectrum

4.3.1   Modelling of Ship Motions in Regular waves

Regular monochromatic waves are characterized by a single frequency (wavelength) and amplitude (wave height/2), hence the sea surface elevation in the case of regular waves is:

$$\zeta(t, x) = A_{reg} \cdot \sin(\omega t + kx) \tag{4.19}$$

Where ω is the wave circular frequency, k is the wave number and x the coordinate of any free surface point calculated using a ship-fixed coordinate system. Ship motions are calculated assuming the ship as a linear dynamic system. Hence, the ship's response in regular waves is also

regular with the same frequency, a different amplitude and a phase lag. In order to determine the amplitude of the response, the Response Amplitude Operator (RAO) of every motion is needed. The RAOs and phase lag are dependent on the wave excitation frequency ω, the ship speed V_s, the wave encounter angle X and are defined as:

$$RAO = \frac{Response\ amplitude}{Excitation\ amplitude} \qquad (4.20)$$

The ship response at a regular wave with amplitude A_{reg} and phase ϕ at translational and rotational motions is given by Equations (4.21) and (4.22).

$$\xi_i = A_{reg}RAO_i(\omega_e, V_s, X) \cdot \sin(\omega_e t + \phi + \delta\phi_i(\omega_e, V_s, X)) \qquad [m]$$
$$i = 1, 2, 3$$
$$(4.21)$$

$$\xi_j = kA_{reg}RAO_j(\omega_e, V_s, X) \cdot \sin(\omega_e t + \phi + \delta\phi_j(\omega_e, V_s, X)) \qquad [rad]$$
$$j = 4, 5, 6$$
$$(4.22)$$

The calculation of the hydrodynamic response characteristics of the vessel was carried out using the 6DOF, 3D panel code NEWDRIFT (78; 79; 80). The discretized hull geometry is required as input to the software. A 3D representation of the examined hull form with and without the panels is shown in Figures 4-3 and 4-4.
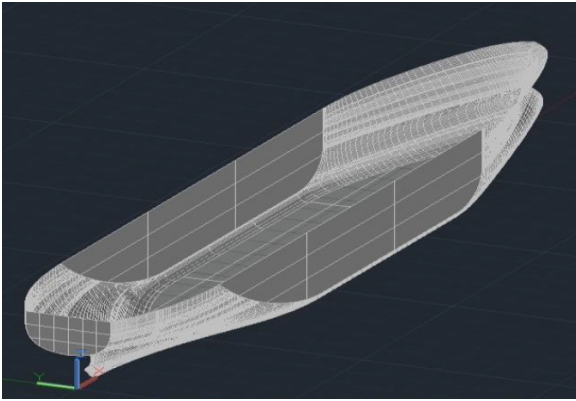
Figure 4-3: 3D representation of the examined hull form
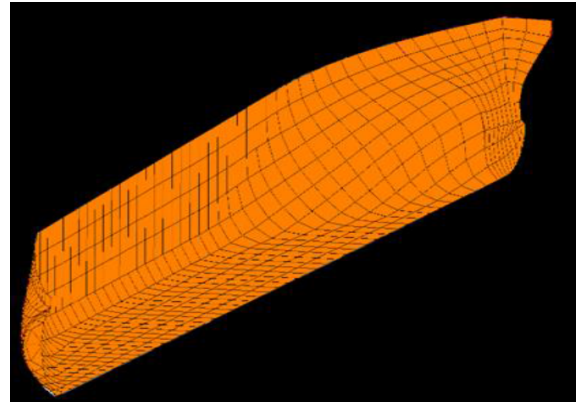
Figure 4-4: 3D representation of the examined hull form, discretized with panels

Hydrodynamic response results were generated using the NEWDRIFT software for regular waves with circular frequency from 0.45 to 2.5 rad/s and for vessel speeds from 6 to 16 knots. For the vessel under consideration these circular frequencies correspond to waves with a λ/L ratio from 1.9 to 0.06. In all cases the wave encounter angle was 180 ^{o} (head waves) since this case

is the most challenging condition for the propulsion system in terms of wave added resistance, according to (51). For each combination of wave frequency and vessel speed the following were calculated using the 3D panel code:

1. The response amplitude operators (RAOs) of each motion.
2. The phase difference, $\delta\phi$ between excitation and response of each motion.
3. The added mass in the surge motion, m_{add}.
4. The wave added resistance in regular waves, R_{reg}.

The calculated values of RAOs, $\delta\phi, m_{add}$ and R_{reg} were then interpolated using polynomial surfaces in order to get analytical expressions for each quantity. An example of the resulting RAO surface for the heave and pitch motion, for different ship speeds and wave encounter frequencies in head waves is shown in Figures 4-5 and 4-6.
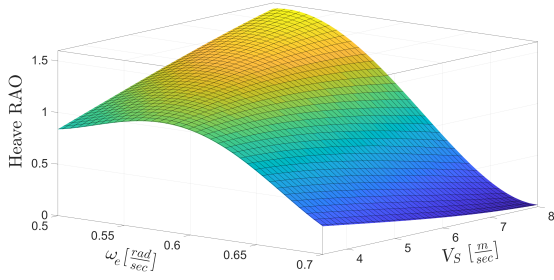
Figure 4-5: RAO of heave motion for different ship speeds and wave encounter frequencies
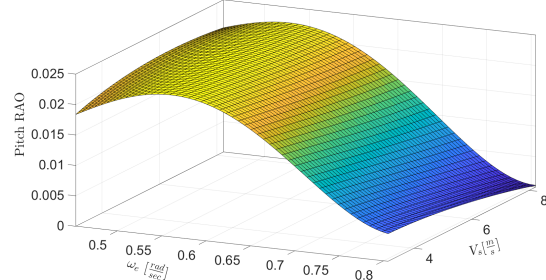
Figure 4-6: RAO of pitch motion for different ship speeds and wave encounter frequencies

4.3.2   Modelling of Ship Motions in Irregular waves

Irregular waves can be treated as a superposition of regular waves with different frequencies and the same amplitude. The different wave components were obtained by dividing the spectral area in n number of regions having the same area, thus the same amplitude (77). The frequency of each wave component is defined as the frequency at the centroid of each region. Figure 4-7 shows an example of the transformed spectrum division in 10 regions. Region boundaries are shown with dotted lines and the obtained frequencies are shown with red crosses. At each discrete frequency the amplitude of the nth wave component is given by:

$$A_{reg} = A_{reg_i} = \sqrt{2S(\omega_{e,i})\delta\omega_{e,i}}, \quad i = 1, ..., n \tag{4.23}$$

The different wave components have the same amplitude $_{reg}$, since the different regions have the same area. In this study the number of different wave components n, was selected to be 500.
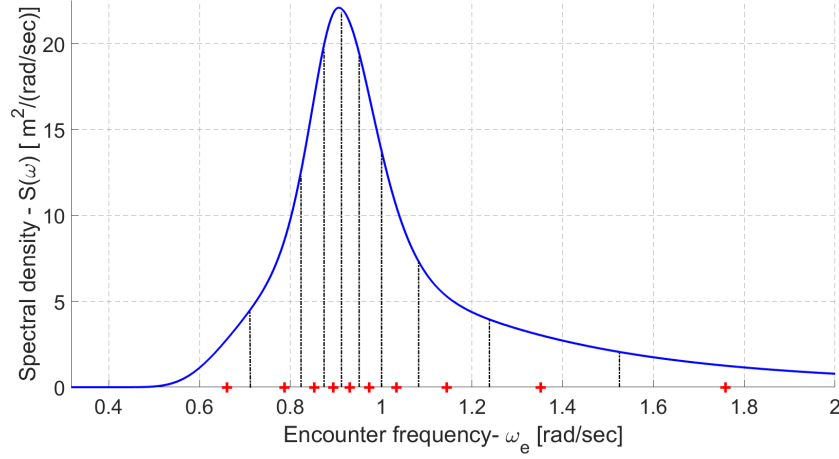
Figure 4-7: Example of division of the encounter spectrum in 10 regions

The resultant wave elevation is hence given by:

$$\zeta(t,x) = A_{reg} \sum_{i=1}^{500} \cdot \sin(\omega_i t + k_i x + \phi_i) \tag{4.24}$$

The phase of each regular wave ϕ_i is obtained using a random number generator. Ship motions at six degrees of freedom were calculated assuming the ship as a linear dynamic system. Hence the response of the ship can be calculated as the superposition of the responses obtained for each excitation wave component, under the assumption of linearity of the system. Thus, the motions of the ship sailing in irregular waves, $\xi_{\kappa_{irr}}$ can be calculated as:

$$\xi_{\kappa_{irr}} = \sum_{i=1}^{500} \xi_{\kappa_{reg,i}} \tag{4.25}$$

where κ is the index of the 6 degrees of freedom of the ship and $\xi_{\kappa_{reg,i}}$ is defined as:

$$\xi_{\kappa_{reg,i}} = A_{\kappa,i} \cdot \sin(\omega_{e,i} + \phi_{k,i} + \phi_i)$$
$$\kappa = 1,...,6 \ \ and \ \ i = 1,...,500 \tag{4.26}$$

where the motion amplitude $A_{\kappa,i}$ and phase difference $\phi_{k,i}$ in each regular wave is calculated using the NEWDRIFT software as discussed in Section 4.3.1.

4.3.3   Ship Hull Model Extension

The one dimensional dynamic ship hull model presented in Section 4.2 is extended for simulation in waves, to include the effect of wave added resistance R_{AW}. In the case of simulation in waves

the vessel dynamics in the longitudinal direction are described by :

$$\frac{dV_s}{dt} = \frac{T_p - \left(\frac{R_T}{1 - t_D} + R_{AW} + F_{fk}\right)}{m_s + m_{add}}$$

(4.27)

where F_{fk} are the Froude Krylov forces, which are forces due to the incident waves. Since these forces are zero-mean oscillatory forces (81), and we are interested in the mean vessel speed and not in minor speed fluctuations, F_{fk} are neglected in the present analysis. In this case, the added mass for the surge motion m_{add}, was obtained using the NEWDRIFT code. In the case of regular waves, it is determined based on the combination of different wave characteristics (T, h). In the case of irregular waves, the added mass is assumed to be equal to the value obtained for a representative regular wave for the examined sea spectrum (See Section 6.2). Due to the lack of data concerning the variation of thrust deduction factor in waves it was assumed to be constant. The added resistance in regular waves R_{reg} was calculated using the 3D panel code. The added resistance in irregular waves was then computed for different ship speeds and sea conditions as:

$$R_{AW}(V_s) = 2 \int_0^\infty \frac{R_{reg}(\omega; V_S)}{A_{reg}^2} \cdot S(\omega)d(\omega)$$

(4.28)

4.3.4 Propeller Model Extension

When a ship sails in a seaway with adverse weather conditions, intense pitch and heave motions may cause the propeller to approach and even pierce the free surface. This results in a reduction of propeller produced thrust and demanded torque (55). In order to take into account this phenomenon, the b factor proposed by Minsaas et al in (82), is employed in the thrust and torque calculation equations as shown below:

$$Q_p = \frac{1}{2}C_Q\rho_{sw}V_r^2 A_0 D_p b^{0.8}$$

(4.29)

$$T_p = \frac{1}{2}C_T\rho_{sw}V_r^2 A_0 b$$

(4.30)

Where b is a factor calculated using an empirical correlation, which takes into account the reduction of propeller produced thrust and torque, due to the propeller emergence to the free surface. The effects of the b factor were considered in a quasi-steady manner, since the propeller depth varies much slower than its rate of rotation. The b factor is calculated using an empirical

correlation as follows:

$$
b = \begin{cases} 1 - 0.675 \cdot \left[1 - 0.769\left(\frac{h_v}{r_p}\right) \right] & , \frac{h_v}{r_p} < 1.3 \\[4mm] 1 & , \frac{h_v}{r_p} \geq 1.3 \end{cases} \tag{4.31}
$$

Where h_v is the time varying vertical distance between the propeller shaft centre and the free surface and r_p is the propeller radius. The time varying distance h_v is calculated at the location of the propeller $x_p = x - L/2$ and is defined as:

$$
h_v(t) = \zeta_p(t) + h_{heave}(t) + h_{pitch}(t) + z_p \tag{4.32}
$$

where ζ_p is the free surface elevation at the location of the propeller and h_{heave} is the propeller's vertical displacement due to heave motions, calculated as:

$$
h_{heave}(t) = \begin{cases} \xi_3 = A_3 \cdot \sin(\omega_e t + \phi_3 + \phi) & , for\ regular\ waves \\[4mm] \xi_{3,irr} = \sum_{i=1}^{500} A_{3,i} \cdot \sin(\omega_{e,i} t + \phi_{3,i} + \phi_i) & , for\ irregular\ waves \end{cases} \tag{4.33}
$$

and h_{pitch} is the propeller vertical displacement due to pitch motion, which can be obtained using the following expression. As equation (4.34) denotes, it is assumed that the rotation of the ship takes place around the ship's centre of gravity.

$$
h_{pitch}(t) = \begin{cases} x_p \tan\left(A_5 \sin(\omega_e t + \phi_5 + \phi) \right) & , for\ regular\ waves \\[4mm] \sum_{i=1}^{500} x_p \tan\left(A_{5,i} \sin(\omega_{e,i} t + \phi_{5,i} + \phi_i) \right) & , for\ irregular\ waves \end{cases} \tag{4.34}
$$

4.3.4.1 Propeller inflow velocity calculation in waves

The propeller effective inflow velocity significantly affects the propeller thrust and torque as Equations (4.29) and (4.30) denote. The variation of V_a in regular waves due to the surge motion of the ship and the orbital motion of water particles, was calculated using the expression proposed by Ueno in (51) for X=180 ^{o}. In this work it is mentioned that the variation of the propeller inflow velocity due to the heave and pitch motions of the ship can be neglected. The

expression is shown in eq. (4.35) where the first term, includes the effect of the surge motion of the vessel and the second term includes the effect of the orbital motion of the sea particles on propeller inflow velocity.

$$V_a(t) = (1 - w)[V_s - \omega_e A_1 \cdot \sin(\omega_e t - \phi_1)] - \alpha \omega A_{reg} e^{-kz_p} \cdot \cos(\omega_e t + kx_p) \tag{4.35}$$

Where t is time, A_1 and ϕ_1 are the amplitude and phase lag of the surge motion respectively,, k is the wave number, z_p is the immersion depth of the propeller shaft, x_p is the position of the propeller with reference to the centre of gravity of the vessel and α is a coefficient accounting for the wave amplitude decrease at the stern defined as:

$$\alpha = \begin{cases} 0.2\left(\frac{\lambda}{L}\right) & , \frac{\lambda}{L} \le 2.5 \\ \\ 1 & , \frac{\lambda}{L} > 2.5 \end{cases} \tag{4.36}$$

In the case of irregular waves, eq. (4.35) is modified utilizing the assumption of linearity of the system.

$$\begin{aligned} V_a(t) = &(1 - w)\left[V_s - \sum_{i=1}^{500} \omega_{e,i} A_{1,i} \cdot \sin(\omega_{e,i} t - \phi_{1,i})\right] - \\ &\sum_{i=1}^{500} \left[\alpha_i \omega_i A_{reg,i} e^{-kz_p} \cdot (\omega_{e,i} t + k_i x_p + \phi_i)\right] \end{aligned} \tag{4.37}$$

Note: In eq. (4.27) the Froude-Krylov forces are neglected, since we are interested in the calculation of the mean vessel speed. In eq. (4.35) though, the surge amplitude calculated by the panel code is used, where the Froude-Krylov are taken into account. In this case no averaging takes place, since V_a significantly affects the propeller demanded torque and hence we are interested in calculating the instantaneous propeller inflow velocity V_a.

4.3.4.2   Validation of the b factor using open water data in various propeller drafts

In this section, the reliability of the b factor introduced in Eqs. (4.29) and (4.30), is evaluated using available open water test data (83). This empirical factor, reduces the propeller thrust and torque, due to propeller proximity to the free surface. Open water diagram of a propeller

operating in calm sea conditions and three different immersion drafts were available and are presented in Figure 4-8. The examined propeller immersion drafts h_v/D_p are 1.13, 0.5 and 0.34. At $h_v/D_p = 1.13$ propeller operation is unaffected by the free surface, at $h_v/D_p = 0.5$ propeller blades barely touch the free surface and at $h_v/D_p = 0.34$ propeller blades pierce the surface. The main particulars of the propeller used in open water tests are shown in Table 4.2. It is observed, that the influence of propeller immersion is increasing with increasing
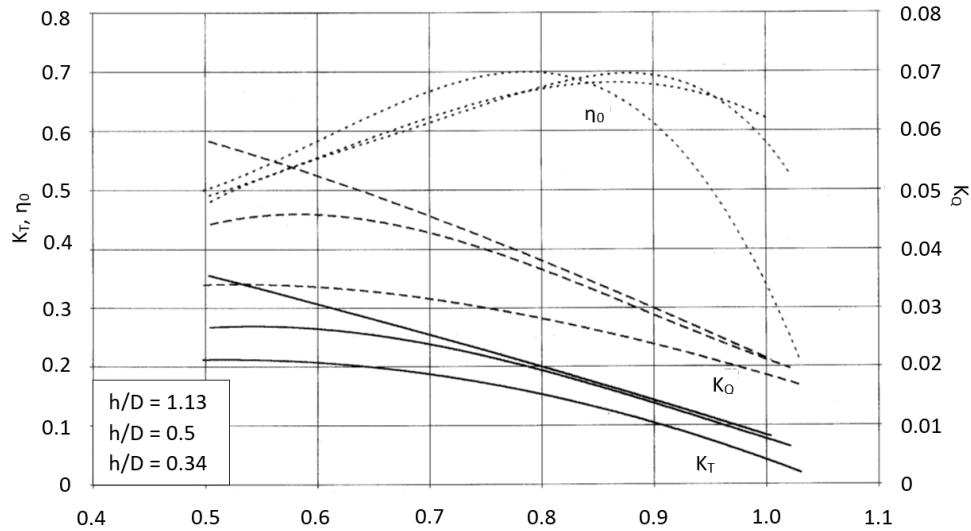
Figure 4-8: Open water diagram of the propeller used in model tests for various immersion depths. K_T: solid lines, K_Q: dashed lines, η_0: dotted lines (83)

Table 4.2: Particulars of the propeller used in model tests

	Propeller Type	Fixed Pitch Propeller
Diameter	272.7	mm
No of Blades	6	-
Pitch Ratio	1.05	-
A_E/A_0	0.7	-

propeller loading (decreasing J). Whereas at h_v/D_p=0.5 (blade tips just touch the surface) the influence is limited to a range of J<0.8, propeller characteristics change dramatically when the blades pierce the surface (h_v/D_p=0.34). It is interesting that even at h_v/D_p=0.34 the maximum efficiency is almost unchanged, whereas the optimum advance coefficient becomes considerably lower. In order to evaluate the accuracy of the b factor, the reduction of the measured thrust and torque coefficients is compared to the one predicted by eq. 4.31. Table 4.3 contains K_T and K_Q measurements for various propeller immersion depths and advance coefficients J, as they were derived from Figure 4-8.

Table 4.3: Thrust and torque coefficients for varying advance coefficients and propeller immersion

	h_v/D_P	J=0.5	J=0.6	J=0.7	J=0.8	J=0.9
	1.13	0.355	0.306	0.253	0.199	0.142
K_T	0.5	0.267	0.262	0.237	0.191	0.137
	0.34	0.212	0.207	0.186	0.152	0.103
	1.13	0.584	0.523	0.457	0.280	0.238
$10 \cdot K_Q$	0.5	0.437	0.457	0.426	0.364	0.286
	0.34	0.339	0.335	0.315	0.380	0.299

Using these measurements, the equivalent b-factor can be calculated for each one of the above cases as:

$$b_T = \frac{K_T(J)}{K_{T,\frac{h}{D_P}=1.13}(J)} \tag{4.38}$$

$$b_Q = \frac{K_Q(J)}{K_{Q,\frac{h}{D_P}=1.13}(J)} \tag{4.39}$$

The calculated b factor for each case is shown in Table 4.4. As expected, b is decreasing with decreasing J (increasing propeller loading).

Table 4.4: Calculated b factor using open water measurements

	h_v/D_P	J=0.5	J=0.6	J=0.7	J=0.8	J=0.9	Average
	1.13	1.0	1.0	1.0	1.0	1.0	1.0
b_T	0.5	0.753	0.858	0.935	0.958	0.962	0.893
	0.34	0.596	0.676	0.733	0.763	0.726	0.699
	1.13	1.0	1.0	1.0	1.0	1.0	1.0
b_Q	0.5	0.696	0.845	0.916	0.948	0.946	0.870
	0.34	0.507	0.573	0.628	0.683	0.752	0.628

Then, the averaged b-factor for the various advance coefficients is compared with the one calculated using eq. (4.31) and the results are summarized in Table 4.5. Results show that torque reduction due to propeller proximity to the free surface can be predicted with adequate accuracy using eq. (4.31), since deviation from measured values is less than 3%. Deviation between measured and calculated thrust reduction lies around 5%.

Table 4.5: Deviation between average b-factor derived from measurements and the one calculated using eq. 4.31

	h_v/D_P	Average b	Calculated b	Deviation
	1.13	1.0	1.0	0%
b_T	0.5	0.893	0.844	5.5%
	0.34	0.699	0.645	7.7%
	1.13	1.0	1.0	1.0
b_Q	0.5	0.87	0.844	2.99%
	0.34	0.628	0.645	-2.71%

4.3.4.3   Validation of the b factor and propeller inflow velocity V_a using dynamic open water data in regular waves

In the previous section, the reliability of the b factor was evaluated using open water thrust and torque measurements in calm water conditions and different propeller immersion depths. In this section, the b factor as well as the expression for the propeller effective inflow velocity V_a (see eq.(4.35)), are validated in dynamic open water conditions. Timeseries of thrust and torque measurements were available for a propeller operating in open water conditions, in regular head waves with a wave height of 0.22 m and various wavelengths (83). The distance of the propeller shaft centre from the undisturbed free surface was 0.2 m. Propeller rotational speed was set at 11.25 RPS and forward carriage speed V_c was 2.35 m/sec. The basic particulars of the propeller used at model tests are presented in Table 4.2 and open water propeller characteristics are presented in Figure 4-8. Since the propeller is operating in open water conditions eq. (4.35) is transformed to:

$$V_a(t) = V_c - \omega A_{reg} e^{-k z_p} \sin(\omega_e t + \phi) \tag{4.40}$$

And the propeller thrust and torque are calculated as below, using the K_T and K_Q for $h_v/D_p = 1.13$ in Figure 4-8.

$$T_P(t) = K_T(t) \rho_{fw} N_p^2 D_p^4 \tag{4.41}$$

$$Q_P(t) = K_Q(t) \rho_{fw} N_p^2 D_p^5 \tag{4.42}$$

Thrust and torque predictions are compared to measurements for 3 different wavelengths and two different propeller immersion depths in Figures 4-9 and 4-10. The three examined wavelengths are 4.15 m, 8.3 m and 12.45 m. The sea surface elevation for the first wavelength is also presented. Measurements are shown with black colour and model predictions are shown with red colour. For $h_v = 0.31$ ($h_v/D_p = 1.13$), no torque or thrust loss due to proximity to the free surface
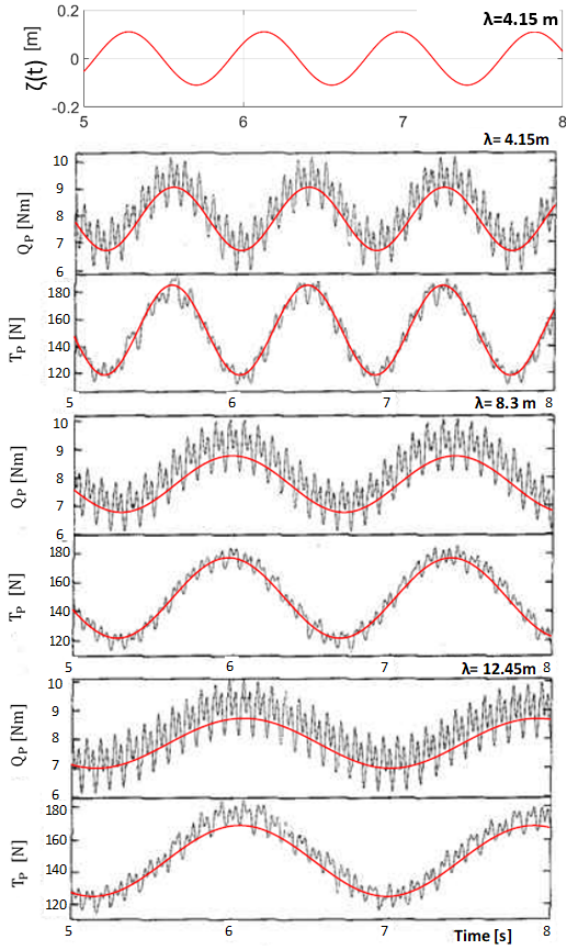
Figure 4-9: Model predicted (red) T_p and Q_p against measurements (black) for 3 different wavelengths (h_v=0.31 m, $h_v/D_p = 1.13$) (83)
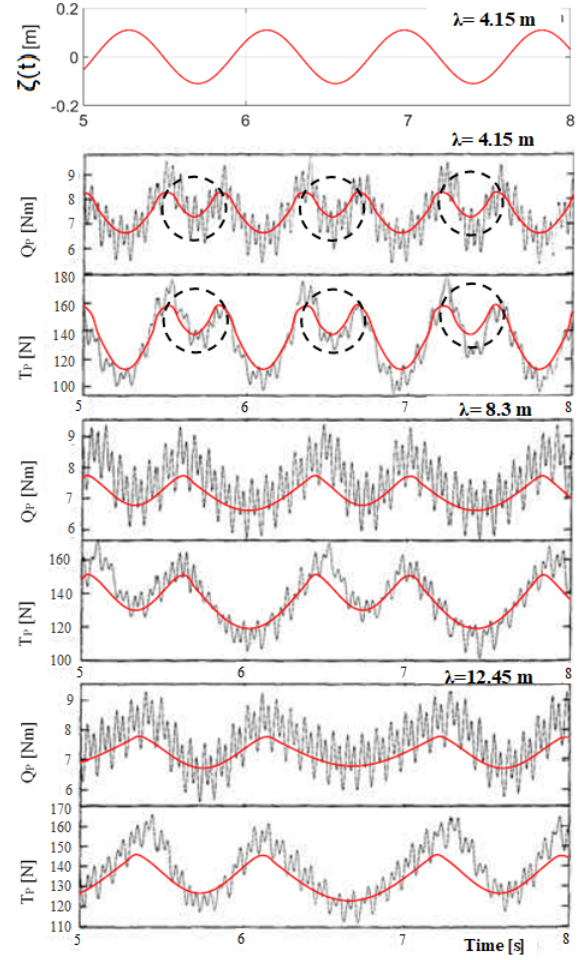
Figure 4-10: Model predicted (red) T_p and Q_p against measurements (black) for 3 different wavelengths (h_v=0.2 m, $h_v/D_p = 0.72$) (83)

is detected. Thrust and torque in waves vary with the encounter frequency, which is rather low relative to the rotational speed of the propeller. Thrust and torque predictions are close to measured values for the examined wavelengths. For the second case $h_v = 0.2$ ($h_v/D_p = 0.72$), it is shown that propeller operation near the free surface has a significant effect on propeller thrust and torque. At time instants 5.5 s, 6.5 s and 7.5 s there is a thrust and torque loss due to the propeller proximity to the free surface (see dashed circles at Figure 4-10). This is present in all three wavelengths but is more visible in the shortest wavelength, λ=4.15 m. It is also observed that the trough in T_p and Q_p corresponds with the trough of surface elevation. In both cases, model predictions are very close to measurements, which is an indication that eq. (4.35) accurately predicts the propeller inflow velocity V_a, since K_T and K_Q values were known. Hence, it can be concluded that in cases without propeller emergence the behaviour can be described satisfactorily with a quasi-steady method, in the simplest case using the common K_T

and K_Q curves derived from open-water tests in calm water. In cases with propeller emergence or proximity to the free surface, the thrust and torque decrease can be predicted with satisfactory accuracy using empirical correlations such as the one presented in eq. (4.31). The high frequency thrust and torque variations which can be observed in Figures 4-9 and 4-10 cannot be predicted by the employed model which is based on the propeller open water tests. However, these fluctuations do not affect engine operation due to their small amplitude and very high frequency and can therefore be neglected . In order to predict these high frequency variations more detailed methods should be employed as in (84).

Chapter 5

Coupled Model Validation

The various submodels that were presented in the previous chapters, were integrated into one coupled model in order to simulate the transient response of the entire marine propulsion power-plant. The interconnection and data exchange between the different submodels is shown in Fig. 5-1. The engine model communicates with the SCR model, providing the exhaust gas temperature at the SCR inlet and accepting the exhaust gas temperature at the reactor outlet. It also communicates with the propeller model, supplying the engine rotational speed and receiving the propeller demanded torque (engine load). The propeller model also communicates with the vessel model, providing the propeller produced thrust and receiving the ship forward speed. In this chapter, the coupled model is validated under transient loading conditions by comparing model predictions to ship-board measured data acquired from a commercial vessel. The main particulars of the ship, propeller and SCR reactor are listed in Table 5.1 and the ones of the engine are listed in Table 2.1. The inputs to the model were the governor speed setpoint and the temperature setpoint for the CBV controller. Moreover, since the control scheme of RBV, RSV and RTV valves was not available, measured timeseries of the position of these valves were used as input to the model. Model validation focused on low load operation, which is the most challenging operating area for the model since auxiliary blowers are running and the turbochargers are running outside their mapped area. More specifically, the cases that were examined are:

  (i) Deceleration from high to medium load

 (ii) Acceleration from low to medium load and engagement of SCR system

(iii) SCR system heating at high engine load

 (iv) Engine deceleration from medium to low load

  (v) Engine acceleration from low to medium load
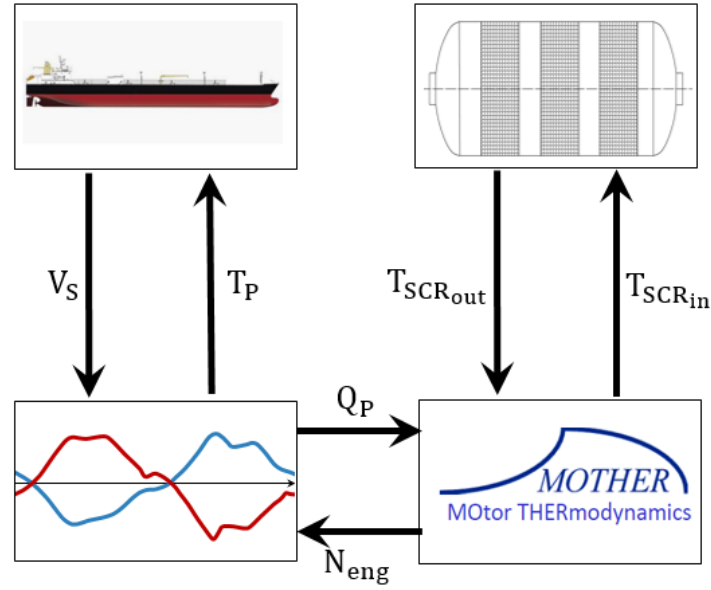
Figure 5-1: Interconnection and data exchange between the different submodels

Table 5.1: Characteristics of the simulated system

Ship Particulars		
Length	159.9	m
Breadth	25.6	m
Design Draught	9.5	m
Cargo Capacity	20600	m^3
DWT	18200	t
Design Speed	16	kn
Fixed Pitch Propeller Particulars		
Diameter	5.85	m
No. of blades	5	-
Pitch ratio	0.8	-
Blade Area Ratio	0.65	-
Total Inertia	37200	kgm^2
SCR Reactor Particulars		
Length	6.0	m
Diameter	2.54	m
Catalyst volume	8.02	m^3
Catalyst mass	3500	kg
Catalyst specific area	698	m^2/m^3

5.1   Deceleration from high to medium load

In the first validation case, a deceleration from high to medium engine load at Tier III operating mode is examined. Valve RBV is fully closed and valves RTV and RSV are fully open (see Figure 1-2 for SCR valve configuration), i.e. all the exhaust gas passes through the SCR system. The engine operates at constant 80% load until 270 s and then decelerates to 55% load at

about 500 s. Simulation results are shown in Figures 5-2 and 5-3 where model predictions are shown with blue colour and measurements are shown with red colour. When the deceleration commences, valve CBV opens so that exhaust gas temperature at the SCR reactor inlet will remain above the ABS formation limit. When CBV opens, a fraction of scavenge air is directed from the scavenge receiver directly to the turbine, bypassing engine cylinders. In this way, the amount of air entering the engine decreases resulting in richer combustion and hence in an increase of exhaust gas temperature at the SCR reactor inlet. Model predictions show good agreement with measured signals of engine speed and engine load. PID controller predictions for the governor index and CBV position are also very close to measured data. The measured T/C speed was not available, hence the validation of the turbocharger operation may only be conducted through prediction of boost pressure which is predicted with satisfactory accuracy. The predicted exhaust gas temperature at the SCR reactor outlet decreases slightly faster than the measured one. However, deviation between simulated and measured values remains small
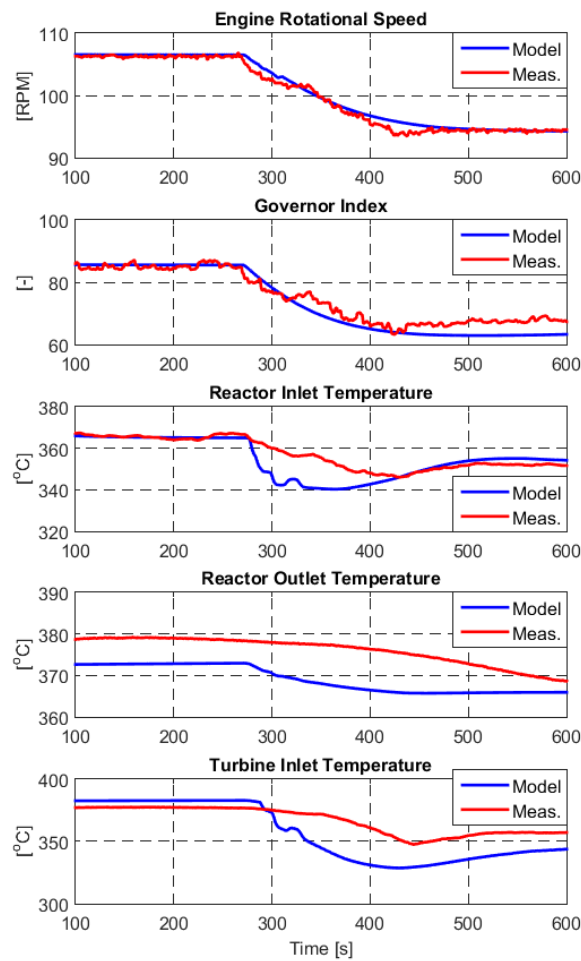

Figure 5-2: Model predictions against on-board measurements for load decrease scenario from high to medium engine load
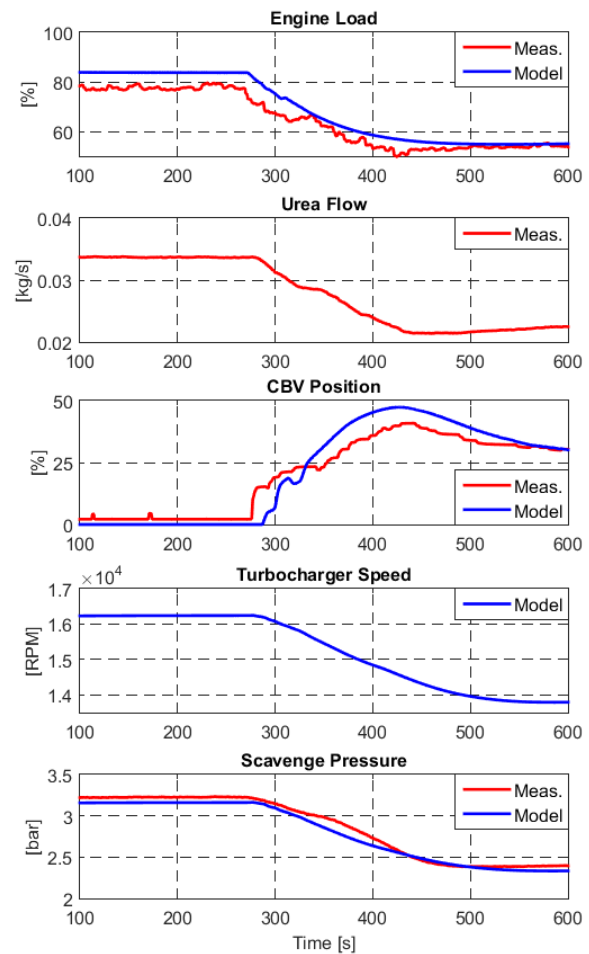
Figure 5-3: Simulation results against on-board measurements for a high to medium load deceleration

(less than 10 ^0C) throughout the simulated time. Due to the large size and thermal inertia of the SCR reactor, exhaust gas temperature at the reactor outlet decreases much slower that the one at the reactor inlet. On the other hand, exhaust gas temperature at the turbine inlet decreases more rapidly due to the mixing of exhaust gas with scavenge air, as a result of valve CBV operation.

5.2   Acceleration from low to medium load and engagement of SCR system

In the second validation case, a low load acceleration followed by an engagement of the SCR system is investigated. Initially, the engine operates at 18% load in Tier II mode, i.e. valve RBV is fully open and the SCR system is isolated. At about 1830 s the engine accelerates to 30% load and at about 1900 s the engagement of the SCR system commences. Valve RTV opens gradually, valve RSV opens entirely and valve RBV remains fully open in order to supply the turbine with adequate enthalpy. After the acceleration, the engine operates at steady load for about 1000 s, then further accelerates to 50% and then to 90% load and eventually decelerates to 50% load. At 2150 s, valve RTV's opening increases to about 60%, which results in a reduction of turbocharger speed, since the exhaust gases that pass through the SCR arrive to the turbine with reduced enthalpy. The drop of turbocharger speed results in a slight decrease of p_{scav}, p_{comp} and p_{max} (dotted circle in Figure 5-5). At 3400 s, when the deceleration from 90% to 50% load takes place, RTV position is reduced almost by half. In this way, less amount of exhaust gas passes through the SCR system and more exhaust gas proceeds directly to the turbine. This is done, to ensure that the turbocharger will be provided with adequate enthalpy and avoid any possible engine-turbocharger system instability or engine component overheating. It should be noted that the auxiliary blowers operate during the whole time, even though at times p_{scav} is well above the blower deactivation pressure, in order provide the turbine with enough enthalpy and avoid instability of the engine-turbocharger system. Model predictions are compared to measured data in Figures 5-4 and 5-5. In this dataset, the p_{max} and p_{comp} measured signals were available and are also included in the results. Measured time-series of RBV, RSV and RTV position profile were used as input to the model. Prediction of engine speed is very good both during acceleration and deceleration. Engine load and governor index are also predicted with good accuracy. Compression and maximum combustion pressure prediction is also satisfactory. The

model slightly overestimates the exhaust gas temperature on the reactor inlet in the beginning of SCR heating but the agreement between model predicted values and measurements is very good after 2400 s. Moreover, there is very good agreement between the predicted and measured exhaust gas temperature at the reactor outlet. The increase of SCR reactor outlet temperature is much slower than the one at the reactor inlet due to the large thermal inertia of the SCR reactor. After half an hour (1800 s) of SCR heating with the RTV valve being 50% open, the exhaust gas temperature at the reactor outlet increased only by 40 ^oC.
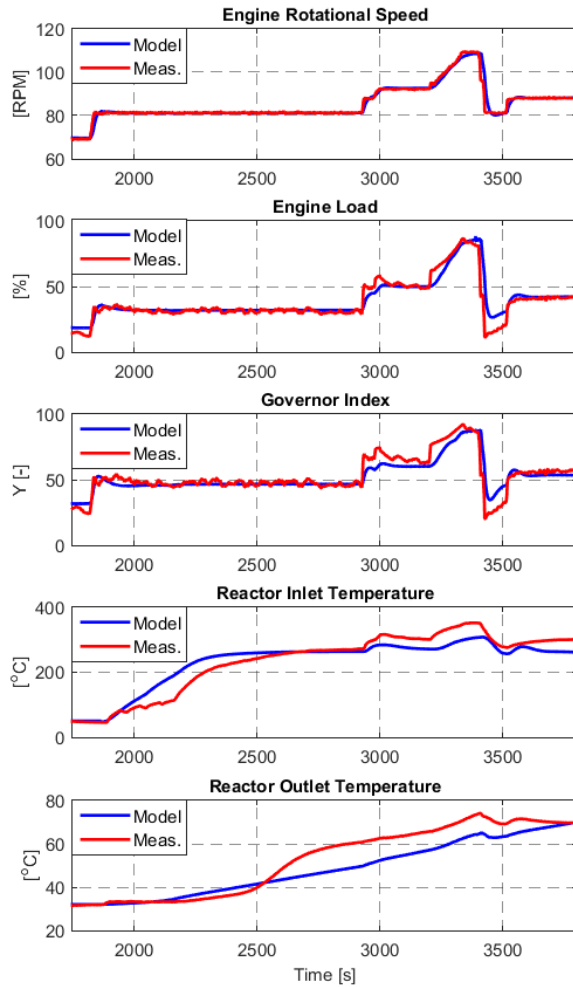
Figure 5-4: Model predictions and on-board measurements during low load transients and engagement of the SCR system
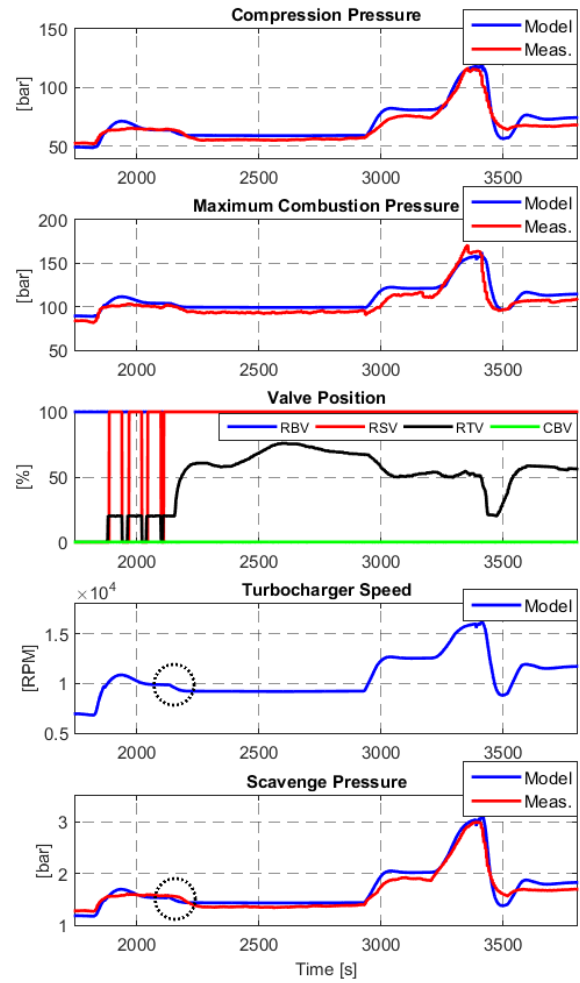
Figure 5-5: Simulation results and on-board measurements during low load transients and engagement of the SCR system

5.3   SCR system heating at high engine load

In this case, the engine initially operates at steady 70% engine load at Tier II mode and at 150 s the engagement of the SCR system commences. Engine rotational speed and engine load

remain constant during the whole simulation time. The auxiliary blowers are not engaged in
this case, since the engine is operating at sufficiently high load. Measured time-series of RBV,
RSV and RTV position were used as input to the model. At the beginning of the simulation,
RBV is fully open and RTV opens gradually, up to about 50 % opening. Due to the bypassing of
exhaust gases through the SCR system, the enthalpy of exhaust gas reaching the turbocharger
turbine decreases. This leads to a decrease of turbocharger speed of around 2000 RPM and
a subsequent reduction of boost pressure of 0.7 bar. As the SCR reactor is heated, and the
enthalpy of exhaust gases exiting the reactor increases, $N_{T/C}$ and p_{scav} also increase. At 2500 s,
valve RTV opens fully and valve RBV starts closing, until 3800 s when it shuts completely. This
results in an increase of $N_{T/C}$ which consequently leads to an increase of p_{scav}, p_{comp} and p_{max}.
Valve CBV remains closed throughout the simulation time. The sudden opening of valve RTV,
and the sudden drop of boost pressure resulted in a slight fluctuation of model predicted engine
speed and load at 300 s. As in the previous case, in the beginning of SCR heating, the reactor

Figure 5-6: Model predictions and on-board
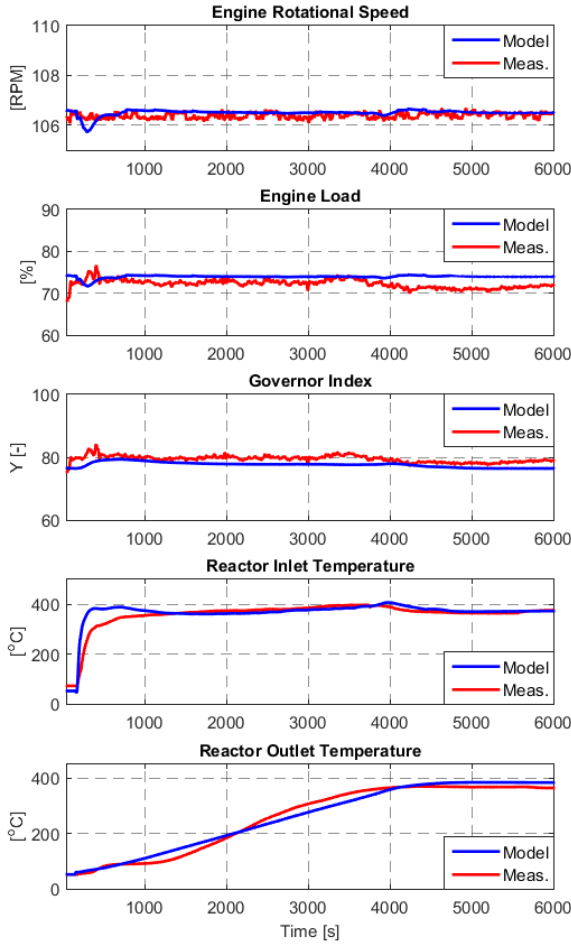measurements during the heating of the SCR
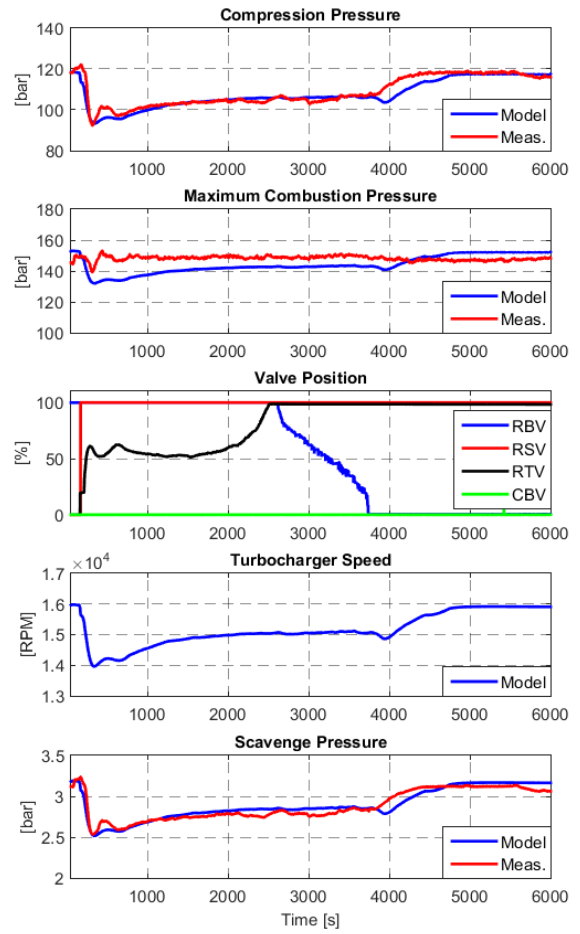system at constant 70% engine load

Figure 5-7: Simulation results and on-board
measurements during the heating of the SCR
system at constant 70% engine load

inlet temperature is slightly overestimated by the model. However, after 1000 s agreement between model predicted and measured reactor inlet temperature is very good. Prediction of scavenge pressure and exhaust gas temperature at the reactor outlet, is also satisfactory. In this simulation case, almost 3800 s (around 1 hour) were needed to heat the SCR reactor.

5.4   Engine deceleration from medium to low load

In this validation case, a deceleration from medium to low load is examined. At the beginning of the simulation, the engine operates at steady 55% load for 280 s and then decelerates to 27% load at about 700 s. The SCR system is engaged, which means that valve RBV is fully closed and valves RSV and RTV are fully open. Validation results are presented in Figures 5-8 and 5-9 where measurements are shown with red color and model predictions are shown with blue color. The measured turbocharger speed was not available hence only the simulated one is shown. At the beginning of the simulation, valve CBV is open at about 25% and when the deceleration commences opens further, in order to ensure proper exhaust gas temperature at the inlet of the SCR reactor. At about 440 s, during engine deceleration, scavenge pressure drops below the blower activation pressure of 2.05 bar and the auxiliary blowers begin operating in order to provide the engine with sufficient amount of air. The engagement of the auxiliary blowers creates a sudden increase of airflow to the engine. As a result, combustion becomes leaner and the exhaust gas temperature at the engine outlet drops. Consequently, valve CBV opens even more in order to maintain the reactor inlet temperature above the setpoint value. The operation of the A/B results in a slower decrease of turbocharger speed and scavenge pressure due to the increase of airflow to the turbocharger. It is worth noticing that the exhaust gas temperature at the reactor outlet decreases much slower than the one at the reactor inlet due to the large thermal inertia of the SCR reactor. On the other hand, the exhaust gas temperature at the turbine inlet decreases much more rapidly due to the action of valve CBV, which leads scavenge air to the turbine inlet. It is observed that the exhaust gas temperature at the reactor outlet changes very little during the load transient. Model predictions for engine speed and power are very close to measured values. Prediction of governor index Y and CBV position is also good both during the load transient as well as during steady engine operation. Moreover, SCR temperature prediction is satisfactory both in terms of values as well as dynamics. The simulated reactor outlet temperature decreases slightly faster than the measured one but the deviation between measured and simulated values remains small (less than 10 ^{o}C).
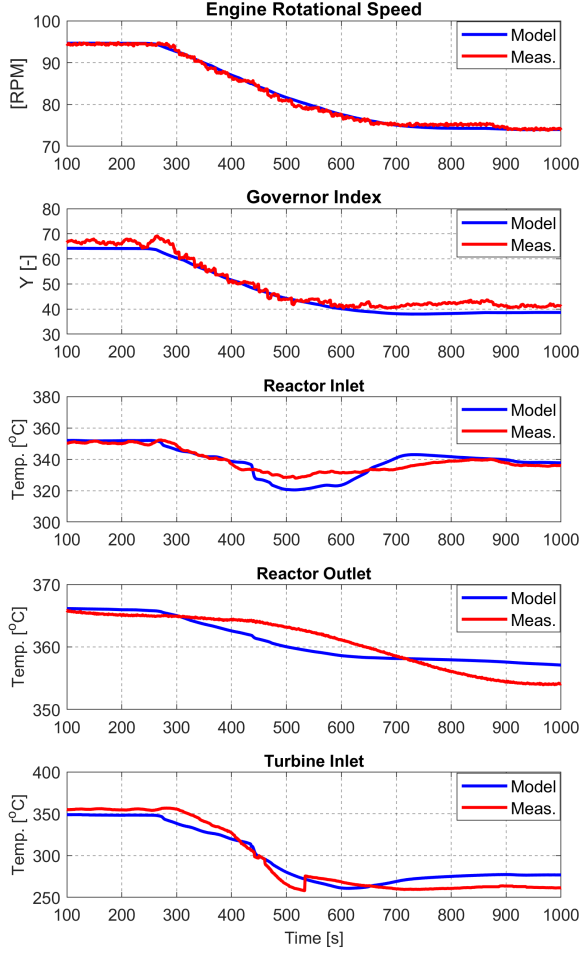
Figure 5-8: Model predictions against on-board measured data for load decrease scenario from medium to low engine load
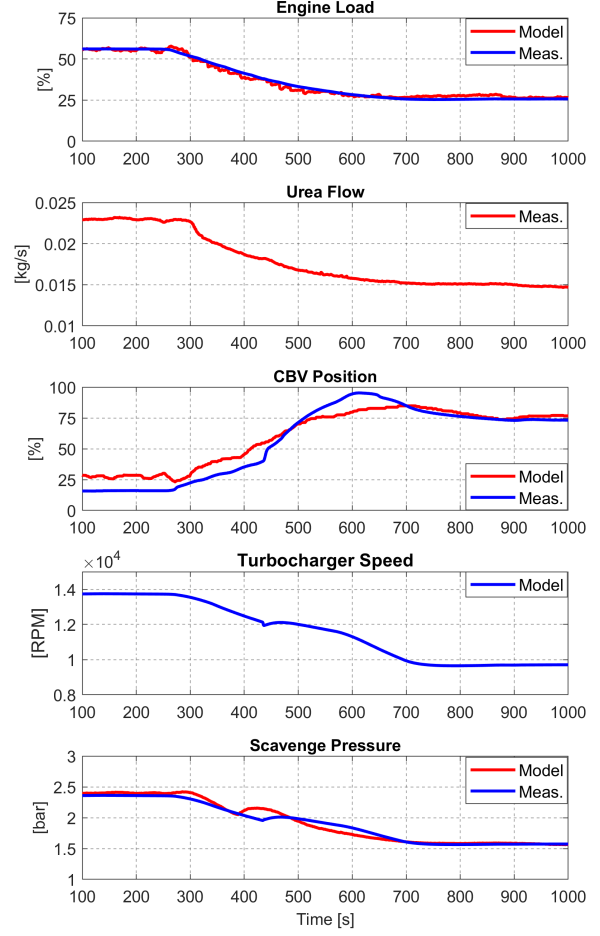
Figure 5-9: Simulation results against on-board measured data for a medium to low load deceleration

5.5 Engine acceleration from low to medium load

In the last validation case, an acceleration from low to medium engine load is examined. The engine operates at steady 30% load for 350 s and accelerates stepwisely to 40% and then to 48% load at 400 s. As in the previous case, the SCR system is engaged, i.e. valve RBV is closed, valves RSV and RTV are fully open and valve CBV is controlled so that exhaust gas temperature at the SCR reactor inlet will remain above the ABS formation limit. In this dataset the measured signals of compression pressure, p_{comp} and maximum combustion pressure, p_{max} were available and are compared with the respective model predictions. At about 430 s, the auxiliary blower is deactivated since scavenge pressure exceeds the blower deactivation pressure of 2.05 bar. The deactivation of the blowers results in a decrease of the airflow entering the engine. However, exhaust gas temperature is not significantly increased after the A/B deactivation due to the simultaneous reduction of CBV opening at about 450 s. When the CBV opening is reduced, less
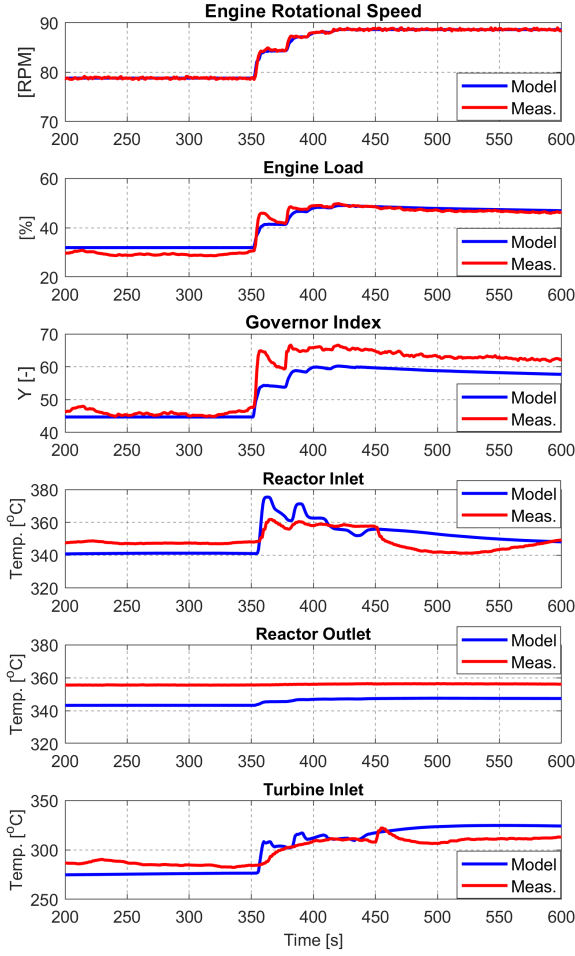
Figure 5-10: Model results against measurements for a low to medium load acceleration
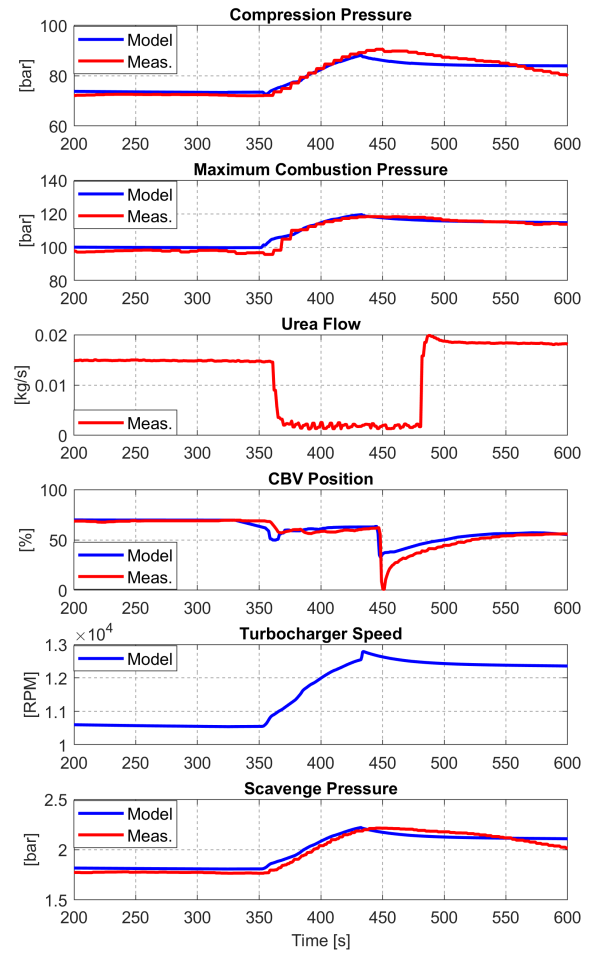
Figure 5-11: Model results against measured data for a low to medium load acceleration

air is directed to the turbine and more air is led to the engine cylinders. Due to the operation of valve CBV, the exhaust gas temperature at the reactor inlet has the same value before and after the load transient and the exhaust gas temperature at the reactor outlet remains practically unchanged. As far as model predictions are concerned, the engine load and governor index predicted by the model are close to measured values and are more smooth than the measured ones during the load transient. On the other hand, the predicted reactor inlet temperature shows higher fluctuations than the measured one. Model prediction of exhaust gas temperature in the turbine inlet is also in good agreement with the measured one. Moreover, the agreement between simulated and measured p_{comp}, p_{max}, and p_{scav} is good both in terms of numerical values and dynamics.

Conclusively, the presented coupled model is able to simulate the dynamic performance of a large two-stroke marine diesel engine equipped with a SCR system during low load acceleration, deceleration and SCR system heating.

THIS PAGE INTENTIONALLY LEFT BLANK

Chapter 6

Model Application and Results

In this chapter, the coupled model is used to investigate the response of the engine-SCR system under transient loading conditions. The inputs to the model were the governor speed setpoint, the temperature setpoint at the CBV controller and the position of valves RBV, RSV and RTV. The simulation cases that were investigated in this chapter are summarized in Table 6.1.

Table 6.1: Investigated simulation cases

Description	Load [%]	Engine Speed [rpm]	Sea condition	Duration [sec]
Effect of blower deactivation	25%-50%	72-91	Calm sea	2000
SCR system disengagement	50%	91	Calm sea	600
Low load acceleration	25%-50%	72-91	Regular waves	550
Low load deceleration	50%-25%	91-72	Regular waves	800
Low load acceleration	25%-50%	72-91	Regular and irregular waves	550

6.1   Simulation of the system under calm weather conditions

6.1.1   Investigation of the effect of Blower Deactivation Pressure

The effect that the deactivation of the auxiliary blowers has on the stability of the engine-turbocharger system, during SCR reactor heating was investigated via simulation. Two blower deactivation pressures were examined: 1.75 bar and 2.25 bar. Simulation results are shown in Figures 6-1 and 6-2, where results for $p_{deact} = 1.75$ bar are shown in red solid line and results for $p_{deact} = 2.25$ bar are shown with blue dashed line. The engine initially operates at 25% load with the auxiliary blowers operating and the reactor outlet temperature at the

beginning of the simulation is 230 ^oC. Valve RBV is fully closed, valve RTV is fully open and CBV is partially open in order to maintain exhaust gas temperature at the SCR reactor inlet above the ABS formation temperature. At 200 sec, the engine speed setpoint is set to 92 RPM which corresponds to 50% load. When the acceleration begins, exhaust gas temperature increases, valve CBV shuts and SCR reactor heating is accelerated due to the increased enthalpy of exhaust gases entering the SCR system The two simulation cases produce identical results until 920 s, when the auxiliary blower with the lower deactivation pressure (red solid line), is deactivated. Due to the sudden decrease of airflow as a result of A/B deactivation, turbocharger speed and scavenge pressure dereasse rapidly. The drop of scavenge pressure further decreases the airflow in the engine which in turn results in an increase of exhaust gas temperature at the reactor inlet. At 980 s, scavenge pressure drops below the blower activation pressure of 1.55 bar and the auxiliary blowers begin operating again. The same pattern of blower activation and deactivation is repeated at 1050 s and 1180 s respectively. Fluctuations at engine speed
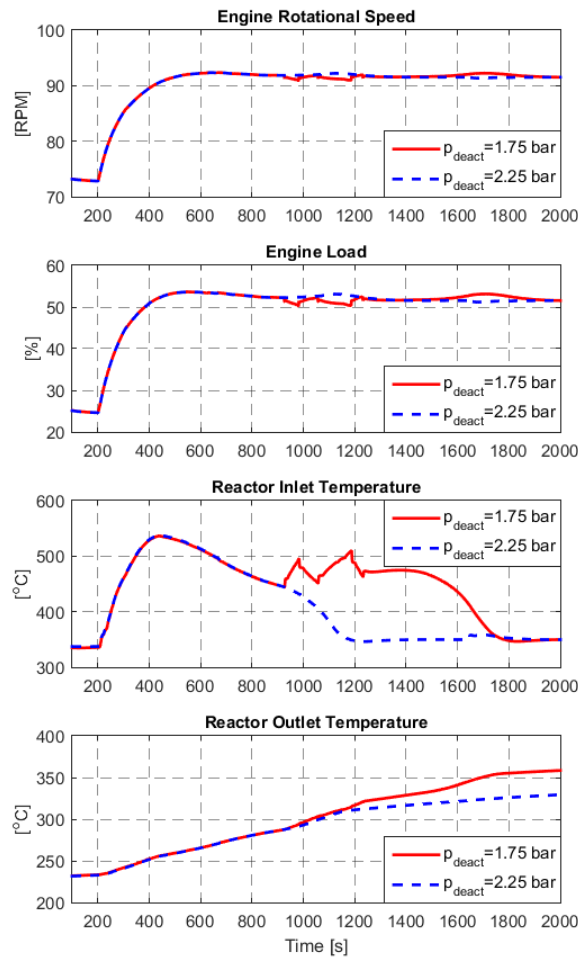

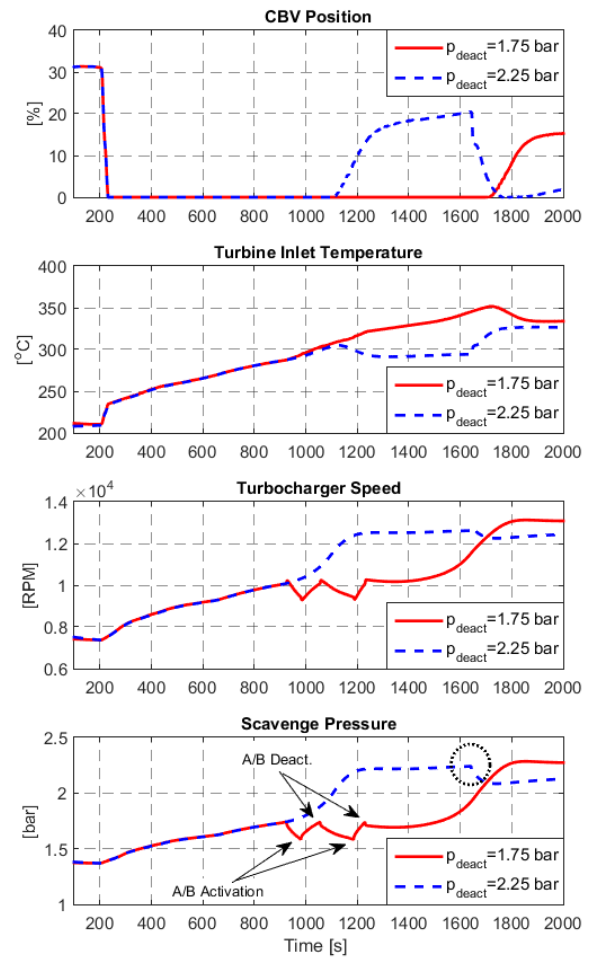Figure 6-1: Simulation results during reactor heating for different blower p_{deact} (a)

Figure 6-2: Simulation results during reactor heating for different blower blower p_{deact} (b)

and load are also present but they are rather small. The heating of the SCR reactor continues despite the temperature fluctuations, since exhaust gas temperature at the inlet of the reactor remains higher than the one at the outlet. At 1230 s the auxiliary blowers are again turned off, but in this case the turbocharger speed does not drop but instead remains constant for about 200 s. The exhaust gas temperature at the outlet the SCR reactor is 320 ^oC which is adequate to sustain the turbocharger. From this simulation case, it is shown that the minimum exhaust gas temperature for smooth SCR operation without the auxiliary blowers engaged is around 320 ^{o}C. As the exhaust gas temperature at the reactor outlet increases, turbocharger speed also increases and temperature at the reactor inlet drops. At 1750 s, valve CBV slightly opens in order to ensure that exhaust gas temperature at the reactor inlet will remain above ABS formation limit. On the other simulation case (blue dotted line), in which the blower p_{deact} is set at 2.25 bar, engine operation is smooth without any instability. At 1650 s, p_{scav} exceeds the blower deactivation pressure and the blowers are turned off (dotted circle). Turbocharger speed slightly drops but no oscillations emerge, since in this case the exhaust gases exiting the SCR system provide the turbocharger with adequate enthalpy.

6.1.2   Simulation of SCR system disengagement

In this simulation case the effect that the disengagement of the SCR system has on engine operation is investigated via simulation. In the beginning of the simulation, the engine operates at steady 50% load at Tier III mode, i.e. valves RSV and RTV are fully open, RBV is fully closed and valve CBV is also closed. At about 300 s the SCR disengagement procedure commences, with the opening of valve RBV. When valve RBV opens entirely, valves RTV and RSV start closing until 410 s when RTV closes completely. Even though RTV closes quite rapidly no fluctuations on turbocharger speed are observed, since the turbine is supplied with enough enthalpy through the fully open valve RBV. The isolation of the SCR system resulted in a lower engine backpressure which in turn led to a turbocharger acceleration. Boost pressure increased by 0.15 bar which resulted to a rise of compression pressure and maximum combustion pressurep_{comp} and p_{max} by 7 bar. Due to the increased in-engine pressures engine load and speed were also slightly increased. Exhaust gas temperature at the exhaust manifold, decreased by 40 ^{o}C due to the higher amount of air that entered the engine which resulted in leaner combution. Gas temperature at the turbine inlet initially increases (between 310 and 350 s), as exhaust gases exiting the SCR system are mixed with the hotter exhaust gases from the exhaust receiver and then decreases
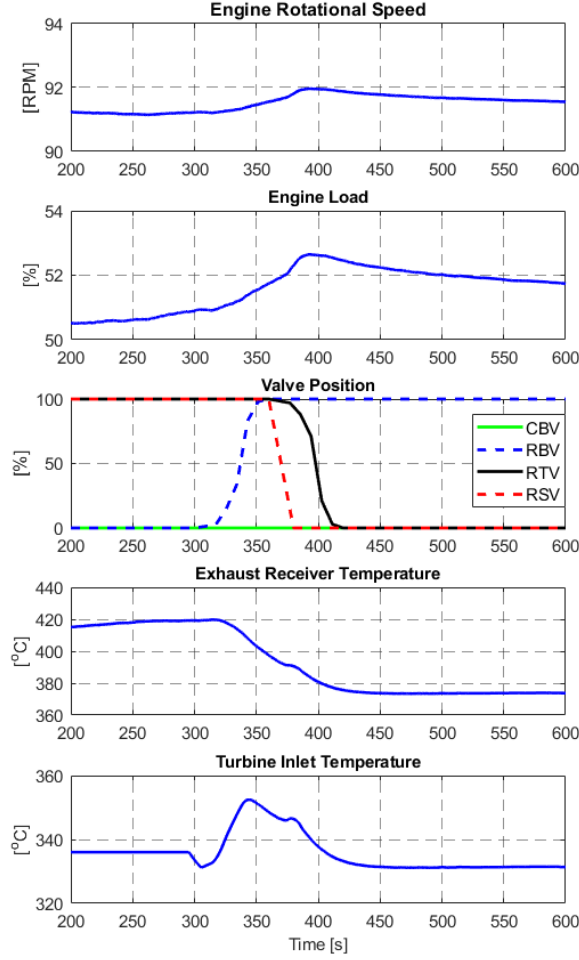
Figure 6-3: Simulation results for a reactor shutting scenario at 50% engine load (a)
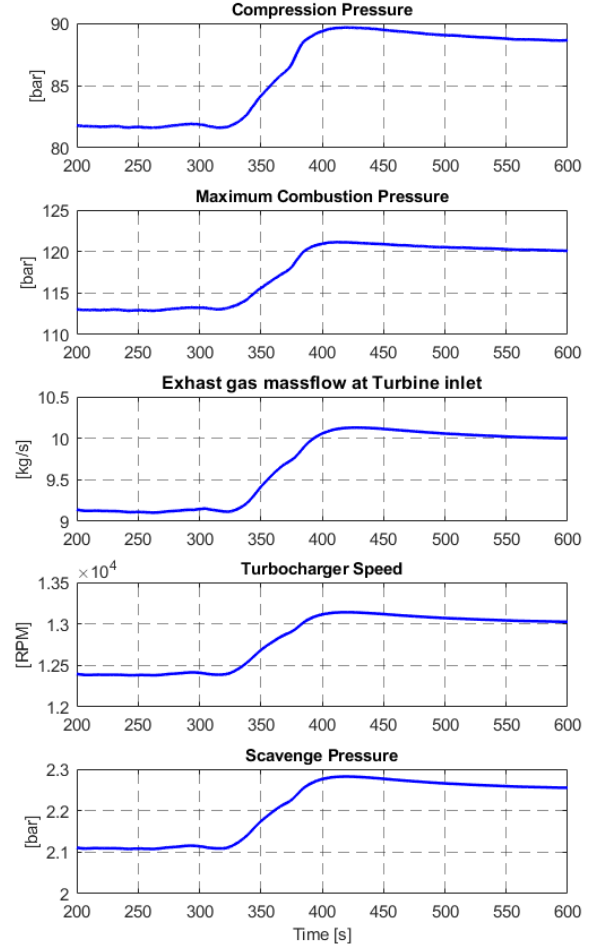
Figure 6-4: Simulation results for a reactor shutting scenario at 50% engine load(b)

due to turbocharger acceleration. Conclusively, no instability on the engine-turbocharger system was observed during the disengagement of the SCR system.

6.2   Simulation of the system under heavy weather conditions

In this section, the coupled model is used to investigate the performance of the system in heavy weather conditions under transient loading. The goal is to examine whether intense variation of propeller load, could be the triggering factor of instability of the engine-turbocharger system. In all simulation cases, the engine operates in Tier III mode, i.e. valve RBV is fully closed, valves RTV and RSV are fully open and the position of valve CBV is controlled using a PID controller. The inputs to the model were the governor speed setpoint and temperature setpoint for the CBV controller. The wave encounter frequency is 180° (head waves) in all the examined cases. As it was mentioned in Section 4.3 the sea environment is modelled using a sea spectrum

and the different sea conditions were modelled by varying the sea spectrum parameters H_s and T_{peak}. In the case of regular waves, a representative regular wave for each specific sea condition was chosen. The frequency of such a representative regular wave corresponds to the circular frequency of the centroid of the spectral area and its amplitude was calculated as below, where $E(S)$ is the spectral area:

$$A_{reg_{rep}} = \sqrt{2E(S)} \tag{6.1}$$

6.2.1 Engine response during a low load acceleration in regular waves

In the first simulation case, an acceleration from low to medium load was examined and simulation results are presented in Figures 6-5 and 6-6. The parameters of the JONSWAP sea spectrum are $H_S = 12.9$ m and $T_{peak} = 10.4$ s and the representative regular wave for this sea spectrum has a wave height of 9 m, a period of 9 s and a wavelength corresponding to λ/L of 0.8. In order to better understand the effect of waves on the operation of the system, simulation results in waves are compared with the ones in calm water conditions. System responses such as engine speed, propeller torque etc. are regular and they vary with the encounter frequency, since the excitation medium is a regular wave. As Fig. 6-5 shows, the propeller demanded torque fluctuates significantly due to the variation of the propeller inflow velocity. This results in a subsequent fluctuation of engine load and exhaust gas temperature. At 25% load, N_{eng} fluctuates around the calm sea value, with an amplitude of 2 RPM and the exhaust gas temperature at the reactor inlet fluctuates with an amplitude of 25 ^{o}C. Due to these fluctuations the exhaust gas temperature at the reactor inlet sometimes drops below 300 ^{o}C which is the limit for ABS formation. As expected, vessel speed is lower in waves due to the effect of wave added resistance. Since, the ship achieves lower speed under the same engine speed, the propeller operates in a lower advance coefficient J, i.e. the propeller is more loaded. To gain a better insight on the system dynamics and the engine-propeller interaction, simulation results from 150 to 180 s are presented in Figure 6-7. Engine torque follows the propeller demanded torque with a time delay of about 1 s as the speed governor manages to keep engine rotational speed around the setpoint. As Eq. 2.11 denotes, when engine torque is higher than the propeller torque the engine accelerates, while when the opposite happens the engine decelerates. Ship motions are quite intense, for example pitch motion has an amplitude of 5 m and this was expected since the wavelength to ship length ratio is close to 1, where wave induced motions are more intense. When due to the combined effect of the free surface elevation and ship motions, the propeller approaches the
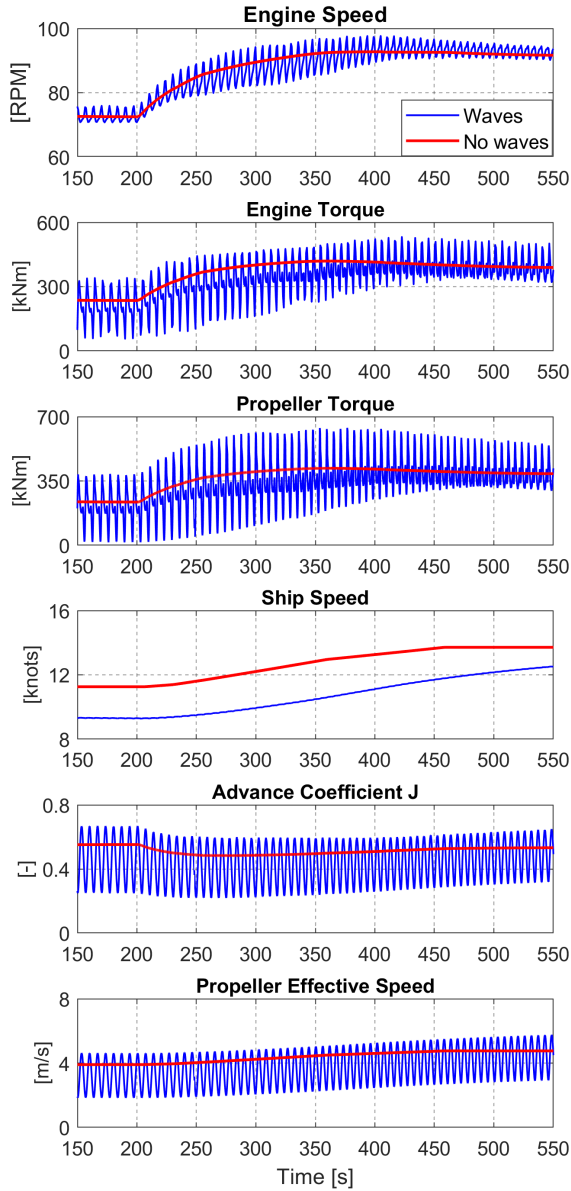
Figure 6-5: Simulation results for a low to medium load acceleration under calm and heavy weather conditions
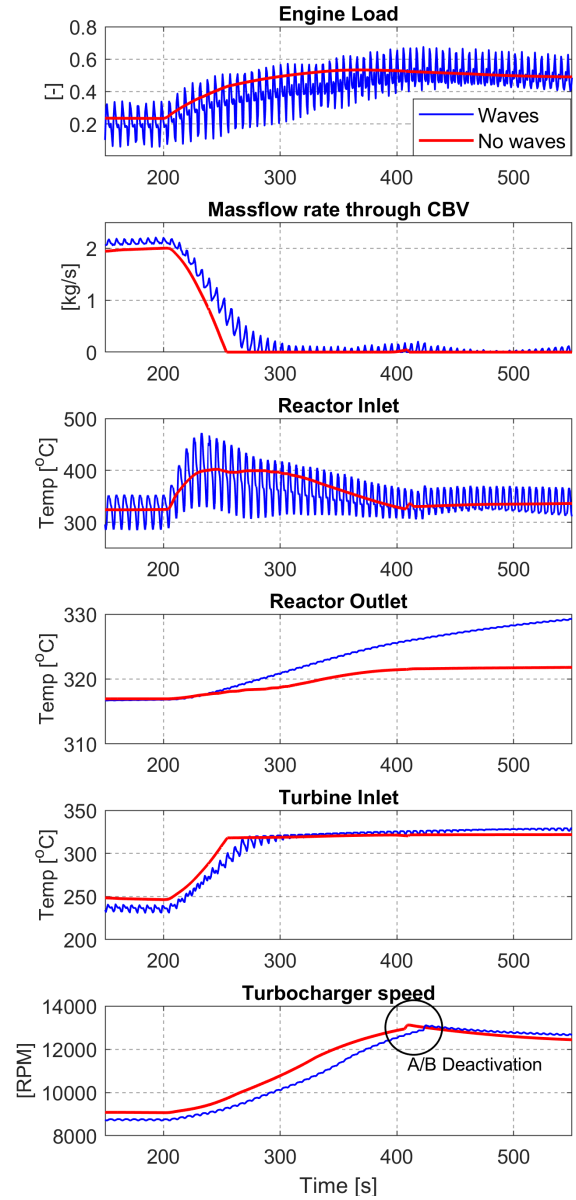
Figure 6-6: Model predictions for a low to medium load acceleration under calm and heavy weather conditions

free surface, propeller torque is reduced due to the effect of the *b* factor which was introduced in Section 4.3.4 (dotted circles in Figure 6-7). This momentary propeller torque loss leads to a momentary engine acceleration. The governor responds by reducing the fuel index, reducing engine torque which subsequently leads to a sudden drop of exhaust gas temperature. During the load transient (between 200 and 400 s), the fuel index is limited by the maximum values imposed by the rotational speed and scavenge pressure limiters. As a result, the available engine torque is bounded and the fluctuations of engine speed increase. The increased fluctuations of engine speed result in a further increase of exhaust gas temperature fluctuations at the reactor
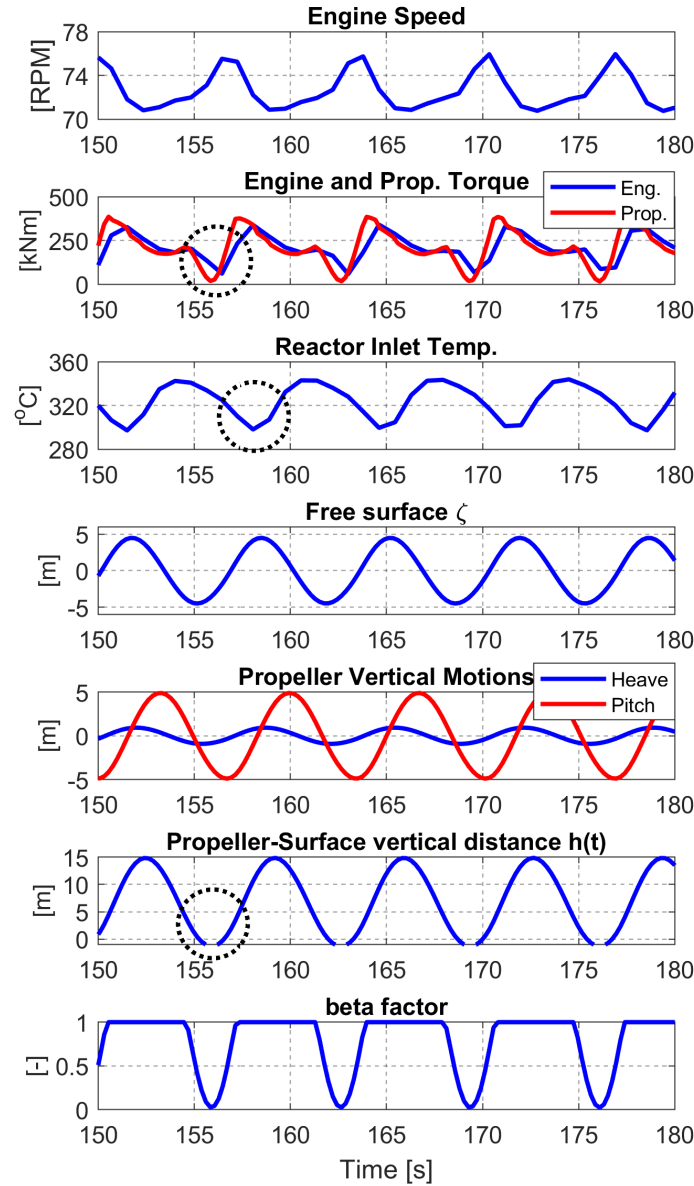
Figure 6-7: Transient simulation results for a low to medium load acceleration under severe weather conditions between 150-180 s

inlet. On the other hand, the exhaust gas temperature at the reactor outlet shows no variation. This is due to the large thermal inertia of the SCR reactor which acts as a filter and smoothens the temperature profile at the reactor outlet. As a result, the temperature profile that the turbocharger encounters is much smoother and hence turbocharger speed shows no oscillations. Even though the exhaust gas temperature at the reactor outlet is higher in the case of waves, the exhaust gas temperature at the turbine inlet is lower. This is owed to the increased massflow of air through valve CBV. The increased amount of air through CBV and the slower acceleration of the engine due to the impact of the limiters, result in a slower turbocharger acceleration in the case of waves.

At about 400 s, p_{scav} exceeds the blower deactivation pressure and the auxiliary blowers (A/B) are deactivated. This results in a small fluctuation at the turbocharger speed and to an increase of exhaust gas temperature due to the decreased airflow in the engine. The effect of blower deactivation on the compressor operating line is shown in Figure 6-8, where the compressor operating line for the two examined cases is presented. It is shown that in heavy weather conditions, the compressor operating point may momentarily lie very close to the compressor surge line during blower deactivation. This would become even more intense in the case of a dirty compressor as, the compressor operating line would move further left and up-wise, making the compressor surge even more likely.
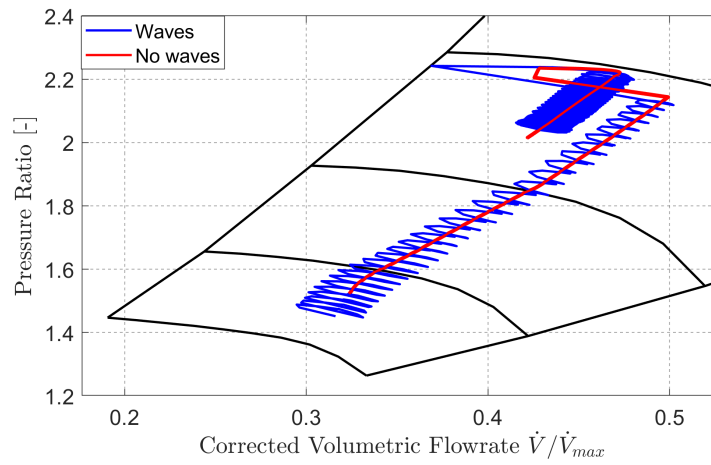
Figure 6-8: Compressor working line during a low to medium load acceleration under calm sea and heavy weather conditions

6.2.2 Engine response during a low load deceleration in regular waves

In the second simulation case, a deceleration from medium to low load was investigated. In this case, a milder sea condition was examined, where the parameters of the JONSWAP sea spectrum were $H_s = 11.4\ m$ and $T_{peak} = 9.3\ s$. The representative regular wave for this sea spectrum has a wave height H=8 m and a period T=8 s. Simulation results for heavy and calm weather conditions are presented in Figures 6-9 and 6-10. At the beginning of the simulation, the engine operates at steady 55% load at 94.5 RPM and at 280 sec the engine begins to decelerate until it reaches 27% load at 74 RPM. System responses oscillate with a smaller amplitude than in Section 6.2.1, since a milder sea state is simulated. Simulation results between 150 s and 180 s are shown in Figure 6-11. The wave encounter frequency is higher in this simulation scenario, which leads to reduced propeller vertical motions. As a result, even though propeller inflow velocity fluctuations lies in the same levels as in the previous case, torque fluctuations are
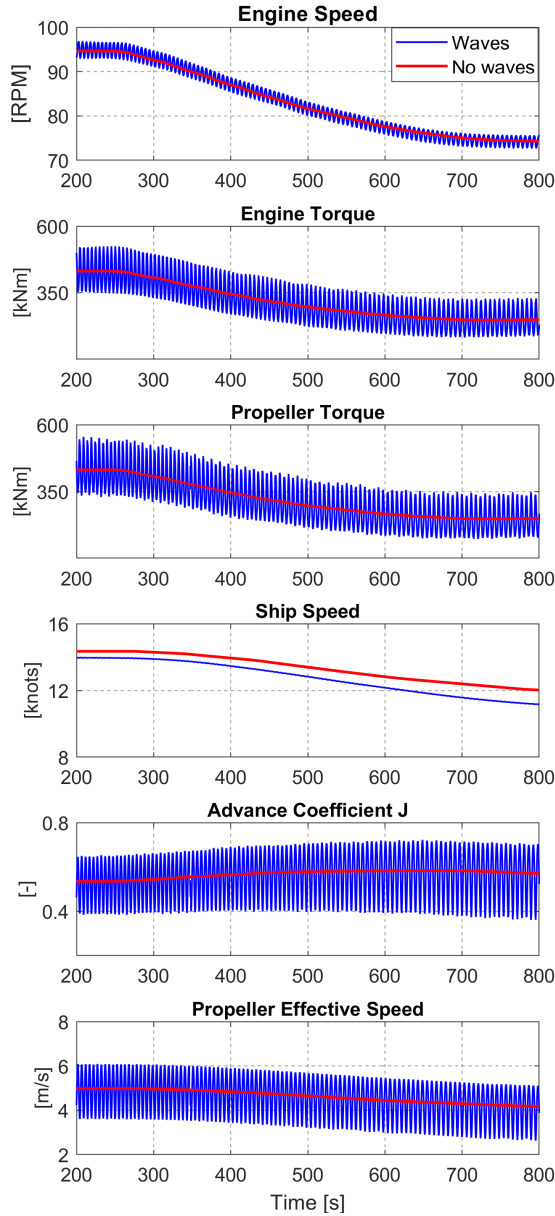
Figure 6-9: Simulation results for medium to low load deceleration under calm and heavy weather conditions
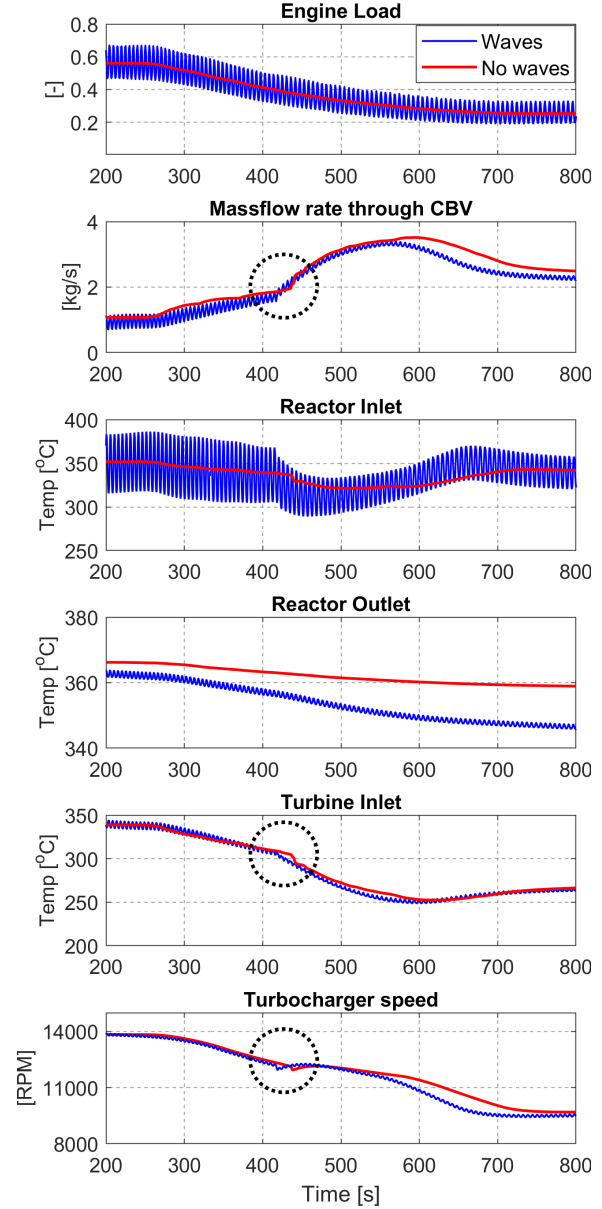
Figure 6-10: Model predictions for medium to low load deceleration under calm and heavy weather conditions

smaller. This is shown in the last 3 graphs of Figure 6-11 where the propeller vertical motions, propeller-surface distance and the beta factor are shown. Propeller vertical displacement due to pitch motion is four times smaller compared to the previous simulation scenario. As a result, the sudden drops of torque and exhaust gas temperature are not present in this case. The free surface varies between 4 and -4 m with the wave frequency of 8 s, while engine and ship responses vary with the encounter frequency. The engine produced torque follows the propeller demanded torque with a time delay of around 1 s. Also, the reduced wave excited motions lead to lower wave added resistance and as a result ship speed in waves is higher than the one in the previous
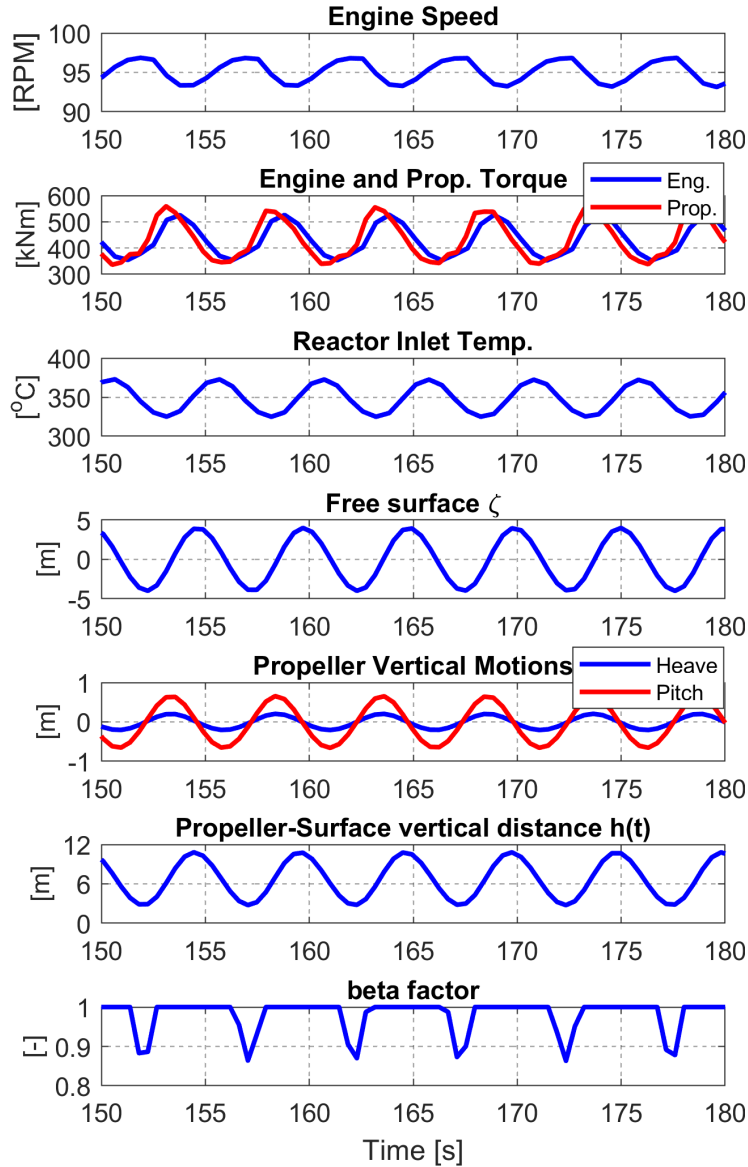
Figure 6-11: Simulation results for medium to low load deceleration under calm and heavy weather conditions

simulation case. Valve CBV, is initially open in order to ensure that exhaust gas temperature at the reactor inlet will remain above the critical ABS formation limit. When the deceleration commences, CBV opens even more in order to bypass more air from the engine cylinders. In this way, combustion becomes richer which leads to higher exhaust gas temperature. At about 420 s, p_{scav} drops below the auxiliary blower activation pressure of 2.05 bar and the auxiliary blowers begin to operate. This results in an increase of the airflow entering the engine and hence, to a decrease of exhaust gas temperature. In order to counteract this, at 420 s valve CBV opens further, bypassing more air from the cylinders directly to the turbine, which leads to a more rapid decrease of the turbine inlet temperature.

6.2.3 Engine response during a low load acceleration in regular and irregular waves

In this simulation scenario, irregular waves are applied to the system. The system's response in irregular waves is shown in Figures 6-12 and 6-13 where it is compared with the respective response in regular waves. The sea spectrum parameters are $H_s = 8$ m, $T_{peak} = 8$ s and the representative regular wave for this sea spectrum has a height of 5.6 m, a period of 6.7 s and a wavelength of 70 m. This wavelength corresponds to about half the ship length ($\lambda = 0.44$ L). Apart from some spikes that appear, fluctuations of thermodynamic and hydrodynamic parameters are most of the time smaller than the ones in regular waves. Engine response during
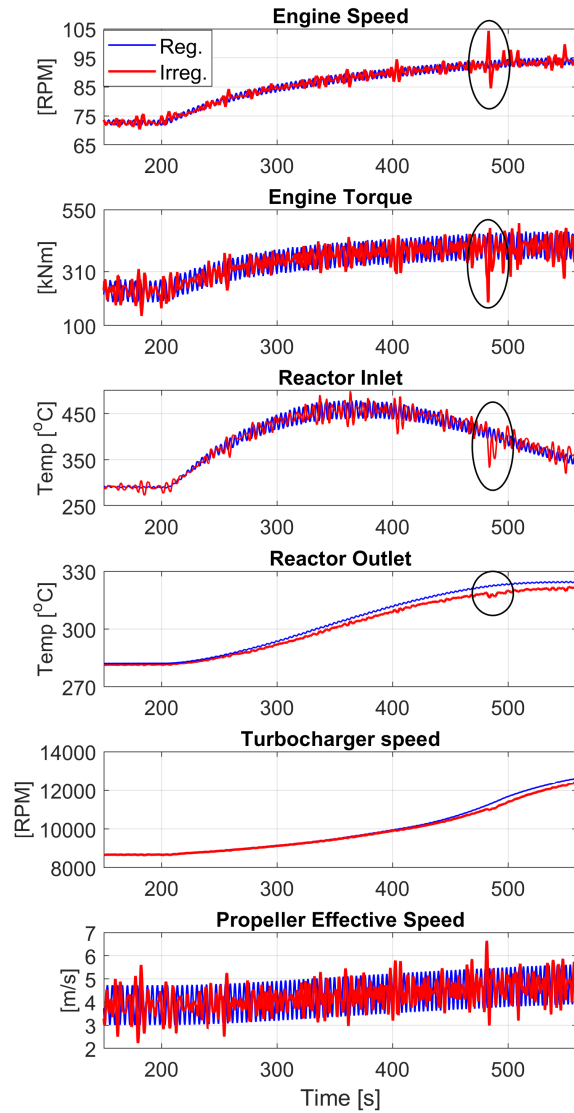
Figure 6-12: Simulation results for a 25% to 50% load acceleration in heavy weather conditions for regular and irregular waves
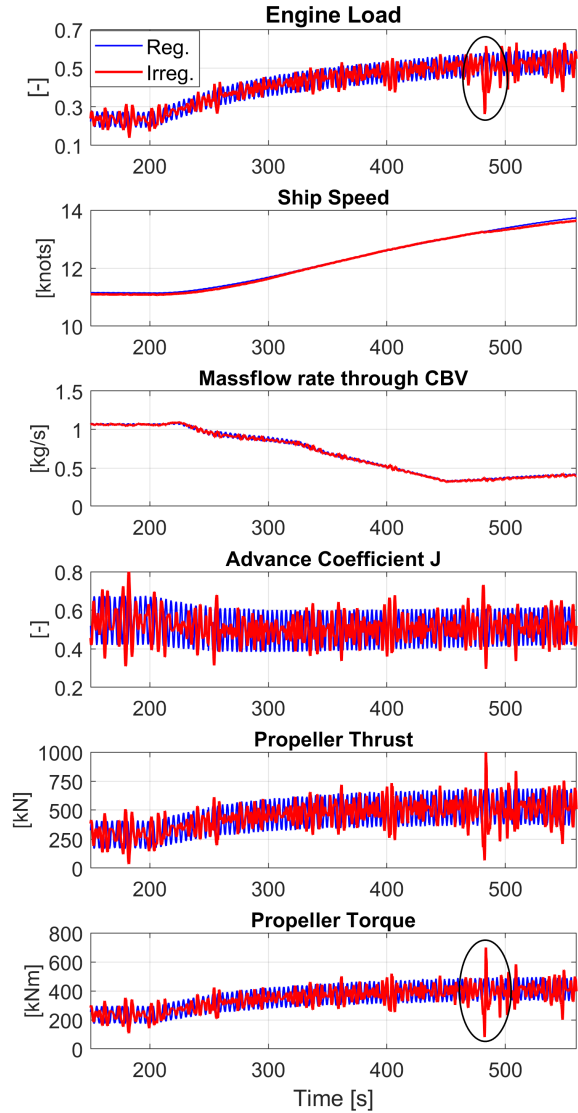
Figure 6-13: Model predictions for a 25% to 50% load increase scenario in heavy weather conditions for regular and irregular waves

acceleration is quite similar in both cases. This is an indication that the chosen regular wave is indeed representative of this sea state. Ship speed is the same in regular and irregular waves, since the wave added resistance is the same and calculated as in Eq. (4.28), using the same sea spectrum. Moreover, exhaust gas temperature at the reactor outlet is slightly higher in the case of regular waves leading to a slightly faster turbocharger acceleration. This is an indication that the engine is slightly more loaded in case of regular waves. A sudden decrease of propeller demanded torque takes place at about 480 s (ellipse in Fig. 6-13). This results in a significant fluctuation of engine produced torque, engine speed and exhaust gas temperature (ellipses in Fig. 6-12). Engine torque is momentarily reduced by 200 kNm and exhaust gas temperature
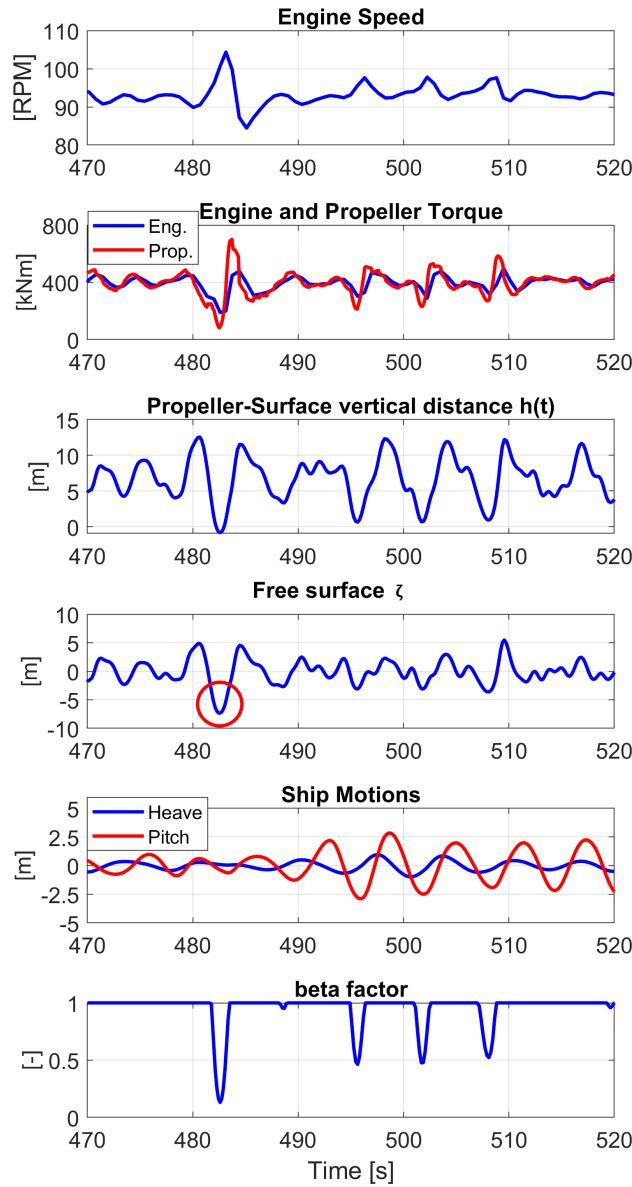
Figure 6-14: Thermodynamic and hydrodynamic simulation results for 470-520 s, where an engine speed spike is observed

at the reactor inlet drops by around 70 ^{o}C. On the contrary, exhaust gas temperature at the SCR reactor outlet remains relatively unaffected (circle at Fig. 6-13). In order to understand the reason behind this propeller torque spike, engine speed, torque and ship motions results for 470-520 s, are shown in Fig. 6-14. It is observed that, engine torque follows the propeller torque with a time delay of 0.5 s, as the governor manages to maintain engine speed around the speed setpoint. As expected, when the engine torque is higher than the propeller torque, the engine accelerates, while when the opposite happens the engine decelerates. As Fig. 6-14 shows, the main reason behind this torque spike is a large trough of the free surface ζ at about 483 s (shown with a red circle), which caused the propeller-surface distance $h(t)$ to decrease significantly. As a result, the propeller torque decreased due to the effect of the b factor which led to a significant engine acceleration. The speed governor responded by reducing the fuel in the engine, hence the reduced engine torque and exhaust gas temperature at Fig. 6-12. Smaller engine speed spikes also take place at 497 s, 502 s and 509 s. In those cases as well, a torque loss takes place due to the propeller proximity to the free surface (note the reduction of the b factor), due to increased pitch motions of the vessel at the respective time instants.

It has to be underlined that the irregular free surface in this simulation case is just one possible representation of this sea spectrum. Since, the phases of the components that compose the irregular waves are produced using a random number generator, an infinite number of possible free surface representations can be generated. Nevertheless, a sound idea of the combined system's response in heavy irregular seas can be obtained by this simulation.

Note: It was observed that when the vessel operates in waves it may face extreme operating conditions due to propeller racing. These extreme operating cases can be known a priori if more complicated methods of stochastic analysis are employed.

THIS PAGE INTENTIONALLY LEFT BLANK

Chapter 7

Conclusions

In this work, the transient response of a large two-stroke marine diesel engine coupled to a high pressure SCR exhaust aftertreatment system was investigated through simulation. Zero dimensional models for the two-stroke diesel engine and the SCR system were developed and validated against available measured data. With a view of obtaining an accurate prediction of propeller load during load transients, models for the propeller and the ship hull were also developed and integrated with the engine model, enabling the simulation of the entire propulsion system. The coupled model was validated against available on-board measured data, obtained from an operating commercial vessel. The model is able to capture the transient behavior of the marine propulsion plant during acceleration, deceleration and SCR system heating.

The main challenge that the SCR system introduces on engine operation is associated with the large thermal inertia of the SCR reactor. Due to its large thermal inertia, the SCR system requires a significant amount of time to reach operational temperature. In the case that was examined in this work, the SCR reactor required 1 hour to reach the appropriate temperature for SCR operation while the engine was operating at 72% load. The SCR system was found to have an increasing inertial effect on the engine-turbocharger system as engine load decreased. As a result, thermal instability of the engine-turbocharger system might emerge during low load operation, where the effect is more pronounced. Simulations showed, that the deactivation of the auxiliary blowers during SCR heating may lead to a sudden decrease of available enthalpy to the turbine and become the triggering factor of engine-turbocharger instability. A critical exhaust gas temperature limit the at turbine inlet, above which instabilities are avoided was found to be 320 ^{o}C. In order to prevent any such instabilities, auxiliary blowers should operate until exhaust gas temperature at the reactor outlet reaches that limit. Moreover, the disengagement of the

SCR system at medium engine load was examined, without detecting any serious implications in engine operation.

Also, the operation of the engine-SCR system, when the vessel sails in a seaway with heavy weather conditions was investigated. The performance of the system was examined in both regular and irregular waves. Significant engine speed and torque fluctuations appear in the presence of both regular and irregular waves mainly due to the variation of propeller inflow velocity. Torque loss due to the propeller emergence to the free surface is also a factor contributing to fluctuations of engine speed. As far as SCR operation is concerned, it was found that the torque and temperature fluctuations due to the operation in heavy seas do not cause instability of the engine-turbocharger system. This is due to the different time constants of the various subsystems. For example, engine torque fluctuates with the encounter frequency which is around 7-12 s in head seas, while the period of temperature oscillations is much higher, around 200 s. Engine performance in regular and irregular waves did not show significant differences apart from some spikes that were present during operation in irregular waves due to propeller emergence to the free surface, as a result of intense ship motions.

Conclusively, when IMO III regulation was announced there were quite a few researchers that underlined the susceptibility of the High Pressure SCR system to thermal instability especially during low load operation (1), (2). In this thesis it was found that such instabilities can be prevented and the engine is able to operate safely even at very low load, or heavy weather conditions with the SCR system engaged.

Future Work

- It would be of interest to investigate the performance of a two-stroke diesel engine equipped with an SCR system during extreme manoeuvring conditions, such as crash stop or crash ahead manoeuvres.

- In this work the DeNOx performance of the SCR catalyst was not studied. To the author's opinion, it is of high interest to investigate the performance of the catalyst in terms of NOx reduction during load transients.

- If the above DeNOx chemical kinetics model is developed, different urea dosing control strategies can be investigated.

- Both during model validation and model application, measured time series of RBV and

RTV valves were used as input to the model. It would be of interest to develop a control scheme that would predict the position of RBV and RTV valves. In this way, different reactor heating scenarios could be investigated. The criterion for heating should be a balance between heating time and on the other hand, not subtracting too much energy from the turbocharging as this would increase combustion chamber component temperatures.

THIS PAGE INTENTIONALLY LEFT BLANK

Appendix A

Calculation of Temperature Gradients for SCR model

The coefficients C_1-C_{18} that are used for the calculation of the temperature gradients of the exhaust gas, catalyst block and wall are presented in this section.

A.1 Vaporizer/Pipe

A.1.1 Exhaust Gas

The temperature gradient of the exhaust gas in the vaporizer/pipe is calculated as below:

$$\left(\frac{dT}{dt}\right)_{exh,j} = C_1(T_{exh,j-1} - T_{exh,j}) - C_2(T_{exh,j} - T_{wall,j}) - C_3(T_{exh,j}^4 - T_{wall,j}^4) - dT_{ch,vap} \quad \text{(A.1)}$$

Where:

$$C_1 = \frac{\dot{m}_{exh}}{m_{exh}} \quad \textit{Exhaust gas mixing term} \quad \text{(A.2)}$$

$$C_2 = \frac{h_{exh}A_{gw}}{m_{exh}c_{exh}} \quad \textit{Gas} - \textit{wall convection} \quad \text{(A.3)}$$

$$C_3 = \frac{\sigma\epsilon A_{gw}}{m_{exh}c_{exh}} \quad \textit{Gas} - \textit{wall convection} \quad \text{(A.4)}$$

A.1.2 Vaporizer/Pipe Wall

The temperature gradient of the wall in the vaporizer/pipe is calculated as below:

$$\left(\frac{dT}{dt}\right)_{wall,j} = C_4(T_{exh,j} - T_{wall,j}) + C_5(T_{exh,j}^4 - T_{wall,j}^4) - C_6(T_{wall,j} - T_{amb}) \quad \text{(A.5)}$$

Where:

$$C_4 = \frac{h_{exh}A_{gw}}{m_{wall}c_{wall}} \quad Gas - wall\ convection \tag{A.6}$$

$$C_5 = \frac{\sigma\epsilon A_{gw}}{m_{wall}c_{wall}} \quad Gas - wall\ radiation \tag{A.7}$$

$$C_6 = \frac{1}{(R_{wall} + R_{ins} + R_{amb})(m_{wall}c_{wall})} \quad Wall to ambient \tag{A.8}$$

A.2   SCR Reactor

A.2.1   Exhaust Gas

The temperature gradient of the exhaust gas in the SCR reactor is calculated as:

$$\left(\frac{dT}{dt}\right)_{exh,j} = C_7(T_{exh,j-1} - T_{exh,j}) - C_8(T_{exh,j} - T_{cat,j}) - C_9(T_{exh,j} - T_{wall,j})$$
$$- C_{10}(T_{exh,j}^4 - T_{cat,j}^4) - C_{11}(T_{exh,j}^4 - T_{wall,j}^4) + dT_{ch,reac} \tag{A.9}$$

$$C_7 = \frac{\dot{m}_{exh}}{m_{exh}} \quad Exhaust\ gas\ mixing\ term \tag{A.10}$$

$$C_8 = \frac{h_{cat}A_{cat}}{m_{exh}c_{exh}} \quad Gas - catalyst\ convection \tag{A.11}$$

$$C_9 = \frac{h_{exh}A_{gw}}{m_{exh}c_{exh}} \quad Gas - wall\ convection \tag{A.12}$$

$$C_{10} = \frac{\sigma\epsilon A_{cat}}{m_{exh}c_{exh}} \quad Gas - catalyst\ radiation \tag{A.13}$$

$$C_{11} = \frac{\sigma\epsilon A_{gw}}{m_{exh}c_{exh}} \quad Gas - wall\ radiation \tag{A.14}$$

A.2.2   Catalyst Block

The temperature gradient of the exhaust gas in the catalyst block is calculated as below:

$$\left(\frac{dT}{dt}\right)_{cat,j} = C_{12}(T_{exh,j} - T_{cat,j}) + C_{13}(T_{exh,j}^4 - T_{cat,j}^4) - C_{14}(T_{cat,j} - T_{wall}) \tag{A.15}$$

Where:

$$C_{12} = \frac{h_{cat}A_{cat}}{m_{cat}c_{cat}} \quad Gas - catalyst\ convection \tag{A.16}$$

$$C_{13} = \frac{\sigma\epsilon A_{cat}}{m_{cat}c_{cat}} \quad Catalyst - wall\ radiation \tag{A.17}$$

$$C_{14} = \frac{1}{R_{cond}m_{cat}c_{cat}} \quad Catalyst - wall\ conduction \tag{A.18}$$

A.2.3 SCR Reactor Wall

The temperature gradient of the wall in the reactor is calculated as below:

$$\left(\frac{dT}{dt}\right)_{wall,j} = C_{15}(T_{exh,j}-T_{wall,j})+C_{16}(T_{exh,j}^4-T_{wall,j}^4)+C_{17}(T_{cat,j}-T_{wall,j})-C_{18}(T_{wall,j}-T_{amb})$$

(A.19)

$$C_{15} = \frac{h_{exh}A_{gw}}{m_{wall}c_{wall}} \quad Gas-wall\ convection$$

(A.20)

$$C_{16} = \frac{\sigma\epsilon A_{gw}}{m_{wall}c_{wall}} \quad Gass-wall\ radiation$$

(A.21)

$$C_{17} = \frac{1}{R_{cond}m_{wall}c_{wall}} \quad Catalyst-wall\ conduction$$

(A.22)

$$C_{18} = \frac{1}{(R_{wall}+R_{ins}+R_{amb})(m_{wall}c_{wall})} \quad Wall\ to\ ambient$$

(A.23)

THIS PAGE INTENTIONALLY LEFT BLANK

Bibliography

[1] T. Fujibayashi, S. Baba, and H. Tanaka, "Development of marine SCR system for large two-stroke diesel engines complying with IMO NOx Tier III." 27th CIMAC Congress, Shanghai, China, May 13th to May 16th, 2013.

[2] E. Codan, S. Bernasconi, and H. Born, "IMO III emission regulation: Impact on the turbocharging system." 26th CIMAC Congress, Bergen, Norway June 14th to June 17th, 2010.

[3] International Maritime Organization, *MARPOL : Annex VI and NTC 2008 with guidelines for implementation*, 3rd ed. IMO, 2013.

[4] ——, "Report of the marine environment protection committee on its seventy-first session, annex 1 resolution MEPC.286(71), (designation of the baltic sea and the north sea emission control areas)," IMO, London, United Kingdom, Tech. Rep., 2017.

[5] J. B. Heywood, *Internal Combustion Engine Fundamentals*. McGraw-Hill, 1988.

[6] P. Andreadis, A. Zompanakis, C. Chryssakis, and L. Kaiktsis, "Effects of the fuel injection parameters on the performance and emissions formation in a large-bore marine diesel engine," *International Journal of Engine Research*, vol. 12, no. 1, pp. 14–29, 2011. [Online]. Available: https://doi.org/10.1243/14680874JER511

[7] H. Liu, L. Lu, and Z. Wang, "Studying on fuel injection strategies on the performance of two-stroke marine diesel engine," in *SAE Technical Paper*, no. 2014-01-2706. SAE International, October 2014. [Online]. Available: https://doi.org/10.4271/2014-01-2706

[8] L. Feng, J. Tian, W. Long, W. Gong, B. Du, D. Li, and L. Chen, "Decreasing NOx of a low-speed two-stroke marine diesel engine by using in-cylinder emission control measures," *Energies*, vol. 9, no. 4, p. 304, 2016. [Online]. Available: https://doi.org/10.3390/en9040304

[9] F. X. Tanner, M. Brunner, and G. Weisser, "A computational investigation of water injection strategies for nitric oxide reduction in large-bore DI diesel engines," in *SAE Technical Paper*, no. 2001-01-1069. SAE International, March 2001. [Online]. Available: https://doi.org/10.4271/2001-01-1069

[10] C. Chryssakis, L. Kaiktsis, and A. Frangopoulos, "Computational investigation of in-cylinder NOx emissions reduction in a large marine diesel engine using water addition strategies," in *SAE Technical Paper*, no. 2010-01-1257. SAE International, April 2010. [Online]. Available: https://doi.org/10.4271/2010-01-1257

[11] MAN Energy Solutions, "Emission project guide," Copenhagen SV, Denmark, Tech. Rep., 2018.

[12] K. Sandelin and D. Peitz, "SCR under pressure: Pre turbocharger NOx abatement for marine 2-stroke diesel engines," no. 111. 28th CIMAC Congress, Helsinki, Finland, June 6th to June 10th, 2016.

[13] I. Nova and E. Tronconi, *Urea-SCR Technology for deNOx After Treatment of Diesel Exhausts*. Springer-Verlag New York, 2014, ch. 13, p. 387. [Online]. Available: https://doi.org/10.1007/978-1-4899-8071-7

[14] M. Foteinos, S. Konstantinidis, N. Kyrtatos, and K. Busk, "Simulation of the transient thermal response of a high pressure selective catalytic reduction aftertreatment system for a Tier III two-stroke marine diesel engine," *ASME J. Eng. for Gas Turbines and Power*, vol. 141, no. 7, 2019. [Online]. Available: https://doi.org/10.1115/1.4042131

[15] N. Kyrtatos and I. Koumbarelis, "Performance prediction of next generation slow speed marine diesel engines during ship manoeuvres," *Transactions of The Institute of Marine Engineers*, vol. 106, 1994.

[16] A. G. Livanos, G. Theotokatos, and N. P. Kyrtatos, "Simulation of large marine two-stroke diesel engine operation during fire in the scavenging air receiver," *Journal of Marine Engineering & Technology*, vol. 2, no. 2, pp. 9–16, 2003. [Online]. Available: https://doi.org/10.1080/20464177.2003.11020170

[17] N. Kyrtatos, G. Theotokatos, N. Xiros, K. Marec, and R. Duge, "Transient operation of large-bore two-stroke marine diesel engine powerplants: measurements and simulations." 23rd CIMAC Congress, Hamburg, Germany, May 7th to May 10th, 2001.

[18] S. I. Raptotasios, N. F. Sakellaridis, R. G. Papagiannakis, and D. T. Hountalas, "Application of a multi-zone combustion model to investigate the NOx reduction potential of two-stroke marine diesel engines using EGR," *Applied Energy*, vol. 157, pp. 814 – 823, 2015. [Online]. Available: https://doi.org/10.1016/j.apenergy.2014.12.041

[19] D. T. Hountalas, "Prediction of marine diesel engine performance under fault conditions," *Applied Thermal Engineering*, vol. 20, no. 18, pp. 1753 – 1783, 2000. [Online]. Available: https://doi.org/10.1016/S1359-4311(00)00006-5

[20] J. Woodward and R. Latorre, "Modeling of diesel engine transient behavior in marine propulsion analysis," *Transactions - Society of Naval Architects and Marine Engineers*, vol. 92, pp. 33 – 49, 1985.

[21] E. Hendricks, "Mean value modelling of large turbocharged two-stroke diesel engines," in *SAE Technical Paper*, no. 890564.   SAE International, February 1989. [Online]. Available: https://doi.org/10.4271/890564

[22] M. Blanke and J. Andersen, "On modelling large two stroke diesel engines: New results from identification," *IFAC Proceedings Volumes*, vol. 17, no. 2, pp. 2015 – 2020, 1984, 9th IFAC World Congress: A Bridge Between Control Science and Technology, Budapest, Hungary, 2-6 July. [Online]. Available: https://doi.org/10.1016/S1474-6670(17)61272-2

[23] C. Guan, G. Theotokatos, P. Zhou, and H. Chen, "Computational investigation of a large containership propulsion engine operation at slow steaming conditions," *Applied Energy*, vol. 130, pp. 370 – 383, 2014. [Online]. Available: https://doi.org/10.1016/j.apenergy.2014.05.063

[24] F. Baldi, G. Theotokatos, and K. Andersson, "Development of a combined mean value-zero dimensional model and application for a large marine four-stroke diesel engine simulation," *Applied Energy*, vol. 154, pp. 402 – 415, 2015. [Online]. Available: https://doi.org/10.1016/j.apenergy.2015.05.024

[25] C. Guan, G. Theotokatos, and H. Chen, "Analysis of two stroke marine diesel engine operation including turbocharger cut-out by using a zero-dimensional model," *Energies*, vol. 8, no. 6, pp. 5738 – 5764, June 2015. [Online]. Available: https://doi.org/10.3390/en8065738

[26] G. Theotokatos, C. Guan, H. Chen, and I. Lazakis, "Development of an extended mean value engine model for predicting the marine two-stroke engine operation at varying settings," *Energy*, vol. 143, pp. 533 – 545, 2018. [Online]. Available: https://doi.org/10.1016/j.energy.2017.10.138

[27] Y. Tang, J. Zhang, H. Gan, B. Jia, and Y. Xia, "Development of a real-time two-stroke marine diesel engine model with in-cylinder pressure prediction capability," *Applied Energy*, vol. 194, pp. 55 – 70, 2017. [Online]. Available: https://doi.org/10.1016/j.apenergy.2017.03.015

[28] D. Chatterjee, T. Burkhardt, M. Weibel, E. Tronconi, I. U, and C. Ciardelli, "Numerical simulation of NO/NO2/NH3 reactions on SCR-catalytic converters:model development and applications," in *SAE Technical Paper*, no. 2006-01-0468. SAE International, April 2006. [Online]. Available: https://doi.org/10.4271/2006-01-0468

[29] L. Guzzella and C. Onder, *Introduction to Modeling and Control of Internal Combustion Engine Systems*. Springer-Verlag Berlin Heidelberg, 2014, ch. 2, p. 123. [Online]. Available: https://doi.org/10.1007/978-3-642-10775-7

[30] C. M. Schar, C. H. Onder, and H. P. Geering, "Control of an SCR catalytic converter system for a mobile heavy-duty application," *IEEE Transactions on Control Systems Technology*, vol. 14, no. 4, pp. 641–653, July 2006. [Online]. Available: https://doi.org/10.1109/TCST.2006.876634

[31] C. Ericson, B. Westerberg, and I. Odenbrand, "A state-space simplified SCR catalyst model for real time applications," in *SAE Technical Paper*, no. 2008-01-0616. SAE International, April 2008. [Online]. Available: https://doi.org/10.4271/2008-01-0616

[32] P. Chen and J. Wang, "Control-oriented model for integrated diesel engine and aftertreatment systems thermal management," *Control Engineering Practice*, vol. 22, pp. 81 – 93, 2014. [Online]. Available: https://doi.org/10.1016/j.conengprac.2013.09.009

[33] ——, "Control-Oriented Modeling and Observer-Based Estimation of Solid and Gas Temperatures for a Diesel Engine Aftertreatment System," *Journal of Dynamic Systems, Measurement, and Control*, vol. 134, no. 6, September 2012. [Online]. Available: https://doi.org/10.1115/1.4006632

[34] N. Pedersen, T. Bojsen, J. Madsen, and M. Vejlgaard-Laursen, "FMI for co-simulation of embedded control software." First Japanese Modelica Conference, Tokyo, Japan, May 23th to May 24th, 2016, pp. 70–77.

[35] Z. Skaf, T. Aliyev, L. Shead, and T. Steffen, "The state of the art in selective catalytic reduction control," in *SAE Technical Paper*, no. 2014-01-1533. SAE International, April 2014. [Online]. Available: https://doi.org/10.4271/2014-01-1533

[36] Y. Xiao, H. Zhao, X. Tian, and W. Tan, "Investigation on the Control Strategy for Marine Selective Catalytic Reduction System," *Journal of Dynamic Systems, Measurement, and Control*, vol. 141, no. 1, September 2018. [Online]. Available: https://doi.org/10.1115/1.4041011

[37] S. R. Christensen, B. B. Hansen, K. H. Pedersen, J. R. Thogersen, and A. D. Jensen, "Selective Catalytic Reduction of NOx over V2O5-WO3-TiO2 SCR Catalysts, A Study at Elevated Pressure for Maritime Pre-turbine SCR Configuration," *Emission Control Science and Technology*, vol. 5, no. 3, pp. 263–278, September 2019. [Online]. Available: https://doi.org/10.1007/s40825-019-00127-0

[38] U. Campora and M. Figari, "Numerical simulation of ship propulsion transients and full-scale validation," *Proceedings of the Institution of Mechanical Engineers, Part M: Journal of Engineering for the Maritime Environment*, vol. 217, no. 1, pp. 41 – 52, 2003. [Online]. Available: https://doi.org/10.1243/147509003321623130

[39] G. Benventuto, S. Brizzolara, and M. Figari, "Simulation of the propulsion system behaviour during ship standard maneuvres." Proceedings of the Eighth International Symposium on Practical Design of Ships and Other Floating Structures, 2001, pp. 657–663.

[40] G. Livanos, G. Simotas, G. Dimopoulos, and N. Kyrtatos, "Simulation of marine diesel engine propulsion system dynamics during extreme maneuvering." ASME 2006 Internal Combustion Engine Division Spring Technical Conference (ICES2006), 2006, pp. 569–577. [Online]. Available: https://doi.org/10.1115/ICES2006-1366

[41] G. Livanos, G. Papalambrou, and N. Kyrtatos, "Electronic engine control for ice operation of tankers." 25th CIMAC Congress, Vienna, Austria, May 21st to May 24th, 2007.

[42] X. Llamas and L. Eriksson, "Control-oriented modeling of two-stroke diesel engines with exhaust gas recirculation for marine applications," *Proceedings of the Institution of*

Mechanical Engineers, Part M: Journal of Engineering for the Maritime Environment, vol. 233, no. 2, pp. 551–574, 2019. [Online]. Available: https://doi.org/10.1177/1475090218768992

[43] J. Mc Carthy, W. Norley, and G. Ober, "The performance of a fully submerged propeller in regular waves," David Taylor Model Basin, West Bethesda, Maryland 20817-5700, Tech. Rep. 1440, 1961.

[44] S. Nakamura, N. S., and I. R., "Open-water characteristics and load fluctuations of propeller in waves," *Journal of the Kansai Society of Naval Architects, Japan*, vol. 159, pp. 25–34, 1976. [Online]. Available: https://ci.nii.ac.jp/naid/10030509610/en/

[45] M. Van Sluijs, "Performance and propeller load fluctuations of a ship in waves," Netherlands ship research center TNO, Leeghwatersraat 5, Delft, Netherlands, Tech. Rep. 163, 1972.

[46] A. Aalbers and W. Gent, "Unsteady wake velocities due to waves and motions measured on a ship model in head waves," vol. 15, 1985, pp. 69–81. [Online]. Available: https://ci.nii.ac.jp/naid/20001674599/en/

[47] S. Nakamura and S. Naito, "Propulsive performance of a container ship in waves," *Royal Architecture and Ocean Engineering,The Society of Naval Architects of Japan*, vol. 15, no. 158,159.162, pp. 24–48, 1977. [Online]. Available: https://repository.tudelft.nl/islandora/object/uuid:7972f9f5-77bd-4dd9-a55d-90d1f150f41e?collection=research

[48] G. Politis, "Unsteady rollup modeling for wake-adapted propellers using a time-stepping method," *Journal of Ship Research*, vol. 49, no. 3, 2005.

[49] ——, "The BEM as a tool for analysing unsteady propulsor motions, with applications to maneuvering propellers and biomimetic flows." International Conference on Computational Methods in Marine Engineering, MARINE, Barcelona, Spain, 2011.

[50] R. Tasaki, "On the characteristics of the driving machine in the self-propulsion test among waves," *Journal of Zosen Kiokai*, vol. 1957, no. 101, pp. 25–32, 1957. [Online]. Available: https://doi.org/10.2534/jjasnaoe1952.1957.25

[51] M. Ueno, Y. Tsukada, and K. Tanizawa, "Estimation and prediction of effective inflow velocity to propeller in waves," *Journal of Marine Science and Technology*, vol. 18, no. 3, pp. 339–348, September 2013. [Online]. Available: https://doi.org/10.1007/s00773-013-0211-8

[52] B. Taskar and S. Steen, "Analysis of propulsion performance of KVLCC2 in waves." Fourth International Symposium on Marine Propulsors, Austin, Texas, USA, July 2015.

[53] K. K. Yum, B. Taskar, E. Pedersen, and S. Steen, "Simulation of a two-stroke diesel engine for propulsion in waves," *International Journal of Naval Architecture and Ocean Engineering*, vol. 9, no. 4, pp. 351 – 372, 2017. [Online]. Available: https://doi.org/10.1016/j.ijnaoe.2016.08.004

[54] B. Taskar, K. K. Yum, S. Steen, and E. Pedersen, "The effect of waves on engine-propeller dynamics and propulsion performance of ships," *Ocean Engineering*, vol. 122, pp. 262 – 277, 2016. [Online]. Available: https://doi.org/10.1016/j.oceaneng.2016.06.034

[55] N. Kyrtatos, G. Politis, V. Lambropoulos, G. Theotokatos, N. Xiros, and J. Coustas, "Optimum performance of large marine engines under extreme conditions." CIMAC Congress, Copenhagen, Denmark, 1998.

[56] M. Ott, I. Nylund, R. Alder, T. Hirose, Y. Umemoto, and T. Yamada, "The 2-stroke low-pressure dual-fuel technology: From concept to reality," no. 233. 28th CIMAC Congress, Helsinki, Finland, June 6th to June 10th, 2016.

[57] K. Yum, S. Skjong, B. Taskar, E. Pedersen, and S. Steen, "Simulation of a hybrid marine propulsion system in waves," no. 202. 28th CIMAC Congress, Helsinki, Finland, June 6th to June 10th, 2016.

[58] G. Theotokatos and N. Kyrtatos, "Investigation of a large high- speed diesel engine transient behavior including compressor surging and emergency shutdown," *ASME. J. Eng. Gas Turbines Power*, vol. 125, no. 2, pp. 580–589, 2003. [Online]. Available: https://doi.org/10.1115/1.1559903

[59] M. Foteinos, E. Tzanos, and N. Kyrtatos, "Ship hull fouling estimation using shipboard measurements, models for resistance components, and shaft torque calculation using engine model," *Journal of Ship Research*, vol. 61, no. 2, pp. 64–74, 2017. [Online]. Available: https://doi.org/10.5957/JOSR.61.2.160053

[60] G. Woschni and F. Anisits, "Experimental investigation and mathematical presentation of rate of heat release in diesel engines dependent upon engine operating conditions," in *Automotive Engineering Congress and Exposition*. SAE International, February 1974. [Online]. Available: https://doi.org/10.4271/740086

[61] G. Woschni, "A universally applicable equation for the instantaneous heat transfer coefficient in the internal combustion engine," in *National Fuels and Lubricants, Powerplants, Transportation Meetings.* SAE International, February 1967. [Online]. Available: https://doi.org/10.4271/670931

[62] E. Ciulli, "A review of internal combustion engine losses part 1: Specific studies on the motion of pistons, valves and bearings," *Proceedings of the Institution of Mechanical Engineers, Part D: Journal of Automobile Engineering*, vol. 206, no. 4, pp. 223–236, 1992. [Online]. Available: https://doi.org/10.1243/PIME_PROC_1992_206_183_02

[63] M. I. Foteinos, A. Papazoglou, N. P. Kyrtatos, A. Stamatelos, O. Zogou, and A. M. Stamatellou, "A three-zone scavenging model for large two-stroke uniflow marine engines using results from CFD scavenging simulations," *Energies*, vol. 12, no. 9, 2019. [Online]. Available: https://doi.org/10.3390/en12091719

[64] J. Jensen, A. Kristensen, S. Sorenson, N. Houbak, and E. Hendricks, "Mean value modeling of a small turbocharged diesel engine," February 1991. [Online]. Available: https://doi.org/10.4271/910070

[65] Mathworks, "Curve fitting toolbox, user's guide," 1 Apple Hill Drive, Natick, MA 01760-2098, Tech. Rep., 2019. [Online]. Available: https://www.mathworks.com/help/pdf_doc/curvefit/curvefit.pdf

[66] J. S. Carlton, *Marine Propellers and Propulsion*, 3rd ed. Butterworth-Heinemann, 2012, ch. 11, pp. 275–279. [Online]. Available: http://dx.doi.org/10.1016/B978-0-08-097123-0.00001-0

[67] M. Parsons, "Mode coupling in torsional and longitudinal shafting vibrations," *Marine Technology*, vol. 20, no. 3, pp. 257 – 271, 1983.

[68] N. Xiros, *Robust Control of Diesel Ship Propulsion.* Springer-Verlag London, 2002, ch. 1, p. 8. [Online]. Available: https://doi.org/10.1007/978-1-4471-0191-8

[69] E. Tronconi and P. Forzatti, "Adequacy of lumped parameter models for scr reactors with monolith structure," *AIChE Journal*, vol. 38, no. 2, pp. 201–210, 1992. [Online]. Available: https://aiche.onlinelibrary.wiley.com/doi/abs/10.1002/aic.690380205

[70] V. Bertram, *Practical Ship Hydrodynamics*, 2nd ed. Butterworth-Heinemann, 2012, ch. 3, pp. 121–124. [Online]. Available: https://doi.org/10.1016/B978-0-08-097150-6.10002-8

[71] R. Roddy, D. Hess, and W. Faller, "Neural network predictions of the 4-quadrant Wageningen propeller series," David Taylor Model Basin, West Bethesda, Maryland 20817-5700, Tech. Rep., 2006.

[72] W. Lammeren, J. Manen, and M. Oosterveld, "The Wageningen B-Screw series." SNAME Annual Meeting, New York,NY, 1969.

[73] M. Oosterveld and P. Oossanen, "Further computer-analyzed data of the Wageningen B-screw propeller series," *International Shipbuilding progress*, vol. 22, no. 151, 1975.

[74] J. Holtrop and G. Mennen, "An approximate power prediction method," *International Shipbuilding Progress*, vol. 29, no. 335, pp. 166 – 170, 1982.

[75] J. Holtrop, "A statistical re-analysis of resistance and propulsion data," *International Shipbuilding Progress*, vol. 31, no. 363, pp. 272 – 276, 1984.

[76] P. Oltmann, "Identification of hyrodynamic damping derivatives - a pragmatic approach." Proceedings of the international conference on marine simulation and ship manoeuverability (MARSIM), Kanazawa, Japan, 2003.

[77] A. R. Lloyd, *Seakeeping: Ship Behaviour in Rough Weather*. Ellis Horwood, 1988.

[78] A. Papanikolaou, "On integral-equation-methods for the evaluation of motions and loads of arbitrary bodies in waves," *Ingenieur-Archiv*, vol. 55, no. 1, pp. 17–29, January 1985. [Online]. Available: https://doi.org/10.1007/BF00539547

[79] S. Liu, A. Papanikolaou, and G. Zaraphonitis, "Prediction of added resistance of ships in waves," *Ocean Engineering*, vol. 38, no. 4, pp. 641 – 650, 2011. [Online]. Available: http://www.sciencedirect.com/science/article/pii/S0029801810002775

[80] ——, "Practical approach to the added resistance of a ship in short waves." International Society of Offshore and Polar Engineers, July 2015.

[81] T. Perez, *Ship Motion Control,Course Keeping and Roll Stabilisation Using Rudder and Fins*. Springer-Verlag London, 2005. [Online]. Available: https://doi.org/10.1007/1-84628-157-1

[82] K. Minsaas, O. Faltinsen, and B. Persson, "On the importance of added resistance, propeller immersion and propeller ventilation for large ships in a seaway." Second International Symposium on Practical Design in Shipbuilding (PRADS), Seoul, Korea and Tokyo, Japan, 1983.

[83] "ACME research project final technical report," European Commission, Tech. Rep., 2000.

[84] K. Belibassakis, G. Politis, and T. Gerostathis, "Calculation of ship hydrodynamic propulsion in rough seas by non-linear bem with application to reduction of energy losses in waves." 32th International Conference on Offshore Mechanics and Arctic Engineering (OMAE), June 9-14, 2013.